Studies on vegetation mapping and methane emissions in a taiga-tundra boundary lowland, northeastern Siberia

Tomoki Morozumi

Doctoral Dissertation

Graduate school of Environmental Science,
Hokkaido University, Sapporo, Japan

北東シベリアのタイガ-ツンドラ境界における
植生マッピングとメタン放出に関する研究

北海道大学大学院環境科学院

両角友喜

Abstract

The taiga–tundra boundary ecosystem is expected to be affected by climate change. While high latitude regions could contribute substantially to methane (CH_4) emissions, those emissions in the taiga–tundra boundary has been only sparsely evaluated at local to regional scales. Here, we linked *in situ* CH_4 fluxes from 2009 to 2016 with vegetation cover, and scaled these findings to estimate CH_4 emissions at a local scale (10 × 10 km) using high-resolution (0.5 m) satellite images in a taiga–tundra boundary ecosystem on permafrost (Indigirka lowland, northeastern Siberia). We also linked samples of dissolved methane concentrations in the river water in 2016 (usual year) and 2017 (extreme flooding) with satellite water colour for delineating different water sources. *In situ* CH_4 emissions were high in the wetland vegetation classes, including cotton-sedge, *Sphagnum*, and emergent plants. Lakes and rivers were also CH_4 sources, while forest floors were not a CH_4 sink. Furthermore, relatively high concentrations of dissolved methane (0.7–1.1 μmol l^{-1}, or μM) were observed in four tributary areas in 2017 during the flood's recession, while these values remained low in the main channel (0.2–0.3 μM). Estimated local CH_4 emissions (37±10 mg m^{-2} d^{-1}) were higher than those of other tundra studies in eastern Siberia. Our results indicate that: i) sedge and emergent wetland ecosystems in the taiga–tundra boundary lowland act as hot spots for CH_4 emissions, ii) tree distribution does not regulate the local CH_4 emissions and balances, because of sparse tree coverage, and iii) dissolved methane concentrations in the river surface water can be estimated using satellite reflectance which can provide a new tool for environmental monitoring of flood events in remote areas.

OUTLINE

Thesis submitted in February 2019. Hokkaido University, Sapporo, Japan.

Chapter 1 Introduction

1-1 Changing ecosystem and methane emissions in circum-arctic terrestrial regions

Circum-arctic terrestrial regions are highly vulnerable and affected by rapid temperature increasing in the surface air and the permafrost (Serreze and Barry 2011; Hartmann et al., 2013; Vaugham et al., 2013). Under changing climate in the arctic, a large amount of carbon (approximately 1672 Pg) in permafrost might become a source of greenhouse gases (GHGs) such as carbon dioxide (CO_2) and methane (CH_4) which have a potential of strong feedback to climate (Tarnocai et al., 2009). Especially, northern wetland and freshwater system are one of the largest natural sources of global CH_4. In 2007, global mean CH_4 concentrations were shifted from stable to increasing (Nisbet et al., 2014). Bousquet et al., (2011) reported the concentration changes potentially could be affected by high-latitude wetland sources up to 25% in 2007.,. However, those studies are challenging due to large uncertainties of sources. Indeed, bottom-up estimation of wetland CH_4 emissions has a large uncertainty, and there has been not much improvement from previous researches (Christensen et al., 2015). Therefore, the challenges on estimating CH_4 emissions in circum-arctic region is needed.

1-2 Principles of processes on methane emissions

Methane (CH_4) is generally produced by methanogenic archaea under an environment of anoxic soils in wetlands. There are mainly two pathways: i) acetoclastic reaction in which CH_4 and CO_2 are produced from one molecule of acetate, and ii) hydrogenotrophic reaction in which CH_4 and H_2O are produced from one molecule of CO_2 and four molecules of H_2 (Bridgham et al., 2013). Anoxic conditions were maintained under high soil moisture and deeper soil isolated from atmospheric oxygen, and acetoclastic production are affected by root exudates from plants. After the production processes, CH_4 is transported from wetland soils to atmosphere through three pathways: i) diffusion from soil surface, ii) ebullition from soil surface, and iii) transportation through aerenchyma of plant which could act as duct pipes.

Next, we consider consumption of CH_4 in soils. Methanotrophic archaea has an oxidation pathway that CH_4 is converted to methanol and captured into metabolic circuit, then finally it produces CO_2. Methanotroph could consume CH_4 in oxic soil in upland forest and also on the plants root and surface of *Sphagnum* tissues in peatland, although the consumption rate is generally 10^{-1}- 10^{-2} times lower than production rate in

wetland (e.g., Chen and Murrel 2010, Mander et al., 2016).

In the freshwater system, CH_4 is generally produced in bottom sediments under anoxic condition, and from organic matter in a water column (Crawford et al., 2017, and Stanley, 2016). Freshwater CH_4 is also controlled by transportation from surrounding landscape such as wetland and peatland via groundwater pathway in a catchment. Lakes are generally deep and vertically stratified with thermocline, and bottom environment is kept more anoxic, whereas rivers are vertically mixed with turbulence and kept oxic with water flow. Therefore, CH_4 production could be higher in lakes than those in rivers.

1-3 Principle of scaling as a tool to understand regional methane flux

Geographical information system (GIS) is strong tool to calculate the regional budget of methane cycles. Geographic categories of map, such as land cover, vegetation and land use information, were assigned as an area weight of each target regions, and scaled using indivisual measurements. However, observation sites for CH_4 emissions from natural wetlands and freshwaters are sometimes located on a remote area where no detail geographic information. Furthermore, water levels, extents and water qualities of freshwaters differ among seasons and years. In those case, remote sensing techniques can provide suitable geographical information rather than already existing data.

Satellite images such as Landsat have a visible-near infrared (NIR) band, which are used for delineating land covers, vegetation, soils and waters. Surface reflectance, which is calculated by outgoing radiance from a target surface divided by incoming radiance below atmosphere, are widely used for spectral properties. Detector of satellite can only receive the outgoing radiance on the top of atmosphere, therefore atmospheric corrections are applied for calculate surface reflectance from raw data of satellite images. The spectral properties of vegetation are determined by photosynthetic pigment at a leaf, and structures of leaves (Jones and Vaughan, 2010). The leaf area index (LAI), one side leaf area per unit ground area, is also known as the most important characteristics on spectral properties of vegetation canopy. In water surface reflectance, water quality indicators such as total suspended sediments, chlorophyll-*a* and colored dissolved organic matters are important characteristics to determine spectral properties (Gholizadeh et al., 2016). Surface reflectance, detected in a satellite sensor, is provided by *in situ* remote sensing reflectance of water column multiplied by pi(π) (Belzile et al., 2004). Incident light is penetrating and reflecting at thin surface water column in particular case in turbid water, where a penetration depth is 60 cm in the water containing suspended sediment of 400mg/L (Gholizadeh et al., 2016). A remote sensing technique for waterbody methane emissions was introduced by Xiao et al., (2017) in inland lake, using empirical regression between flux and factors of water clarity, dissolved oxygen (DO), depth, and normarised difference vegetation index (NDVI). However, the relation here was depend on water input from surrounding and lake basal structures. Therefore, it is still challenging to apply this method to other regions and river,and a feasibility study should be done for further improvement. Those

characteristics such as vegetation and water qualities are classified or modeled with control factors of CH_4 fluxes and applied for regional upscaling of methane emissions and balances.

There are technical subjects in satellite remote sensing, especially in taiga-tundra boundary which is characterised by heterogenous landscapes. Vegetation and land cover are continuously changing from forests to fens or lakes. However, satellite data are stored in a pixel of a certain extent, and those features are discontinuous in an image. Spatial information in a satellite image are regulated by resolution of each pixel, therefore it is necessary to acquire high resolution data to observe small features such as vegetation patchesin an observation site as described below (Chapter 2).

1-4 Changing ecosystem and hydrology in taiga-tundra boundary

Taiga-tundra boundary ecosystems are surrounding terrestrial arctic as a complicated shape of treeline belt (Montesano et al., 2009). Taiga-tundra boundary (alternate name for tundra taiga ecotone, or forest-tundra) is a region between continuous boreal forest and tree distribution limit. Pan-arctic regions, including taiga-tundra boundary ecosystems, are affected by global warming. Boreal-tundra biome shift is hypothesized on global vegetation model studies as coniferous forest replacing tundra and has been recognized by many field researches such as shrub expansion and tree growth trends (Settele et al., 2014). The shifting of boreal-ecosystems into wetland dominated tundra-ecosystem might reduce the effects of global warming with reducing source area of CH_4, and increasing atmospheric CH_4 absorption (Callaghan et al., 2002). Contrastly, changing forests to wetlands might occur with more precipitation and shallower frozen layer of the permafrost (Skre et al., 2002), or with permafrost collapsing (Desyatkin et al., 2011). Those changes of biome shift could explain as sequences of vegetation successions in the view of local scale. In northeastern Siberian lowland, floodplains are gradually shifting from an aquatic plants stage (*Equisetum* spp. or *Arctophylla fulva*, typically emerging from shallow water <1m depth), a shrub stage (*Salix* spp. and *Alnus fruticosa*) to a larch forest stage (*Larix* spp. with forbs, *Betula nana* and green-moss), and suddenly go back to former stage by erosion and deposition with flooding (Troeva et al., 2010). In similar ways, lakes are gradually shifting from an emergent plant stage (*Caltha* spp., *Hippuris* spp., typically emerging from shallow water <1m depth), a fen stage (*Arctophylla fulva* and *Carex* spp.), a bog stage (*Sphagnum* spp.) to hummock-forest stages (*Larix* sp. with forbs, *Betula nana* and green-moss), and suddenly go back to former stage by thermokarst and refilling water (e.g., Troeva et al., 2010). Successions from wet to drained forest could decrease source area of CH_4 emissions. Those changes may occur over hundreds to thousands of years, although recent climate changes could affect to the ecosystem and CH_4 emissions in shorter terms. For example, extreme rainfall was occurred in 2007 in eastern Siberia (Central Yakutia), forests were disturbed, and carbon cycle were also changed by unusual overwetting (Iwasaki et al., 2010, Tei et al., 2013, Ohta et al., 2014). We need to understand the environmental changes in both successional vegetation shift

timescales and event-induced short timescales.

1-5 Research aim and purposes

To clarify the local CH_4 emissions and the role of taiga-tundra boundary ecosystem among regional CH_4 budget in high latitude, we set four scientific questions: i) What are the environmental factors controlling vegetation distribution? ii) What is the factor limiting for local CH_4 emissions? iii) Whether hypothesized CH_4 absorption in forest floor could affect local CH_4 emissions? iv) Are there any effect on CH_4 emissions by flooding event? Approaches for answering those questions are below: The permafrost and locational factors were observed in the field. Vegetation coverage and contribution for CH_4 emissions were evaluated in the ecosystem using remote sensing and upscaling method. Local CH_4 emissions was compared to those in tundra site in previous studies and discussed for regional characteristics. Riverine dissolved CH_4 concentrations and fluxes were compared between flood year (2017) and normal year (2016). We expect to obtain field-based-knowledge for future change projection and adaptation under climate change.

Additionally, methodological questions should be answered for detecting vegetation, evaluating local CH_4 emissions, and delineating dissolved methane concentrations in surface water of river. As approaches for spatial heterogeneity, vegetation was sampled with step-by-step in multiscale from site (100 m) to local (10 km). Chamber measurements were planned to detect spatial variation of fluxes from wide areas due to the advantage of replacing to another observation point. High resolution (0.5 m per 1 pixel) satellite data were combined with detailed sampling of an in-field spectral measurement and training pixels based on field observations. Satellite surface reflectance data were used for water color detection, and modelling for water mixing between main flow and tributary on flooding in the region (~200 km). Studies need to be conducted based on the fact of own dataset, for local to regional estimation of CH_4 with accurate stand-alone evaluations.

Chapter 2 Local-scale vegetation mapping and estimation of methane emissions in taiga-tundra boundary lowland

Accepted; TelllusB: Chemical and Physical Meteorology, 10.1080/16000889.2019.1581004.

2-1 Introduction

The boundary ecosystem between taiga and tundra (i.e., forest-tundra ecotone) covers an area larger than 1.9 million km^2 in the circumarctic region (Ranson et al., 2011). In this ecosystem, tree cover has expanded since the late 1800s in north-western Alaska (for a distance of approximately >10 km) (Lloyd et al., 2002), and over recent decades in Siberia (Kravtsova and Loshkareva, 2013; Frost and Epstein, 2014), where further tree line shifts are predicted to occur according to climate response model studies (Skre et al., 2002; Soja et al., 2007; Tchebakova et al., 2009). Methane (CH_4) is a potent greenhouse gas that contributes to approximately 20% of the radiative forcing attributed to anthropogenic-derived increase of greenhouse gas concentrations (Ciais et al., 2013; Myhre et al., 2013). The competition for landscape between wetland (source) and upland (sink) ecosystems would affect regional CH_4 emissions regarding vegetation shifts (Callaghan et al., 2002; Harding et al., 2002). However, scenarios of vegetation shifts depend on whether the climate changes to dry or humid (e.g. Holtmeier and Broll, 2005). The change of forests to wetlands might occur with paludification or permafrost thawing in lowlands by changing the humidity and the frozen layer of the permafrost (Skre et al., 2002).

Montesano et al. (2009) reported that the structure of the taiga-tundra boundary ecosystem is scale dependent in the studies using remote sensing, as a patchy forest or wetland can be observed with high-resolution data but cannot be seen with low-resolution data. Epstein et al. (2004) reported two types of tree lines in Alaska: forest-shrub tundra transitions along mountain slopes, and abrupt forest-tussock tundra transitions associated with river floodplains. Such transitions between forest and tussock tundra or thermokarst wetlands generally correspond to drastic shifts from CH_4 sinks to CH_4 sources, which is largely regulated by environmental factors such as soil moisture (Sjogersten and Wookey, 2002; Morishita et al., 2003; Sjogersten and Wookey, 2009). However, previous studies on CH_4 flux performed at local-regional scales have focused on typical tundra or boreal forest ecosystems (e.g. Nilsson et al., 2001). Only a few studies have assessed the taiga-tundra boundary in Scandinavia (Sjogersten and Wookey, 2002; 2009), Hudson Bay Lowland (Roulet et al., 1994), and West Siberia (Flessa et al., 2008; Glagolev et al., 2011).

Land cover classification is often used to estimate the CH_4 flux in arctic-subarctic regions, as the spatial patterns of both vegetation type and CH_4 flux are controlled by soil moisture. In addition, CH_4 flux is regulated by the functioning of plants via the production of substrates and transport from the soil to the atmosphere (Olefeldt et al., 2013; Strom et al., 2015; Davidson et al., 2016). Therefore, vegetation maps are useful tools for understanding the spatial patterns of CH_4 emissions. Such maps are generated by land cover classifications for wetland vegetation and other plant categories, and they show spatial patterns in vegetation types at targeted spatial scales. Previous studies have usually applied vegetation mapping with *in situ* CH_4 flux to estimate CH_4 emissions in the typical tundra and taiga ecosystems of Siberia (e.g., Takeuchi et al., 2003; Schneider et al., 2009). Recent satellite images with high spatial resolution (i.e., WorldView-2 and Geoeye-1 with a resolution <2 m) provide a preferable mapping scale for the vegetation patch size (<30 m) (Virtanen and Ek, 2014) and water bodies (<4 m) (Muster et al., 2012) in the tundra ecosystem. Indeed, CH_4 emissions on plot-scale were revealed using high-resolution vegetation mapping combined with observational CH_4 fluxes and/or footprint models in the tundra ecosystem (Sachs et al., 2010; Parmentier et al., 2011a; Budishchev et al., 2014, Terentieva at al., 2016). Using high-resolution mapping for wetlands vegetation and water bodies, accompanied by *in situ* measurements of CH_4 flux, emissions on regional and local scales can be estimated in the taiga-tundra boundary ecosystems.

The Indigirka lowland is an arctic floodplain in eastern Siberia, Russia. This lowland is characterized by very specific environmental conditions that include continuous permafrost, a tree distribution limit, and river lowlands. Ice-wedge polygons are one of the most common ground patterns of this ecoregion, representing the typical land surface structure in Indigirka lowland. These polygons were formed from a drained lake basin during a geologically recent event (ca. AD 1250–1325) (de Klerk et al., 2011). In this ecosystem, similar environmental conditions are widespread over a vast area of the Yana-Indigirka-Kolyma lowland in north-eastern Siberia (Troeva et al., 2010). The Indigirka lowland, particularly the nature reserve in the Kytalyk area (located on the left bank of the lowland), has been extensively studied to elucidate the response of a tundra ecosystem to climate change. For example, the impact of permafrost degradation on the growth of tundra shrubs (e.g. *Betula nana*) has been reported in this tundra ecosystem (Blok et al., 2010; Nauta et al., 2015). The study area used in this research (i.e. the middle of the Indigirka lowland) is sparsely covered by larch trees (a taiga-tundra boundary ecosystem), which grow on elevated mounds because of low soil moisture and nitrogen uptake (Liang et al., 2014). In recent years, an increasing number of invasive (expanded) species from more southern areas have been reported (Khitun et al., 2016), likely owing to the rising temperatures. Thus, the very specific nature of this environment, combined with continuous permafrost, the tree distribution limit, and river lowlands, renders the ecosystems of this region potentially vulnerable to climate change.

In this study, we report (*i*) the relationship between the distribution of plant species and environmental factors along a microtopographic gradient, (*ii*) vegetation mapping using high-resolution satellite images on a 10 × 10 km local scale, and (*iii*) *in*

situ CH_4 fluxes for various vegetation types associated with the dry-wet gradient during the summer growing season from 2009 to 2016 in a taiga–tundra boundary ecosystem (Indigirka River lowland, eastern Siberia, Russia). From these results, we aimed to determine (*i*) the effects of environmental factors such as distance from the rivers and permafrost conditions on vegetation, (*ii*) the CH_4 emission on local and regional scales using a vegetation map with high-resolution satellite images in the taiga-tundra boundary ecosystem, and (*iii*) its controlling factors on CH_4 emissions. The distribution of the current vegetation under a scenario of global warming, which may lead to vegetation shifts in the future, was also noted.

2-2 Materials and Methods

2-2-1 Study area

The study sites were located in the Indigirka lowland near Chokurdakh (70.6° N, 147.9° E), Republic of Sakha (Yakutia), Russia. The study area is located on continuous permafrost, with an active layer depth ranging from 20 to 50 cm. The landform is a generally flat floodplain surrounded by an upper terrace over 50 m above sea level (a.s.l.).

Our investigation focused on the taiga-tundra boundary ecosystem—Kodac site (K) (70.56° N, 148.26° E)—over the Indigirka lowland (Figure 2-1). In this ecosystem, vegetation consists of mosaic patterns of sparse larch (*Larix cajanderi*, syn. *L. gmelinii*) stands, with a maximum height of 10 m (the density of the trees above 2 m in height is 341 trees ha^{-1} at site K [Liang et al., 2014]), shrubs (*Betula nana*), and wetlands. The soil is characterized by high organic content in the surface layer and abundant ice lenses (Iwahana et al., 2014). Regularly structured ice-wedge polygons and lakes are often observed in this ecosystem.

2-2-2 Relative elevation, thaw depth, and soil moisture

We defined a 50-m monitoring transect, which was composed of a 100 × 50 m survey plot at site K (Figure 2-2a) with local survey points distributed throughout a 10 × 10 km area of the Indigirka lowland (Figure 2-1). At site K, the relative elevation from the lowest base level was measured using a surveying telescope (AT-B4, TOPCON, Tokyo, Japan) at every 2.5 m point along a 50 m transect on July 31, 2012, and in 5 m grids at 231 points over the 100 × 50 m survey plot on July 14, 2013. In addition, we measured seasonal thaw depth (i.e., active layer depth) using a metal rod, and estimated frost table height by subtracting the thaw depth from the relative elevation over the same survey plot. Volumetric soil moisture was also measured using a portable moisture sensor (Trime-Como, IMKO, Ettlingen, Germany) between the surface and a depth of 8 cm, by performing four observations at every 5 m points along the monitoring transect at site K in mid July 2012, 2014, and 2015, as well as at 70 local survey points distributed throughout the 10 × 10 km area in the Indigirka lowland in mid July 2014.

2-2-3 Plant species composition

The spatial distribution of plant species was investigated at the 231 points sampled for relative elevation at site K on July 14, 2013. During sampling, a quadrat (0.5 × 0.5 m) was placed on fairly homogeneous and wide patches of vegetation, and dominant and rare plant species—including trees, shrubs, grasses, forbs, and mosses—were recorded. Moss species were categorized into five groups (green-moss, green-moss/*Sphagnum*-dry mixed, *Sphagnum*-dry, *Sphagnum*-wet, and moss-wet) according to the soil moisture condition, and contained several typical species and/or genera (Table 2-S1). Close-range aerial photographs were taken by a commercially available radio-controlled unmanned aerial vehicle to confirm the extent of vegetation patches and to aid in training pixel selection (AR Drone 2.0, Parrot, Paris, France).

We also investigated the composition of plant species in the 70 quadrats used to measure soil moisture throughout the 10 × 10 km area in the Indigirka lowland in mid July 2014 (Figure 2-1). We listed all plant species observed at site K, and over the Indigirka lowland, during the vegetation survey from 2013 to 2014. The names and taxonomic classifications of plant species were determined by referring to the circumpolar dataset of the Arctic Biodiversity Assessment (CAFF, 2013) and to a local dataset for Kytalyk (Egorova, 2013), 30 km north of Chokurdakh.

2-2-4 Local methane emissions

Methane flux was observed at 37 locations (212 flux measurements in total), using the chamber method during the growing seasons (July) of 2009 to 2016. The flux measurements were conducted in each vegetation type (see section 2-2-5,2-2-6): i) around site K (70.56 °N, 148.26 °E), ii) around site B, which was located near the main flow of the Indigirka River (70.64 °N, 148.15 °E), and iii) at additional points in the Indigirka lowland (including the lake, river, and bare-land). The total numbers of replicates and the total days of observation in each vegetation type are presented in Table 2-3. For each sampling point, transparent chambers (diameter 25 cm, height 25 cm) were installed on the ground or on a floating panel, and headspace gas, which was sampled at 15-min intervals for 30 min (0, 15, and 30 min), was collected into 20-mL vacuumed vials. Linear correlation of headspace CH_4 with time was conducted for each measurement of CH_4 emissions, and R^2 values of more than 0.95 occurred in most cases. These were used for the flux measurements, although closer and lower CH_4 concentrations than the detection limit showed lower linear correlations.

River CH_4 flux (n = 18) was estimated using the ideal assumption of the transfer velocity method from the concentration of dissolved CH_4 in river water. The transfer velocity method was used instead of the chamber method to overcome the limitations of CH_4 flux data by using a floating chamber on the river water. The assumptions were checked to determine if both results fell within the same range.

River gas flux (J_g) is produced by the differences between gas concentrations in the river water (C_w) and the atmosphere (C_a), and CH_4 transfer velocity (k_{CH4}) was calculated based on the calculation in Striegl et al. (2012), considering a median gas transfer velocity in the boreal Arctic zone (Aufdenkampe et al., 2011) and a temperature dependence function (Wanninkhof, 1992):

$$J_g = k_{CH4}(C_w - C_a)$$

The dissolved CH_4 concentration in the river water (C_w) was analysed using the headspace equilibration method. Details on our observations of river CH_4 flux are provided in 2-2-9.

After sampling headspace gas extracted from the chamber and river water, samples were transported to the laboratory in Hokkaido University, Sapporo, Japan, and CH_4 concentration was measured from the samples with a HP6890 gas chromatograph (GC) system (Hewlett Packard, Palo Alto, CA, USA) with a flame ionization detector (FID) at a precision (i.e., standard deviation [SD]) of 0.3 ppm for 20-ppm standards. Therefore, the detection limit of flux was 4.6 mg m^{-2} d^{-1}. The first phase of these measurements was mainly conducted on sedge and sphagnum wetland vegetation in 2009–2013 (Shingubara et al., 2016). Newly obtained land-surface and river flux data collected in 2014–2016 were then added to the data. Estimations of site- and local-scale CH_4 emissions were performed according to the vegetation classification maps created from satellite imagery (see section 2-2-6) obtained from 400 × 400 m (site scale) and 10 × 10 km (local scale) areas.

2-2-5 Vegetation classifications based on plant species

We classified vegetation in the Indigirka lowland into nine categories for upscaling of CH_4 emission over the region in the following three steps. In the first step, microtopographic vegetation classification was conducted. This classification was made based on the zonal distribution of vegetation (therefore plant species) in relation to micro-relief (which results in differences in soil moisture) and tree distribution (Liang et al., 2014). It is well known that soil moisture gradients cause differences in CH_4 flux (Olefeldt et al., 2013). Therefore, this first step in the classification—on the microtopography—is considered to reflect gradients in CH_4 emission. In the second step, plant species-based vegetation classes were delineated. This classification was made via plant species composition.

In the first step of vegetation survey at the site scale conducted along the 50-m transect at site K (Figure 2-2a), the vegetation was visually classified into four categories—tree, shrub, *Sphagnum* spp., and cotton-sedge—based on the dominant species at each measurement point. Trees and shrubs were generally observed on well-drained elevated mounds and slopes, and *Sphagnum* spp. and cotton-sedges were found in wet areas. Next, the four categories were classified via a clustering analysis,

based on the similarities among plant species compositions. The Ward's method (Maechler et al., 2017)—a bottom-up approach that produces the closest pair of data and aggregates data into larger groups—was applied for hierarchical agglomerative clustering using R software (R Core Team, 2017).

At the site scale, we applied clustering analysis to 16 dominant vascular plant spices, and five groups of green-moss and *Sphagnum* spp., observed at site K (Table 2-S1). We only used the dominant species of vascular plants and groups of moss species, as minor (rare) species were not accurately identified to the species level during the site vegetation survey in 2013. Based on the 16 vascular plant species and five groups of non-vascular plants, eight clusters (i–viii) were identified (Figure 2-S1) and compared with the microtopography classes (Figure 2-3 and Table 2-1). Significant differences in the relative elevation (see section 2-2-3) of the eight clusters were statistically assessed by single factor analysis of variance (ANOVA) among clusters and *t*-tests between pairs of clusters, using MS Excel 2016 (Microsoft Corporation, Redmond, WA, USA).

The larch tree (*Larix cajanderi*) is the only tall woody-type species found in the taiga-tundra boundary ecosystem and it was considered an independent category for the spatial variation in potential CH_4 sinks. Therefore, the presence of *L. cajanderi* was emphasized to distinguish it from other plant species (see Figure 2-S1). For the other clustering processes, an equal distance of clustering similarity was applied.

To analyse the variation in plant community composition at a local scale, we used the 71 plant species observed in the local vegetation survey (Table 2-S2) for the clustering analysis and identified 12 clusters (i–xii) (Figure 2-S2). Then, we further classified the 12 clusters into seven classes in the same manner used for the site-scale classification. Clusters were cross-validated with visual interpretation of each vegetation type and evaluated using purity and entropy. In an ideal cluster of a single category, purity is 1, and entropy is 0. Higher purity and lower entropy indicate better clustering results.

2-2-6 Vegetation classification based on satellite imagery

Land-cover classification surveys were conducted for 400 × 400 m (site scale) and 10 × 10 km (local scale) areas using WorldView-2 data (Digital Globe Co., Ltd., Westminster, CO, USA) collected on July 9, 2013, with eight spectral bands (2 m spatial resolution) and one panchromatic band (0.5 m resolution).

Satellite image calibration, correction, and classification were performed using ENVI v5.1 (Exilis Visual Information Solutions, Broomfield, CO, USA) and were mapped with ArcGIS v10.2 (Environmental Systems Research Institute, Redlands, CA, USA).

Image classifications were performed using a combined method of maximum-likelihood classification (MLC) and decision-tree classification (DTC). The MLC-DTC method was supervised by the data for plant species-based vegetation classification described in the previous section. *In situ* observation points (Figure 2-1b) for plant species composition were transferred from pan sharpening 0.5 m resolution

images into 27,896 pixels, which were carefully selected homogeneous and uniform areas for optimal targeting. Among those, 17,113 training pixels were used for supervision and 10,783 test pixels were used for evaluation, and then reflectance features of training pixels were confirmed to distinguish vegetation classes (Figure 2-S4). Details of the MLC-DTC method is presented in 2-2-8 (Figure 2-S3). In addition, we compared the classification of the MLC-DTC method to three different methods, namely spectral information divergence (SID), simple MLC, and simple DTC, to decide the optimal classification method (2-2-8, Table 2-S5) and to select the most appropriate method for accurate classification. We compared the results with satellite-based data and used it for the classifications (see 2-2-8).

To validate classification methods, classification results of test pixels (10,783 pixels) in each method (Figure 2-1b) were compared, and the overall accuracy and kappa statistics (Congalton, 1991) were calculated. The MLC-DTC method showed the highest accuracy and was, therefore, the optimal method for classifying vegetation distribution at our site (Table 2-S5). Therefore, the precision of MLC-DTC classification for each class (Table 2-S6) was based on test pixels using a confusion matrix, which is a list showing the number of pixels classified into each class. The confusion matrix shows the producer accuracy (PA) of test pixels of a given class (the percentage of the number of pixels that were correctly classified into the class) and the user accuracy (UA) of test pixels classified into a class (the percentage of the number of pixels that were correctly classified into the class).

2-2-7 In situ vegetation reflectance

We investigated the reflectance of vegetation types (see section 2-2-5) as training classification of the spectral information divergence (SID) method (see section 2-2-6), at site K and other locations over the Indigirka lowland in July 2013 and 2015 using a MS-720 portable spectroradiometer (Eko Instruments Co., Ltd., Tokyo, Japan), with a field of view of 24°. Spectral reflectance was measured at 40 to 60 cm from each target sample. Reflectance values were calculated by the ratio of target irradiance to solar irradiance (obtained simultaneously) using a white reference panel (Spectralon, Lab sphere Co., Ltd., North Sutton, USA, 99% reflectivity). Dominant species, such as *Larix* spp., *Salix* spp., and cotton-sedge, were observed at 30 plots, with eight replicates for each plot.

2-2-8 Satellite image correction and classification with different methods

Atmospheric correction was applied to all eight spectral bands and the panchromatic band in WorldView-2 satellite data to derive the surface reflectance for comparison with ground-based reflectance measurements. The 6S radiative transfer model (Vermote et al., 1997) was used for the atmospheric correction. The

widely-accepted Gram-Schmidt pan-sharpening method was applied to 2 m resolution multispectral images and those were sharpened to 0.5 m resolution images.

Image classifications were performed using four different methods: i) maximum-likelihood classification (MLC), ii) spectral information divergence (SID), iii) decision-tree classification (DTC), and iv) a combined method of MLC and DTC (MLC-DTC). The MLC method was supervised by the plant species-based vegetation classification. The MLC was calculated by equation below:

$$g_i(\mathrm{x}) = \ln p(\omega_i) - 1/2 \ln \left| \sum_i \right| - 1/2\,(x - m_i)^T \sum_i^{-1} (x - m_i)\,,$$

,where i = class, x = n-dimentional data, p(w_i) = probability that class w_i occurs in the image and is assumed the same for all classes, $\left|\sum_i\right|$= determinant of the covariance matrix of the data in class w_i, $\sum_i^{-1}$ = its inverse matrix, and m_i = mean vector (Richards, 1999 implemented in ENVI).

In situ observation points (Figure 2-1b) for plant species composition were transferred from pan sharpening 0.5 m resolution images into 17,113 training pixels, which were carefully selected homogeneous and uniform areas for optimal targeting. Test pixels (10,783 pixels) were also selected from regions (Figure 2-1b) independent from the training set. Pixels were usually selected by drawing three or more target regions for each vegetation class. Each target region generally contains 500 pixels or more. Under the relatively sparse tree density at the site K, tree canopy pixels were selected from large numbers of smaller target regions than those in other classes. The regions of tree have 16 for training and 16 for test, in which contains 16-100 pixels for each region. The region of shrub subgroups (Table 2-S4) also have 19 small regions for training. The spectral separability of vegetation classes in satellite images was quantified by measuring the Jeffries-Matushita distance, which is commonly used for classification processes and is not saturated at larger spectral differences (Richards and Jia, 1999). A Jeffries-Matushita distance greater than 1.85 was selected as an empirical threshold that had good separability for classification with training pixels obtained in this study.

The spectral information divergence (SID) method was supervised with *in situ* reflectance of vegetation (see S1.1), and waterbody reflectance averaged for lakes and rivers in the dataset acquired from the USGS spectral library in ENVI 5.1 (Clark et al., 1993). The SID was calculated by equation below:

$$SID(r, r') = \sum_{j=1}^{L} p_j \log\left(\frac{p_j}{q_j}\right) + \sum_{j=1}^{L} q_j \log\left(\frac{q_j}{p_j}\right),$$

,where p and q =pair of probability mass functions generated by spectral signature for band j, L=spectral band channel, r and r' = pair of multispectral pixel vector (Du et al., 2004 inplemented in ENVI software).

The Normalized Difference Vegetation Index (NDVI) and the Forest Discrimination Index (FDI) (Bunting and Lucas, 2006) were used in DTC, and were defined as:

$$NDVI = (NIR - Red)/(NIR + Red)$$

$$FDI = NIR - (Blue + Red)$$

MLC-DTC classification has been used to rectify the potential overestimation of some classes of MLC by empirically applied vegetation indexes.

2-2-9 Calculation of river CH4 flux

Dissolved CH_4 in the water samples was measured using the headspace equilibrium technique. A 15 ml sample water was injected into a syringe and shaken, and equilibrated with 45 ml ultrahigh purity N_2 headspace gas for five minutes. The concentration of the headspace gas was analyzed using a HP6890 GC system gas chromatograph (Hewlett Packard, Palo Alto, CA USA). The initial concentrations in river water samples were calculated using Bunsen solubility (Yamamoto et al., 1976).

River CH_4 flux calculations followed Striegl et al., (2012). Flux is calculated by Fick's First Law with a function of the concentration of dissolved gas in the river water (Cw) and in the atmosphere (Ca), and the gas transfer velocity (k) of CH_4.

$$Flux = (Cw - Ca) \times k_{CH4}$$

where k_{CH4} is a product of the relation between CO_2 and CH_4 transfer velocity (Striegl et al., 2012):

$$k_{CH4} = k_{600} (ScCH_4/400)\ 0.69\ (m\ d^{-1})$$

where gas transfer velocity k_{600} is a function of water surface turbulence, and is therefore depends on a river's geography.

Aufdenkampe et al., (2011) reported global CO_2 gas exchange velocity data sorted into zonal and scale-dependent types. The gas exchange velocities for Rivers (6.0 cm hr^{-1}) and Streams (13.1 cm hr^{-1}) in the Boreal arctic zone were applied to the Indigirka mainstream and its tributaries in this study. The Schmidt number of CH_4 ($ScCH_4$) is the ratio between kinetic viscosity and diffusion efficiency. Wanninkhof (1992) showed the Schmidt number (Sc) as a function of temperature (t) dependency calculated as:

$$Sc = A - Bt + Ct^2 - Dt^3$$

where notations are parameters of fresh water CH_4 (A=1897.8, B=114.28, C=3.2902, D=0.039061).
River CH_4 fluxes in this study were calculated using these equations (Figure 2-S7).

2-3 Results

2-3-1 Relative elevation, thaw depth, and soil moisture

Micro-relief elevation was approximately 40 cm in the 50-m transect, where each topographic position was covered by characteristic vegetation (Figure 2-3). Soil moisture was high (12–98%) at low elevations (0–25 cm), where *Sphagnum* sp. mosses and sedges were found. Cotton-sedge was present in the lowest and wettest areas. In contrast, soil moisture was low (3.8–40%) at higher elevations (35–44 cm), where larch trees and shrubs were found. Based on these results, we defined the following four classes of plants: tree, shrub, *Sphagnum* spp., and cotton-sedge (Table 2-1). Trees and shrubs included *Larix cajanderi*, *B. nana*, and *Vaccinium uliginosum*, which were found on microtopographic mounds. In comparison, *Sphagnum* spp. and cotton-sedges (including *Carex aquatilis* and *Eriophorum angustifolium*) were located in wet microtopographic depressions.

2-3-2 Plant species-based vegetation classifications

In this study, we found 71 plant species at site K, including 60 vascular plants and 11 species of mosses (Table 2-S2). Most species observed were from the families Poaceae (nine species) and Ericaceae (eight species), but species from the families Cyperaceae (seven species) and Salicaceae (seven species) were also abundant. Many of the species observed are boreal-hypoarctic species that occur in the taiga and southern part of the tundra within the arctic Siberian region (e.g. Egorova, 2013), such as the shrubs *B. nana* and *Salix pulchra*; the heaths *V. uliginosum*, *Vaccinium vitis-idaea*, and *Ledum decumbens*; and the sedges *C. aquatilis* subsp. *stans* and *Eriophorum vaginatum*. Among the observed species at site K, dominant vascular plants and mosses were used for clustering at the site scale analysis, while all plant species were used for clustering at the local scale analysis.

For the site scale analysis, eight clusters (i–viii) were identified (Figure 2-S1 and Table 2-S1). Based on the clustering results, the vegetation was subsequently classified into four classes. Cluster (i) was classified as tree class; clusters (ii) and (iii) were classified as cotton-sedge and *Sphagnum* spp. classes, respectively; and clusters (iv)–(viii) were classified as shrub class, with clusters (iv) and (v) being shrub-dry and clusters (vi) and (vii) being shrub-moist vegetation. Cluster (viii) was also classified as shrub class and was placed in the dry-tussock vegetation.

At the local scale, we identified 12 clusters (i–xii) (Figure 2-S2 and Table 2-S2). We further classified these 12 clusters of vegetation into seven vegetation classes, similar to that performed at the site scale analysis. Clusters (i), (ii), and (iii), which include trees (*Larix cajanderi*) with different understories, were classified into the tree

class. Clusters (iv) and (v) were characterized by evergreen shrubs (e.g. *Dryas octopetala*) and grass-type plants (e.g. *Poa* sp. and *Luzula confusa*), respectively, and were classified into the lichen-heath class. Clusters (vi) and (vii) were characterized by deciduous shrubs (e.g. *B. nana*) and therefore were classified into the shrub class. Clusters (viii) and (ix) were classified as willow vegetation. These clusters were dominated by alders (*Alnus viridis* ssp. *fruticosa* syn. *A. fruticosa*) and upright-type willows (e.g. *Salix boganidensis*, *Salix richardsonii*, and *Salix alaxensis*), and their canopies were higher than that of plants in the shrub class; moss species were also included. Soil moisture conditions for this vegetation were similar to those of the shrub class (Table 2-S2). Cluster (x) was classified into the emergent class, which was characterized by emergent aquatic species (e.g. *Arctophila fulva* and *Carex chordorrhiza*) and by wet soil conditions with a water table higher than ground level (typically shallow water of < 1 m depth covered by leaves elongated from underwater). Clusters (xi) and (xii) were characterized by sedges (e.g. *Carex* spp. and *Eriophorum* spp.) and *Sphagnum* spp. (e.g. *Sphagnum squarrosum*), and were classified into the cotton-sedge and *Sphagnum* spp. classes, respectively. Cross-validated purity (0.76) was high and entropy (0.24) was low in the hierarchical clustering.

Although clusters grouped by plant species were classified into four classes at the site scale and seven classes at the local scale, the corresponding classes exhibited similar species compositions, with common dominant species between both site and local classifications (Table 2-S1 and S2). Therefore, similar vegetation classes within the site and local classifications were combined into one class, and a total of six classes was obtained (Table 2-1). According to these results, classes based on plant species composition were assigned to a mapping definition, although the lichen-heath class (which was observed on hilly slopes 50 m a.s.l. at a local scale) was excluded from further analyses, as the focus of the present study was on CH_4 emissions in lowland ecosystems.

2-3-3 In situ and satellite reflectance

In situ average reflectance spectra of each vegetation class are shown in Figure 2-S5. Surface reflectance was demonstrated by a factor between 0 and 1 with no unit. In the spectral profile of vegetation targets, relatively constant reflectance (approx. 0.4–0.45) was observed in tree and willow samples for near infrared (NIR) regions at wavelengths between 760 nm and 930 nm. In contrast, a clearly sloping reflectance signature (approx. 0.3–0.45) was observed for *Sphagnum*, cotton-sedge, and emergent samples for the NIR region.

To classify vegetation into the previously determined (see section 2-3-2) six classes, including the subgroups of the shrub class (shrub-dry, shrub-moist, and dry-tussock) and willow class (willow and alder), using satellite image data, sets of more than 200 pixels for each vegetation class were successfully selected as training pixels (Figure 2-S4). In addition, pixels for bare land, rivers, and lakes were also selected. First, we investigated spectral separability using eight bands of satellite imagery for classification and the Jeffries-Matushita distance method (the integral of the

square of the normalised distance between a pair of classes was demonstrated by a value between 0 and 2) (Richards and Jia, 1999) (Table 2-S4). The tree, shrub-dry, shrub-moist, and dry-tussock sub-classes exhibited relatively small distances between each other (< 1.85). In addition, dry-tussock and cotton-sedge classes, as well as willows and alders, displayed small distances between each other (<1.85). From an ecosystem perspective, alder and willow were combined into the willow class as they exhibit similar spatial distributions (Schickhoff et al., 2002) and similar degrees of CH_4 flux. Three shrub subgroups (shrub-dry, shrub-moist, and dry-tussock from the site-scale vegetation survey) were also combined into the shrub class in this classification.

The separability of the cotton-sedge class from the dry-tussock sub-class was low (1.66). Although a difference in CH_4 emissions is expected to exist between these two classes, due to the difference in microtopography between them, we expect that this issue does not strongly affect the estimation of CH_4 emissions. In addition, we observed that the separability of the tree class from the shrub class was low (1.33–1.85). Therefore, we used an additional method of identification for the tree class, as described in S1.2.

2-3-4 Vegetation mapping and accuracy assessment with satellite data-derived classification

We finally created a vegetation map with reflectance features for the Indigirka lowland based on nine plant species-based vegetation classification classes following the MLC-DTC method, which had the highest overall accuracy (85%) and kappa statistics (0.83) (Table 2-S5). The accuracy was similar to the recently reported range for land cover classifications on similar permafrost landscapes in Canada, also created using WorldView-2 satellite images (Chasmer et al., 2014). In our study, producer accuracy (PA) and user accuracy (UA) for the tree, shrub, and willow classes indicated that the classification was not successful (Table 2-S6); however, these misclassifications—tree or shrub confused with willow—did not affect the estimation of local CH_4 emissions in practice, as these classes exhibited no CH_4 emissions (see section 2-3-5). In contrast, the high PAs of the *Sphagnum* spp., cotton-sedge, and emergent classes—from which CH_4 fluxes were substantially high—provided confidence in the estimation of local CH_4 emissions, although a small degree of error is expected due to possible misclassifications. Although the misclassification between the cotton-sedge and *Sphagnum* spp. classes was only approximately 10%, a larger error is expected in local estimations because of the differences in CH_4 flux (2.9 times higher in the cotton-sedge class than in the *Sphagnum* spp. class) and relatively large coverage area of the cotton-sedge class. Such error is also expected from the misclassification of the emergent class to the willow class (Table 2-S6) due to differences in CH_4 flux; however, the error should be small due to the small coverage area of the emergent class in our study area.

The accuracy of the classification system is discussed with four different methods: i) maximum-likelihood classification (MLC), ii) spectral information divergence (SID), iii) decision-tree classification (DTC), and iv) the combined method of MLC with DTC (MLC-DTC). The overall accuracies and the kappa statistics for these four methods are shown in Table 2-S5. Although the MLC yielded relatively high accuracies for mapping, the producer and user accuracies were lower than 50% for the tree class, as its spectral separability was low (Table 2-S4). The tree class in the MLC analysis also showed misclassifications of other classes, such as the willow, shrub, and emergent classes. Therefore, tree class pixels were discerned from the other classes by MLC-DTC using FDI and NDVI (Figure 2-S3).

In this study, we produced a local spatial scale vegetation map with high-resolution (0.5 m) satellite images using the MLC-DTC method (Figure 2-4). The overall accuracy (85%) and kappa statistics (0.83) of the classification were very high using this method, and were the highest of all the methods we applied (i.e., MLC, SID, DTC, MLC-DTC, and two spatial resolutions) (Table 2-S5). Here, we examined the practical aspects of the MLC-DTC method in greater detail. Producer accuracy (PA) and user accuracy (UA) for the tree class were better for the MLC-DTC method than for the other methods. In addition, PA and UA for the cotton-sedge class, which is the most important class for estimating CH_4 emissions (Fig 2-5), were the highest using the MLC-DTC method (Table 2-S5). As the overall accuracies and kappa statistics for SID, MLC, and DTC were much lower than those of the MLC-DTC methods, we concluded that the MLC-DTC method was the most suitable method for estimating local CH_4 emissions.

On the site-scale vegetation map of the Kodac site (K) at the 400 × 400 m area (Figure 2-2b), only eight vegetation classes could be discerned, as no lake class exists at the site scale. The cotton-sedge and willow classes were dominant, with 28% and 22% coverage, respectively, while the *Sphagnum* spp. class exhibited low coverage (9.1%), and the tree class displayed intermediate coverage (14.2%) (Table 2-2). This site-scale vegetation map showed that each vegetation class was distributed close to the others (Figure 2-2b). Similar patterns were also observed along the transect (Figure 2-2a), where vegetation zoning was observed (Figure 2-3).

The local-scale map covers the main flow of the Indigirka River, its floodplain, and the Kodac site (K) (Figure 2-4). The largest area (27%) was covered by the willow class, followed by the cotton-sedge class (23%) (Table 2-3). The river and emergent classes on the local-scale map exhibited higher coverage (15% and 9.5%, respectively) than on the site-scale map (7.9% and 2.2%, respectively). In comparison, the tree and shrub classes, which are typically found at elevation, exhibited lower coverage on the local-scale map (4.1% and 1.9%, respectively) than on the site-scale map (14% and 13%, respectively). The *Sphagnum* spp. class also exhibited low coverage on the local-scale map (1.9%).

2-3-5 CH_4 emissions from vegetation classes and the local-scale in the taiga-tundra boundary

The cotton-sedge and emergent classes exhibited the most substantial CH_4 emissions, with an average and SE of 114 ± 11 mg m^{-2} d^{-1} and 96 ± 29 mg m^{-2} d^{-1}, respectively (Table 2-3, Figure 2-5). The *Sphagnum* spp. class exhibited lower emissions (38 ± 9 mg m^{-2} d^{-1}) than the other wetland classes (i.e., cotton-sedge and emergent). In contrast, we detected a slight CH_4 sink with average fluxes in the tree class (forest floor) and bare-land class (−0.1 ± 0.2 mg m^{-2} d^{-1} and −3.4 ± 2.2 mg m^{-2} d^{-1}, respectively), and slight emissions in the shrub and willow classes (0.8 ± 0.7 mg m^{-2} d^{-1} and 0.3 ± 0.3 mg m^{-2} d^{-1}, respectively), although these values were below the detection limit of our chamber method (< 4.6 mg m^{-2} d^{-1}).

The lake class also emitted substantial quantities of CH_4 (21 ± 3.4 mg m^{-2} d^{-1}), using direct measurement by a floating chamber, whereas the river class emitted 2.6 ± 0.3 mg m^{-2} d^{-1} of CH_4, which was estimated using dissolved CH_4 concentrations (Figure 2-S7) oversaturated 20 to 51 times against the atmospheric equivalent, where the measured values were slightly higher than the detection limit (1.66 mg m^{-2} d^{-1}).

Local CH_4 emissions were estimated from the scaling of different flux rates in *in situ* chamber measurements (Figure 2-5, Table 2-3) to a local scale using a vegetation map (Figure 2-4, Table 2-3). The overall summary of monthly local emissions in the study area was 111 × 10^6 g CH_4 $month^{-1}$ during the growing season (July) from 2009 to 2016. The average ± SE CH_4 flux was 37 ± 10 mg m^{-2} d^{-1} at the local scale, and 38 ±9 mg CH_4 m^{-2} d^{-1} at the site scale.

2-4 Discussions

2-4-1 Classification scheme of vegetation mapping for precise estimation of local CH_4 emissions

In this study, we applied the MLC-DTC method based on plant species composition and reflectance features. In this way, shrublands and sedge wetlands—which are generally the dominant types of vegetation in arctic and subarctic regions (cf. Bartsch et al., 2016, Peregon et al., 2008, 2009, Terentieva et al. 2016)—were classified into shrub, willow, and cotton-sedge classes. We distinguished willow and shrub classes because of their differences in terms of species composition (Table 2-1, S1), vegetation heights (Table 2-S2), and reflectance (Figure 2-S5). Upright-type willows (*S. boganidensis*, *S. richardsonii*, and *S. alaxensis*) and alder (all approximately 2 m in height) composed tall and dense patches of willow class species, which were clearly different from that of the shorter shrub class. Previous studies frequently treated the *Sphagnum* spp. and emergent classes as a sub-category of another wetland category (Flessa et al., 2008; Schneider et al., 2009; Sjogersten and Wookey, 2009; Glagolev et al., 2011); however, in the present study, these classes were separated due to their very different CH_4 emission rates. The emergent vegetation was characterized by emergent aquatic species in a shallow water body (e.g. *A. fulva*) (Table 2-1 and S1), which have been recognized for their important contribution to regional CH_4 emissions in Alaska (Andresen et al.,

2017).

The distribution of vegetation primarily corresponds to microtopography and soil moisture features (Figure 2-3), relating to the seasonal thaw depth (i.e., active layer depth) and the frost table (Figure 2-S6, Table 2-S3). Therefore, assuming that vegetation mapping could be used as an indicator of these environmental factors, this classification could be potentially applied to the upscaling of CH_4 emissions and to other biogeochemical and hydrometeorological processes, such as biomass, net ecosystem exchange, and snowpack distribution controlled by vegetation and microtopography. However, for this vegetation mapping to be widely applied, the accuracies of the classifications of the tree, shrub, and willow classes need to be improved.

2-4-2 Vegetation coverage affected by microtopography regarding permafrost and hydrological conditions

Our mapping provided the spatial distributions of vegetation classes at a local scale (Figure 2-5), showing that the willow, cotton-sedge, and river classes covered large fractions of the landscape of the Indigirka River lowland (Table 2-3). The willow class, covering 26.8% of the landscape at the local scale, was typically documented along and/or surrounding the main stream of the Indigirka River. Willows generally form pure willow stands, with a height ranging from 0.5 m to 3 m (2 m on average, Table 2-S2), are thought to reproduce vegetatively, and display dense green leaves, as revealed in the reflectance measurements (Figure 2-S5). Previous research has shown that willow growth is controlled by thaw depth, especially in regions of continuous permafrost (Pajunen, 2009; Fan et al., 2018). It has also been reported that the structure and productivity of willow communities differs between several successional stages, which are affected by erosion and deposition from flooding events (Schickhoff et al., 2002). Therefore, we assumed that the extensively distributed willow class could be maintained by river flooding and by the wide spread effects of disturbance. This hypothesis is supported by the relatively large fractions of the river class and flat topography of this area. At the regional scale, expanding tall shrubs (alder) and increasing willow growth, which might be affected by climate change, have been observed in the Siberian Arctic (Forbes et al., 2010; Frost and Epstein, 2014; Fan et al., 2018). These growing trends might lead to the replacement of other types of wetland vegetation by willows, and, because there is insignificant CH_4 emission in willow stands, the extensive coverage of willow-dominated vegetation could exert a substantial impact on the local CH_4 emissions of the taiga–tundra boundary.

In the present study, the second largest area was covered by the cotton-sedge (22.7%) class and the fifth largest area by the emergent (9.5%) class, which exhibited higher coverage at the local scale than at the site scale (Table 2-3). Both classes were often located substantially far away from the main branch of the river on the local vegetation map (Figure 2-4). Although the cotton-sedge and emergent classes

sometimes formed pure patches, they were mostly adjacent to the *Sphagnum* spp., shrub, and willow classes, as described for vegetation mapping.

These mixed vegetation patches were also observed at site K and were explained by the effect of vegetation zoning on microtopography along the transect (Figure 2-3). At site K, where relatively drained polygon mires were recorded without open water ponds, the cotton-sedge class was located in the lowest and wettest position (Figure 2-3 and S5). The second lowest position was covered by *Sphagnum* spp. (Figure 2-3), which covers only a relatively small percentage (1.9 %) of the local-scale map, and includes *Sphagnum balticum* and *S. squarrosum*, thereby indicating the humid environment of a bog or poor fen (transitional mire) (Nicholson et al., 1996). Although *Sphagnum* spp. patches were often observed at site K (Figure 2-2b), this class covered a small portion of the local area vegetation map (Figure 2-4). These characteristics of site K could be explained by the relatively later stage of polygon development, where higher positions of the polygon were uplifted by underground ice growth and provided well-drained habitats for *Sphagnum* spp. and other mosses (de Klerk et al., 2011).

The tree and shrub classes, which characterize the northern limit of the taiga, exhibited patchy distributions and were located far from the main branch of the river (Figure 2-4) and from sites along the tributaries in the lowland (Figure 2-2b). The well drained, and higher position of polygon mires, which were approximately at 20–40 cm higher ground than the surrounding wetland, provides a suitable habitat for larch trees, according to on site observations (Figure 2-S2, 3, and S5). Another possible explanation for the topography of tree mounds (Figure 2-3) is that fluvial relief features, such as the natural levees of former river channels (Sidorchuk and Matveev, 1994; Sidorchuk et al., 2000), which contributed to the formation of mounds with geomorphologically narrow shapes, were located parallel to the present river channel (Figure 2-S8). At present, the conditions required for the survival of trees are regulated by the topography of the taiga-tundra boundary, and it is unknown whether the areas of tree mounds are changing or not.

The subsurface permafrost table is an important structural feature that helps maintaining a higher relative elevation with a shallower thaw depth on tree-mounds than on wetlands (Figure 2-S6, Table 2-S3). The higher frost table and higher ridge/mound structures of tree mounds provide drainage conditions for larch roots, thus preventing water logging. Well-drained soil also suppresses CH_4 production and emission, as almost no CH_4 emissions were observed in the tree and shrub classes (Fig. 6). It is interesting that the shallower thaw depth suited to larch growth, as shown in the present study, starkly contrasts with the deeper thaw depth observed along river banks, which are suitable habitats for white spruce growth in the forest-tussock tree lines of the tundra in Alaska, as both correspond to the low moisture of hydrological processes (Epstein et al., 2004). The regional characteristics of tree distribution in the eastern Siberian lowland might contribute to an ecosystem that is seriously vulnerable to climate change, as the elevation of the subsurface permafrost table—which could be strongly affected by recent increases in global temperatures—is one of the most important factors affecting suitable larch habitats.

2-4-3 Factors controlling local methane emissions in taiga-tundra boundary

Local CH_4 emissions were estimated from the scaling of the average values of fluxes in *in situ* chamber measurements (Figure 2-5, Table 2-3) multiplied by each vegetation class coverage (Figure 2-4, Table 2-3). These values were higher than regional estimations for the tundra (10.3 mg m^{-2} d^{-1}, Schneider et al., 2009; 20.6 mg m^{-2} d^{-1}, Sachs et al., 2010) of eastern Siberia, the forest-tundra (8.3 mg m^{-2} d^{-1}, modified from Glagolev et al., 2012) and north-taiga (21.3 mg m^{-2} d^{-1}, modified from Glagolev et al., 2012) and lower than the regional estimations for the arctic Swedish mires (89.8 mg m^{-2} d^{-1}, Nilsson et al., 2001) and boreal wetlands (59.4 mg m^{-2} d^{-1}) in western Siberia (Takeuchi et al., 2003). Regional differences in the up-scaling of CH_4 emissions might reflect differences in vegetation types, as well as the coverage of land cover types.

This up-scaling showed that the monthly CH_4 flux of the cotton-sedge class was 78×10^6 g CH_4 $month^{-1}$ and contributed 70% of the total local CH_4 emissions. The areas of the other CH_4 sources (i.e., the emergent, lake, *Sphagnum* spp., and river classes) were smaller, and they contributed less to local CH_4 emissions (25%, 2.8%, 1.9%, and 1.1%, respectively). In this study, wetland areas (including the cotton-sedge, emergent, and *Sphagnum* spp. classes) covered 38% of the total target area, which is relatively intermediate in comparison to the wetlands (in general) of other studies in the Arctic river lowland (66.6% in the region of the Lena delta; 13.8% at an island site in the Lena delta in East Siberia; 28% at forest-tundra, 31% in north-taiga and 41.4% at south-taiga in West Siberia) (Takeuchi et al., 2003; Schneider et al., 2009; Sachs et al., 2010; Peregon et al., 2009). Generally speaking, higher proportions of wetland area might lead to higher CH_4 emissions in a given landscape. However, in a regional study of the Lena delta, the highest degree of wetland coverage did not cause larger CH_4 emissions as a result of lower CH_4 fluxes (58.4–16.8 mg m^{-2} d^{-1}) in wet and moist vegetation classes (Schneider et al., 2009). Lower CH_4 fluxes in the Lena delta were caused by the limitation of the distributions of sedge-dominant vegetation patches in the tundra region, which were too small to scale up with the 30 m resolution of Landsat Images (Schneider et al., 2009). Differences in the scale of mapped resolutions renders regional comparisons of estimated CH_4 emissions difficult. Therefore, the definition of each vegetation class, which is usually limited by the spatial resolution of satellite imagery, is important for improving local to regional estimates of CH_4 emissions. The Indigirka lowland is heavily covered by cotton-sedge wetlands, which are part of a heterogeneous landscape, and which emit a large amount of CH_4, as described in section 2-3-5. Thus, it is necessary to fill the gap between different scales and resolutions, as well as that between the different classification schemes that are applied to upscaling, to analyse regional differences in ecosystems and CH_4 emissions.

The average fluxes in the cotton-sedge (114 ± 11 mg m^{-2} d^{-1}) and emergent (96 ± 29 mg m^{-2} d^{-1}) classes obtained here were nearly identical to the flux observed in the Lena delta tundra wetland in Eastern Siberia (94.1 mg m^{-2} d^{-1}) (Sachs et al., 2010), in the tall sedge in the arctic Swedish mire (104.8 ±59.2 mg^{-2} d^{-1}, Nilsson et al., 2001) and

sedge fen in the south boreal West Siberia (76.8±23.5 mg m^{-2} d^{-1}, Sabrekov et al., 2014). The flux in *Sphagnum* spp. (38 ± 9 mg m^{-2} d^{-1}) was approximately half of the average flux for cotton-sedge wetlands, and it was nearly identical to the flux in poor fen covered *Sphagnum* spp. in West Siberia (38.9±16.3mg m^{-2} d^{-1}, Sabrekov et al., 2014). Although the value reported here was lower than the flux values obtained for *Sphagnum* spp. cover in the Kytalyk tundra region (98 ± 74 mg CH_4 m^{-2} d^{-1}), similar differences in CH_4 flux between *Sphagnum* spp. and sedge wetlands—possibly caused by methanotrophic bacterial oxidation—have been previously reported (Parmentier et al., 2011b). Thus, the spatial differences in flux related to vegetation were successfully captured by our field observations.

Our observations were conducted on the warmest month (July), usually 3–4 weeks after snowmelt, because we wanted to determine the mean flux during the peak growing season. Therefore, the CH_4 flux recorded almost reflected the peak emission. There was a large inter-annual variation, which possibly depends on precipitation and soil moisture, as has been reported in the Arctic (Mastepanov et al., 2013, Shingubara et al., 2016, 2019). Therefore, monitoring of the temporal variations in CH_4 emissions with simultaneous meteorological factors is necessary to obtain further reliable estimations in the region.

The use of the manual chamber measurement method might cause potential biases. The accuracy and repeatability of *in situ* flux estimations may vary with chamber closure duration, sampling intervals, and chamber size and settings, and, therefore, the flux obtained by the manual chamber method may differ from that obtained by the continuous automatic chamber method that has more frequent intervals and shorter closure times (Mastepanov et al., 2013). The manual and automatic methods also differ in terms of practical applicability, particularly when used for simultaneous measurements in many locations. Thus, the method used for and the objective of flux measurements have to be taken into account when comparing flux rates.

Furthermore, the CH_4 flux attributed to the river class has been less frequently reported than that in wetland vegetation systems for the whole circumarctic region. The estimated river CH_4 flux in the downstream region of the Indigirka was 2.5 ± 1.1 mg m^{-2} d^{-1} in the present study, which was two times lower than the CH_4 flux observed in the Kuparuk River (6.24 mg CH_4 m^{-2} d^{-1}) (Kling et al., 1992) and the Middle Yukon River (5.76 mg CH_4 m^{-2} d^{-1}) (Striegl et al., 2012) in Alaska. In contrast, river CH_4 emissions were considered to be zero in the Lena river delta (Schneider et al., 2009), as dissolved CH_4 concentrations were below the detection limit (< 0.015 μmol L^{-1}) due to dilution by seawater (Semiletov et al., 2011). Regional differences in river CH_4 between the Lena river delta and the Indigirka downstream region could be explained by differences in water sources and factors related to geomorphology (i.e., stream order), as observed by Campeau and del Giorgio, (2014) and Campeau et al. (2014).

Our lake CH_4 flux (23 mg m^{-2} d^{-1}) was higher than that of rivers, but within the range of the diffusive and ebullition CH_4 fluxes (10.7 and 46.9 mg CH_4 m^{-2} d^{-1}, respectively) from thermokarst lakes with organic rich Edoma-type sediment in the Kolyma lowland (Walter et al., 2006). However, we did not consider the ebullition fraction of CH_4 emission, which could contribute from 10 to 90 % of the total emissions

from the surface of lakes in high latitudes, depending on the amount of organic matter in the sediment (Walter et al., 2006; Bastviken et al., 2011; Matveev et al., 2016). As the lakes observed in our study might be water-filled lakes (Marsh and Hey, 1989; Emmerton et al., 2007), the ebullition fraction could be lower than that previously documented by Walter et al. (2006), due to a lack of organic rich Edoma-type sediments under alluvial deposits.

Contrary to expectation, there was no significant CH_4 sink in the forest floor of the tree class (Fig. 6). In Siberia, forest CH_4 sink via microbial oxidation is affected by the tree species (Menyailo et al., 2010) and soil conditions related to the presence or absence of permafrost (Flessa et al., 2008). Both conditions are expected to exist in a larch forest with continuous permafrost, resulting in a smaller degree of CH_4 oxidation in comparison to other boreal forests. Indeed, the net CH_4 flux data for an eastern Siberian larch forest floor was estimated at -1.55 to -34 μg C m^{-2} h^{-1} (Morishita et al., 2003; Takakai et al., 2008; van Huissteden et al., 2008; Desyatkin et al., 2009), which was smaller than the CH_4 oxidation values reported for western Siberian birch-spruce-pine mixed forest (-60 to 0 μg C m^{-2} h^{-1}) (Flessa et al., 2008) and birch forest (-280 to -92 μg C m^{-2} h^{-1}) (Nakano et al., 2004). This effect also supports the regional CH_4 balance in boreal forest, although the net CH_4 uptake by the forest floor could only be 1–10% of the wetland flux (e.g., Morishita et al., 2003; Desyatkin et al., 2009). The CH_4 sink in our study (-0.1 ± 0.2 mg CH_4 m^{-2} d^{-1}) was less than that in the referenced data. Thus, it is not significant on local CH_4 balance. Indeed, the differences whether forest sink (value = -0.1) or no sink (value = 0) is very small in the average flux values in our study area; the local emissions ranged from 37.0 to 37.4 mg CH_4 m^{-2} d^{-1} at the local scale and 37.8 to 38.2 mg CH_4 m^{-2} d^{-1} at the site scale. From this perspective, the larch forest of the taiga–tundra boundary on a permafrost ecosystem might not currently have the potential for CH_4 balance, as the present fraction of tree cover is small compared to that of sedge and emergent wetland vegetation.

Settele et al. (2014) illustrated that the boreal-tundra biome has gradually shifted across temperature and moisture gradients, and this is facilitated by fire disturbance, permafrost thawing, insect disturbance, and drought stress. Indeed, summer temperature is positively correlated with increasing normalised difference vegetation index (NDVI) and tree ring width from 1938 to 2007 in NE Siberia (Berner et al., 2013) and tree-ring width from 1951 to 2012 at the same site (Tei et al., 2017), whereas a multidecadal regime of decreasing summer precipitation might have been reducing tree ring growth in this region from 1990 to 2012 (Tei et al., 2017). However, under the current conditions in the Indigirka lowland, changes in forest disturbance and mortality related to permafrost thaw and other factors were not obvious and the abundance of trees seems to be more closely linked to soil moisture and permafrost conditions across different microtopographies and landscapes.

The present study demonstrates the relative importance of spatially heterogeneous wetland emissions, which could provide fundamental data based on current sampling. We captured the spatial distribution of vegetation in the taiga-tundra boundary where tree expansion or mortality is expected. Wetland expansion and permafrost thaw have been mentioned as triggers for landscape-level CH_4 dynamics in

the Arctic (Johansson et al., 2006; Lara et al., 2015). At the same time, an increasing trend of forest greenness in northern Siberia has been reported through remote sensing observations (Frost and Epstein, 2014; Loranty et al., 2016). However, the increasing trend was not necessarily correlated with accelerated trend of tree radial growth (Berner et al., 2013; Tei et al., 2017). The authors reported that trend in tree radial growth depended on not only temperature but also precipitation regimes even in Arctic region. In recent decades, young larch trees and species from adjacent bioclimatic regions have been reported in this area (Khitun et al., 2016), indicating that it might be possible to change the ecosystem structure at the species level, and also the ecosystem function at the landscape level. The larch tree and shrub classes had close to zero CH_4 sink in this study, suggesting the weak ability of forests in the boundary ecosystem to oxidize CH_4 compared to a mature boreal forest. In contrast, the cotton-sedge, emergent, and *Sphagnum* spp. classes of wetlands were substantial CH_4 sources, similar to those in typical arctic tundra systems. The dynamics of the spatial distribution and CH_4 flux of the vegetation classes could be key for understanding local-regional responses to climate feedback. Therefore, CH_4 emissions at the taiga-tundra boundary should be monitored.

2-6 Concluding remarks

High-resolution satellite imagery provided a microtopographic level vegetation map, based on field observations, for upscaling local CH_4 emissions. The taiga-tundra boundary ecosystem of the Indigirka River lowland is covered by a high proportion of wetlands (cotton-sedge and emergent classes), resulting in larger local CH_4 emissions than that in the tundra located in the same region in north-eastern Siberia. Results from site- and local-scale vegetation mapping, validated by detailed field observations, indicated that site-scale hydrological conditions and geomorphological structures with rivers and permafrost could explain vegetation distribution patterns. High-resolution satellite images are indispensable for assessing local CH_4 emissions because of the highly heterogeneous vegetation and spatially varied CH_4 flux. Our findings indicate that tree distribution was spatially limited to small microtopographic elevations, and that forest CH_4 sink might not provide enough uptake to create a local balance in the taiga-tundra boundary lowland.

Figures and Tables

Table 2-1. Classes assigned by visual observation and final classes based on satellite image mapping. Plant species composition classes corresponding to microtopographies were categorized into six classes. Because of the similarity of species compositions, structures, and spectral features of satellite images among the shrub-dry, shrub-wet, and dry-tussock classes, and between the willow and alder classes, these classes were combined into the shrub class and the willow class, respectively. Bare-land, river, and lake classes were added, whereupon the landscape was finally grouped into nine classes.

Microtopographic classes		**Vegetation classes based on plant species composition**					**Vegetation classes for satellite-data based mapping**
		Plant community			Moss layer	Shrub and Herb layer	
		Classes	Clusters[f]	Clusters[g]			
Mound (High)	Tree	Tree	i	i, ii, iii	Green-moss[a]	*Larix cajanderi, Betula nana, Ledum palustre, Vaccinium vitis-idaea, Vaccinium uliginosum*	Tree
	Shrub	Shrub-dry[g]	iv, v	vi, vii	Green-moss[a]	*Betula nana, Ledum palstre, Rubus chamaemorus*	Shrub
		Shrub-moist[g]	vi, vii		Green-moss/*Sphagnum*-dry[b]	*Salix pulchra, Vaccinium uliginosum*	
		Dry-tussock[g]	viii		*Sphagnum*-dry[c]	*Carex aquatilis, Salix pulchra*	
Wet area (Low)	*Sphagnum*	*Sphagnum*	iii	xii	*Sphagnum*-wet[d]	*Carex aquatilis, Eriophorum vaginatum, Salix pulchra,*	*Sphagnum*
	Cotton-sedge	Cotton-sedge	ii	xi	*Sphagnum*-wet[d], Moss-wet[e]	*Eriophorum angustifolium, Comarum palstre*	Cotton-sedge
		Willow		ix	Green-moss[a], Moss-wet[e]	*Salix boganidensis*	Willow
		Alder		viii	Green-moss[a]	*Alnus fruticosa*	
		Emergent		x	Moss-wet[e]	*Equisetum spp. Arctophila fulva, Carex chordorrhiza*	Emergent
		Bare-land			No	No	Bare-land
		Lake/River			No	No	Lake/River

[a]Green-moss (*Tomentypnum nitens, Hylocomium splendens, Aulacomnium turgidum*).

[b]Green-moss/*Sphagnum*-dry mixed (Green-moss (as above) and *Sphagnum* spp. (*S. warnstorfii* and *S. girgensohnii*).

[c]*Sphagnum*-dry (Sphagnum spp. [*S. warnstorfii, S. girgensohnii*, and *S. balticum*]).

[d]*Sphagnum*-wet (*S. squarrosum* and *S. angustifolium*).

[e]Moss-wet (*Drepanocladus* spp., *Warnstorfia* spp.)

[f] Clusters in the site scale, numbered arbitrarily.

[g] Clusters in the local scale, numbered arbitrarily.

Table 2-2. Area and coverage of classification at the site scale (400 × 400 m).

Class	Area (km^2)	Coverage (%)
Cotton-sedge	0.045	28
Willow	0.035	22
Tree	0.023	14
Shrub	0.021	13
Sphagnum	0.015	9.1
River	0.013	7.9
Bare-land	0.006	3.5
Emergent	0.004	2.2
total	0.160	

Table 2-3. Methane emissions at the local scale were calculated using the observed CH_4 flux, and the area of each vegetation class obtained from the vegetation map. *In situ* CH_4 flux (230 observation in total) was observed from July 3 to August 9, 2009–2016. The sedge-dominated wetland contributes 70% of total emissions.

Class	Area (km^2)	Coverage%	Observed mean CH_4 flux ($mg\ m^{-2}\ d^{-1}$)[a]	SE	N	Days	Estimated local CH_4 emission (10^6 g CH_4 $month^{-1}$)	CH_4 contribution%
Willow	26	27	0.3	0.3	17	5	0.3	0.2
Cotton-sedge	22	23	114	11	90	36	78	70
River	14	15	2.6[b]	0.3	18	2	1.1	1.0
Emergent	9.2	9.5	96	29	14	4	27	25
Shrub	8.0	8.3	0.8	0.7	8	3	0.2	0.2
Bare-land	6.8	7.0	-3.4	2.2	7	2	-0.7	-0.6
Lake	4.6	4.8	25	3.4	3	2	3.6	2.8
Tree	4.0	4.1	-0.1	0.2	49	23	0.0	0.0
Sphagnum	1.8	1.9	38	8.9	24	17	2.2	1.9
Total	**96**		**37**[c]	**9.8**	230	94	111	

[a]Methane flux observed by the calculation of the average of chamber measured values. Data shown are averages ± standard error (SE), with the repeated number of total flux measurements (N) and the observation days (Days).

[b]River methane flux was estimated from river dissolved CH_4 concentrations and transfer velocity (2-2-9, Figure 2-S7).

[c]Average local CH_4 flux per square meter per day (mg CH_4 m^{-2} d^{-1}).

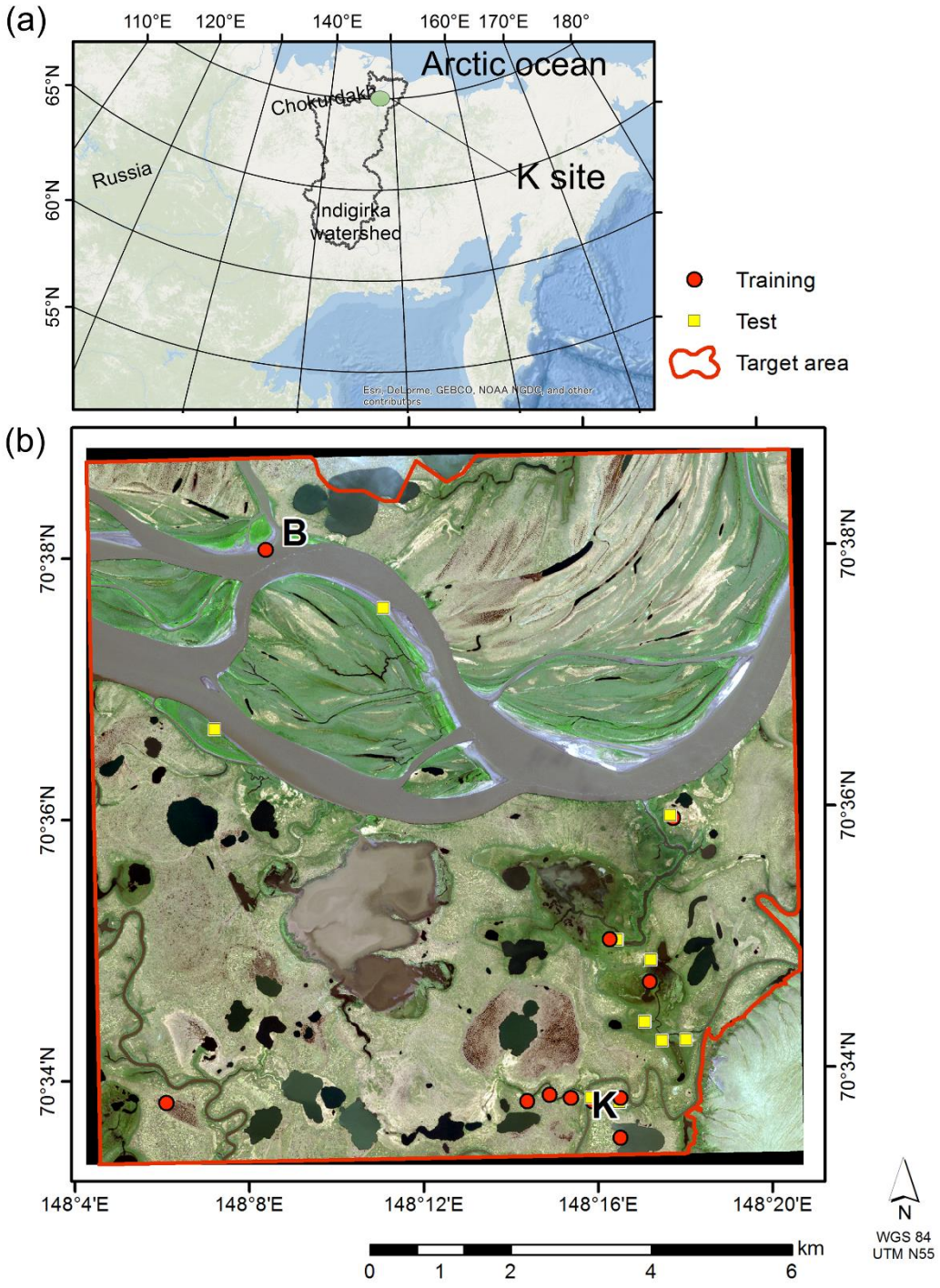

Figure 2-1. (a) Regional and (b) Local position of the study site. The Indigirka lowland is located in the north area of the watershed (Google Maps). WorldView-2 satellite image covered an area of 10 × 10 km (true colour). The main branch of the Indigirka River lies in the upper part of the image. The locations of the Kodac site (K), B site (B), local surveyed plot for training (circle), and test pixels (rectangular) are plotted on the map. Each survey point contains 3–4 quadrats for vegetation surveys. Vegetation was mapped within a target area (red line) without hills and cloudy areas.

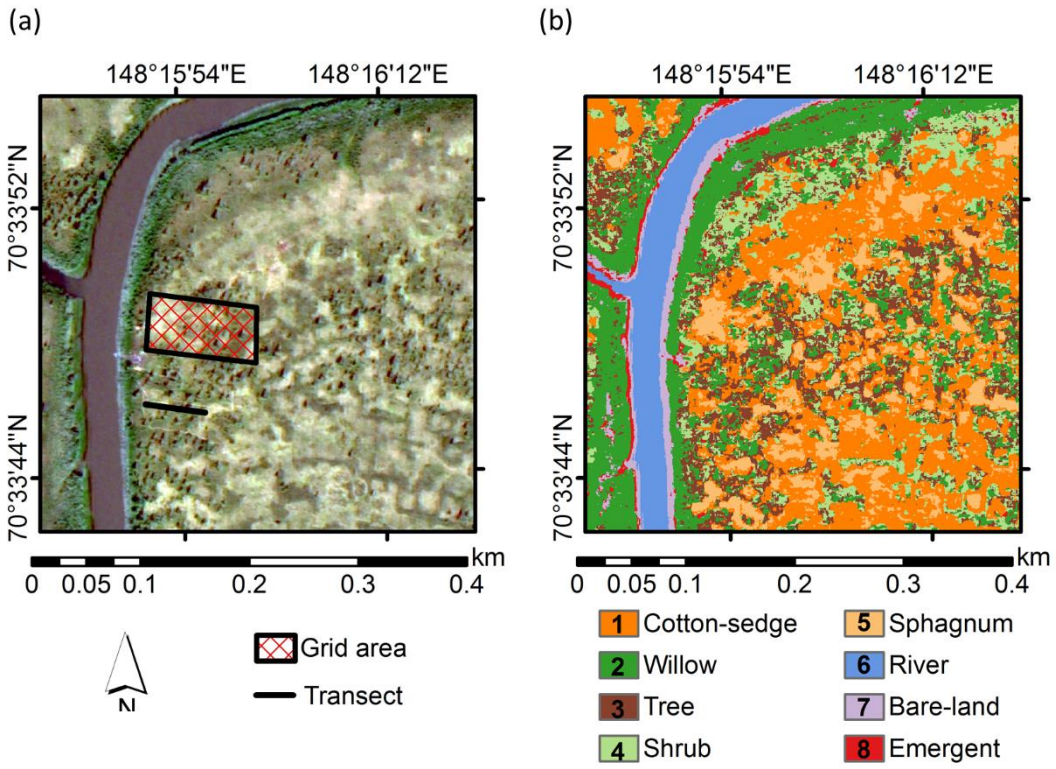

Figure 2-2. (a) True color image and (b) vegetation map classified into nine classes on a site scale (400 × 400 m) at K site. The lake class do not appear at this scale, and the map was covered by eight classes as shown in (b).

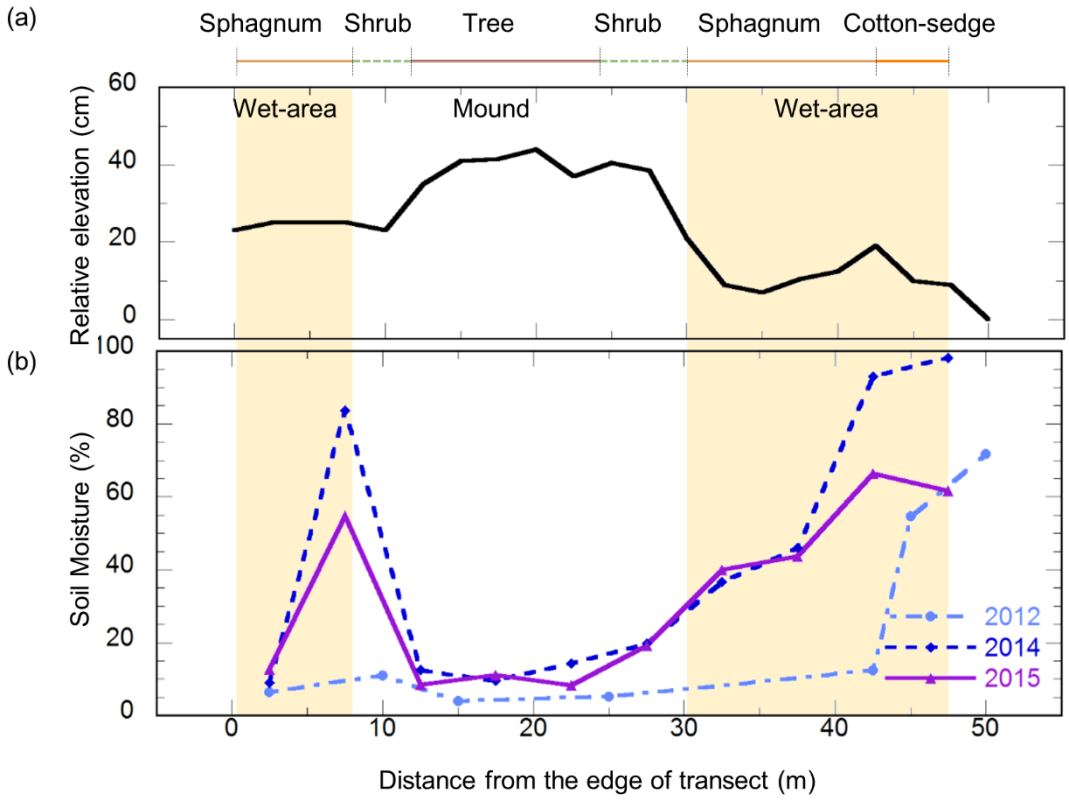

Figure 2-3. Vegetation, relative elevation (a), and soil moisture (b) along a 50-m transect. Soil moisture was measured as the averaged volumetric water content at the surface (0–8 cm) by time domain reflectance on July 12, 2012, July 15, 2014, and July 12, 2015. *Sphagnum* spp. and cotton-sedge areas are hatched to illustrate potential CH_4 sources.

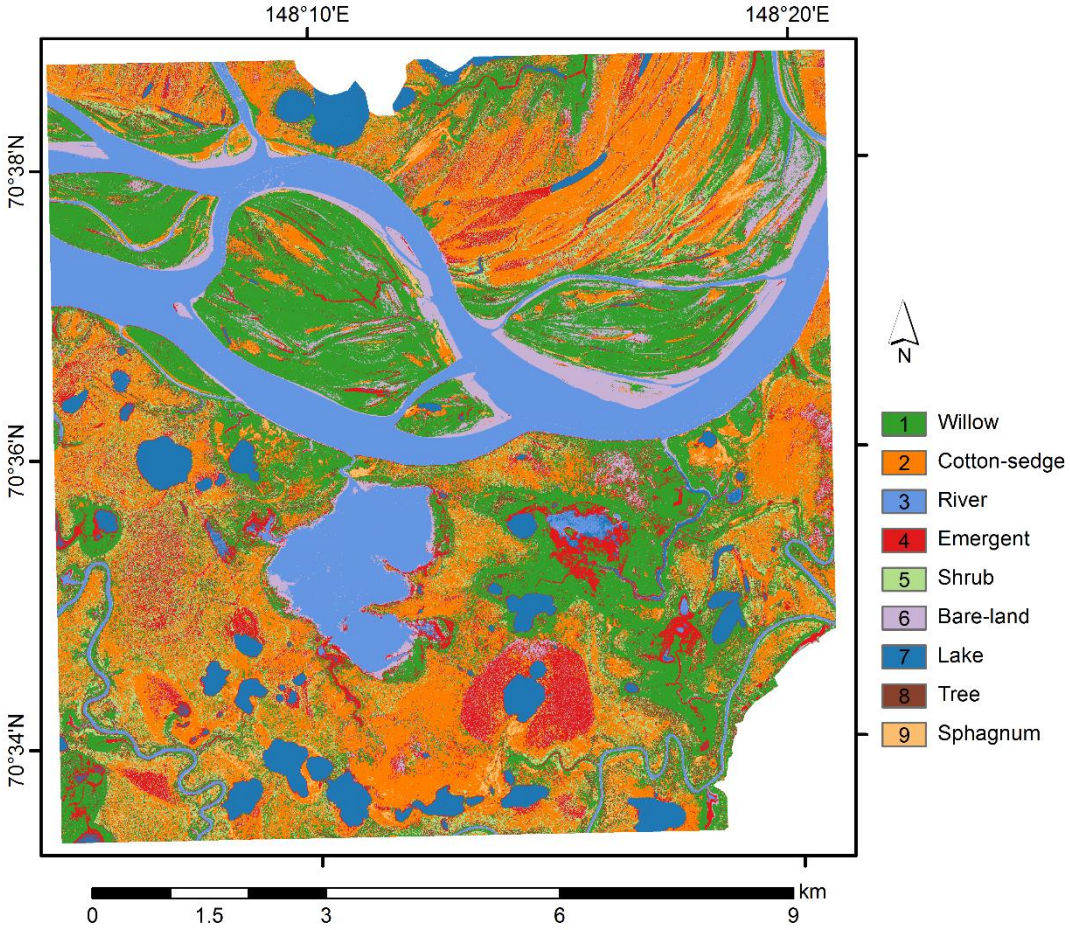

Figure 2-4. Vegetation map showing the nine classes at the local scale (10 × 10 km) obtained by the MLC-DTC (maximum-likelihood classification and decision tree classification combined) method.

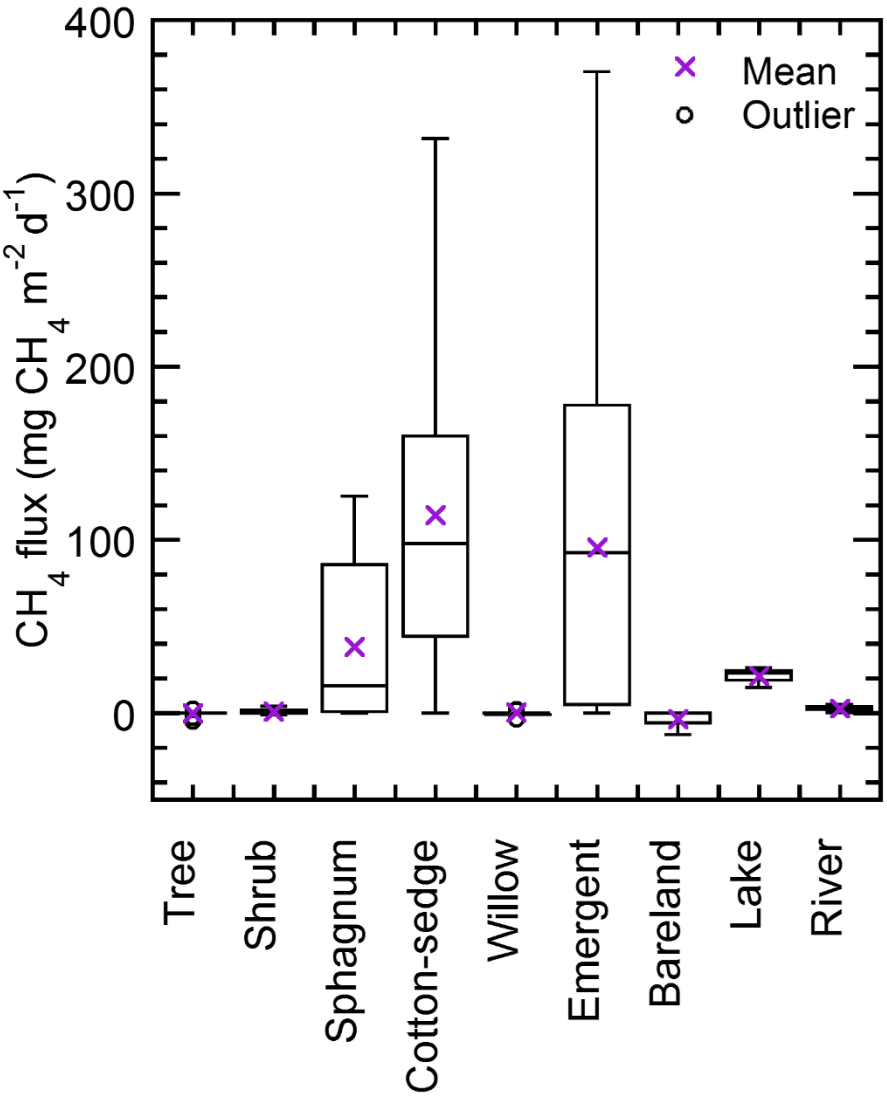

Figure 2-5. *In situ* CH_4 flux measured by the chamber method in 2009–2016 during the summer growing season (July 3–Aug 9, 2009–2016, n (total) = 230). Only river CH_4 flux was derived from dissolved CH_4 concentration using the diffusive fraction with the transfer velocity method. Details are shown in the method and Figure 2-S7.

Additional Tables and Figures for Chapter 2

Table 2-S1. Species appearance frequency (%) among 16 vascular plants and five groups of moss species in each cluster with vegetation class of Kodac site (K) vegetation survey. Total 231 plots were clustered into eight (i–viii) in Figure 2-S1.

Cluster	i	ii	iii	iv	v	vi	vii	viii
n (combinations)	17	2	16	8	18	12	6	15
Class	Tree	Cotton-sedge	*Sphagnum*	Shrub-dry	Shrub-dry	Shrub-moist	Shrub-moist	Dry-tussock
n (plots)	29	3	58	19	54	24	8	36
Averaged specific elevation (cm)	33.1	15.7	10.5	26.2	29.5	19.6	14.4	16.3
SD	5.6	4.7	5.7	3.4	4.4	3.8	2.3	4.9
Averaged thaw depth (cm)	20.1	30.7	29.3	21.8	20	23.1	23.6	24.5
SD	14.8	18.3	12.5	14.4	12.7	14.1	13.1	11.5
Averaged frozen ground height (cm)	13	-15	-19	4.4	9.5	-3.5	-9.3	-8.3
SD	14.7	22.7	16.2	14.3	14.6	16	14.8	13.6
SPECIES/ Species appearance frequency (%)								
Green-moss[a]	94.1	0.0	0.0	100.0	100.0	0.0	0.0	0.0
Green-moss/*Sphagnum*-dry mixed[b]	5.9	0.0	0.0	0.0	0.0	100.0	0.0	0.0
Sphagnum-dry[c]	0.0	0.0	0.0	0.0	0.0	0.0	100.0	100.0
Sphagnum-wet[d]	0.0	0.0	100.0	0.0	0.0	0.0	0.0	0.0
Moss-wet[e]	0.0	100.0	0.0	0.0	0.0	0.0	0.0	0.0
Vaccinium uliginosum	17.6	0.0	0.0	12.5	27.8	8.3	16.7	6.7
Ledum decumbens	17.6	0.0	0.0	25.0	5.6	16.7	16.7	26.7
Betula nana	70.6	0.0	12.5	12.5	77.8	25.0	100.0	6.7
Salix pulchra	23.5	0.0	25.0	0.0	44.4	33.3	50.0	46.7
Eriophorum vaginatum	5.9	0.0	25.0	50.0	33.3	33.3	0.0	60.0
Eriophorum angustifolium	0.0	100.0	50.0	0.0	0.0	0.0	0.0	0.0
Carex aquatilis	0.0	50.0	87.5	12.5	5.6	25.0	66.7	33.3
Comarum palustre	0.0	100.0	25.0	0.0	0.0	0.0	0.0	0.0
Rubus chamaemorus	35.3	0.0	0.0	87.5	5.6	25.0	0.0	33.3
Vaccinium vitis-idaea	17.6	0.0	0.0	0.0	0.0	0.0	0.0	0.0

Larix cajanderi (sapling)	11.8	0.0	0.0	12.5	0.0	0.0	0.0	0.0
Empetrum nigrum	0.0	0.0	0.0	0.0	5.6	0.0	0.0	0.0
Arctagrostis latifolia	0.0	0.0	0.0	0.0	5.6	0.0	0.0	0.0
Polemonium acutiflorum	0.0	0.0	6.3	0.0	0.0	0.0	0.0	0.0
Alnus fruticosa	11.8	0.0	0.0	0.0	5.6	0.0	0.0	0.0
Larix cajanderi (>2 m height tree)	100.0	0.0	0.0	0.0	0.0	0.0	0.0	0.0

[a] Green-moss: *Tomentypnum nitens, Hylocomium splendens, Aulacomnium turgidum*

[b] Green-moss/*Sphagnum*-dry mixed: Green-moss (as above) and *Sphagum* spp. (*S. warnstorfii* and *S. girgensohnii*),

[c] *Sphagnum*-dry*: Sphagum* spp. (*S. warnstorfii, S. girgensohnii, S. balticum and S. angustifolium*)

[d] *Sphagnum*-wet: *S. squarrosum*

[e] Moss-wet: *Drepanocladus spp., Warnstorfia* spp.

Table 2-S2. Species appearance frequency (%) among 71 species in each cluster with vegetation class of local area vegetation survey (10 x 10 km). Appearances of species at 64 plots were clustered into 12 (i–xii) in Figure 2-S2. Then, eight vegetation classes were identified by similarity of species composition with supporting information of vegetation height, surface (0–8 cm) soil moisture and CH_4 flux (shown in Figure 2-S6).

Cluster	i	ii	iii	iv	v	vi	vii	viii	ix	x	xi	xii
n (number of plots in a cluster)	5	4	3	3	3	4	5	6	12	7	6	8
Class		Tree		Lichen-heath		Shrub		Alder	Willow	Emergent	Cotton-Sedge	*Sphagnum*
Height of vegetation(m)	8	5	6	0.4	nd	nd	0.9	2	1.9	nd	0.75	nd
SD of height	0	0	0	0			0	0	1.2		0.2	
n	1	3	1	1			1	2	7		2	
Soil moisture (%)	9.8	16	16	11.6	21.1	19.8	nd	14	39.4	89.1	69	92.7
SD of moisture	9.3	8.1	8.1	10.3	6	4		6.6	21.8	5.7	29.3	20.4
n	4	8	4	4	8	4		4	20	4	8	12
SPECIES/ Species appearance frequency (%)												
Hylocoium splendens	80.0	50.0	100.0	66.7	0.0	50.0	100.0	100.0	0.0	0.0	0.0	0.0
Aulacomnium turgidum	80.0	75.0	100.0	33.3	33.3	25.0	100.0	83.3	0.0	0.0	16.7	50.0
Tomentypnum nitens	0.0	0.0	33.3	66.7	0.0	25.0	20.0	33.3	8.3	0.0	0.0	12.5
Sphagnum sec. *Acutifolia*[a]	0.0	25.0	0.0	33.3	0.0	0.0	0.0	0.0	0.0	0.0	0.0	25.0
Sphagnum balticum	0.0	0.0	0.0	0.0	0.0	0.0	0.0	0.0	0.0	0.0	0.0	12.5
Sphagnum squarrosum	0.0	0.0	0.0	0.0	0.0	0.0	0.0	0.0	0.0	0.0	33.3	62.5

Table 2-S2

Sanionia sp.	0.0	0.0	0.0	0.0	0.0	75.0	0.0	0.0	25.0	0.0	0.0	0.0
Polytrichum sp.	0.0	75.0	0.0	0.0	66.7	50.0	0.0	0.0	0.0	0.0	0.0	0.0
Rhizomnium sp.	0.0	0.0	0.0	0.0	0.0	0.0	0.0	0.0	8.3	0.0	16.7	12.5
Aulacomnium palstre	0.0	50.0	0.0	0.0	0.0	0.0	0.0	33.3	0.0	0.0	0.0	0.0
Ptilidium sp.	0.0	25.0	0.0	0.0	0.0	0.0	0.0	16.7	0.0	0.0	0.0	0.0
Equisetum arvens	20.0	0.0	0.0	0.0	0.0	25.0	0.0	0.0	83.3	0.0	0.0	0.0
Salix glauca	40.0	0.0	0.0	0.0	0.0	0.0	100.0	0.0	16.7	0.0	0.0	0.0
Salix richardsonii	0.0	0.0	0.0	0.0	0.0	0.0	80.0	0.0	50.0	14.3	33.3	0.0
Salix pulchra	40.0	75.0	66.7	0.0	33.3	100.0	40.0	50.0	8.3	14.3	100.0	25.0
Comarum palstre	0.0	0.0	0.0	0.0	0.0	0.0	0.0	0.0	8.3	14.3	50.0	100.0
Vaccinium uliginosum	60.0	0.0	100.0	100.0	100.0	75.0	100.0	100.0	16.7	0.0	33.3	12.5
Eriophorum angustifolium	0.0	0.0	0.0	0.0	0.0	0.0	0.0	0.0	8.3	28.6	83.3	87.5
Calamagrostis neglecta	20.0	25.0	0.0	33.3	0.0	25.0	0.0	0.0	25.0	0.0	66.7	0.0
Alnus fruticosa	20.0	25.0	0.0	33.3	0.0	25.0	20.0	83.3	8.3	0.0	0.0	0.0
Alopeculus alpinus	0.0	0.0	0.0	0.0	0.0	0.0	0.0	0.0	16.7	0.0	0.0	0.0
Allium strictum	0.0	0.0	0.0	0.0	0.0	0.0	20.0	0.0	0.0	0.0	0.0	0.0
Moehringia laferiflora	0.0	0.0	0.0	0.0	0.0	25.0	0.0	0.0	8.3	0.0	0.0	0.0
Salix hastata	0.0	0.0	0.0	0.0	0.0	0.0	0.0	0.0	16.7	0.0	0.0	0.0
Salix boganidensis	0.0	0.0	0.0	0.0	0.0	25.0	0.0	0.0	66.7	0.0	0.0	0.0
Salix alaxensis	0.0	0.0	0.0	0.0	0.0	0.0	0.0	0.0	33.3	0.0	0.0	0.0
Caltha arctica	0.0	0.0	0.0	0.0	0.0	0.0	0.0	0.0	16.7	0.0	0.0	0.0
Eriophorum vaginatum	0.0	25.0	0.0	0.0	33.3	0.0	0.0	0.0	0.0	28.6	0.0	37.5
Carex aquatilis stans	0.0	0.0	0.0	0.0	0.0	0.0	0.0	16.7	8.3	85.7	16.7	62.5

Table 2-S2

Carex saxatilis	0.0	0.0	0.0	0.0	0.0	0.0	0.0	0.0	0.0	0.0	0.0	25.0
Carex vaginatum	0.0	0.0	66.7	33.3	33.3	0.0	0.0	0.0	0.0	0.0	33.3	0.0
Carex rotundata	0.0	0.0	0.0	0.0	0.0	0.0	0.0	0.0	8.3	14.3	0.0	0.0
Carex chordorrhiza	0.0	0.0	0.0	0.0	0.0	0.0	0.0	0.0	0.0	0.0	0.0	25.0
Luzula confusa	0.0	0.0	33.3	33.3	33.3	0.0	0.0	0.0	0.0	0.0	0.0	0.0
Arctagrostis latifolia	0.0	75.0	100.0	0.0	33.3	0.0	60.0	66.7	0.0	0.0	16.7	12.5
Arctophila fulva	0.0	0.0	0.0	0.0	0.0	0.0	0.0	0.0	0.0	28.6	0.0	0.0
Deschampsia borealis	0.0	0.0	0.0	0.0	0.0	0.0	0.0	0.0	8.3	0.0	0.0	0.0
Poa alpigena	20.0	0.0	0.0	0.0	0.0	0.0	0.0	0.0	0.0	0.0	0.0	0.0
Poa tolmatchewii	60.0	25.0	33.3	33.3	66.7	0.0	0.0	16.7	8.3	0.0	0.0	0.0
Poa arctica	0.0	0.0	0.0	0.0	0.0	0.0	0.0	0.0	16.7	0.0	0.0	0.0
Ranunculus pallasii	0.0	0.0	0.0	0.0	0.0	0.0	0.0	0.0	0.0	0.0	0.0	12.5
Rananculus reptans	20.0	0.0	0.0	0.0	0.0	0.0	0.0	0.0	8.3	0.0	0.0	0.0
Ranunculus lapponicum	0.0	0.0	0.0	0.0	0.0	25.0	0.0	0.0	0.0	0.0	0.0	0.0
Menyanthes trifoliata	0.0	0.0	0.0	0.0	0.0	0.0	0.0	0.0	0.0	0.0	0.0	0.0
Hippuris vulgaris	0.0	0.0	0.0	0.0	0.0	0.0	0.0	0.0	0.0	14.3	0.0	0.0
Stellaria peduncularis	40.0	25.0	33.3	0.0	0.0	0.0	0.0	0.0	0.0	0.0	0.0	0.0
Chamaedaphne calyculata	0.0	0.0	0.0	0.0	0.0	0.0	0.0	0.0	0.0	0.0	0.0	12.5
Petasites frigidus	0.0	0.0	33.3	0.0	0.0	0.0	0.0	0.0	8.3	0.0	0.0	0.0
Rubus chamaemorus	20.0	100.0	100.0	0.0	0.0	0.0	0.0	33.3	0.0	0.0	0.0	0.0
Saxifraga hirculus	0.0	0.0	0.0	0.0	0.0	0.0	20.0	0.0	0.0	0.0	0.0	0.0
Saxifraga nelsoniana	0.0	0.0	0.0	33.3	33.3	0.0	0.0	0.0	0.0	14.3	0.0	0.0
Pedicularis labradorica	0.0	0.0	0.0	0.0	0.0	25.0	0.0	0.0	0.0	0.0	0.0	0.0

Table 2-S2

Pedicularis palustris	0.0	0.0	33.3	0.0	33.3	0.0	20.0	0.0	8.3	0.0	0.0	12.5
Betula nana	40.0	100.0	100.0	100.0	33.3	50.0	40.0	100.0	8.3	14.3	16.7	0.0
Vaccinium vitis-idaea	40.0	100.0	100.0	66.7	33.3	0.0	20.0	0.0	0.0	0.0	0.0	0.0
Ledum decumbens	0.0	75.0	66.7	100.0	66.7	50.0	0.0	0.0	0.0	0.0	0.0	0.0
Arctous alpina	20.0	0.0	0.0	33.3	100.0	25.0	20.0	0.0	0.0	0.0	0.0	0.0
Empetrum nigrum	0.0	25.0	0.0	0.0	66.7	0.0	0.0	16.7	0.0	0.0	0.0	0.0
Dryas punctata	0.0	0.0	33.3	33.3	100.0	0.0	0.0	0.0	0.0	0.0	0.0	0.0
Cassiope tetragona	0.0	0.0	0.0	100.0	33.3	0.0	0.0	0.0	0.0	0.0	0.0	0.0
Andromeda polifolia	0.0	0.0	0.0	0.0	0.0	0.0	0.0	0.0	0.0	14.3	0.0	0.0
Orthilia secunda	20.0	25.0	33.3	33.3	0.0	0.0	0.0	0.0	8.3	0.0	0.0	0.0
Pyrola rotundifolia	60.0	0.0	66.7	0.0	0.0	75.0	60.0	50.0	0.0	0.0	0.0	0.0
Valeriana capitata	40.0	0.0	33.3	0.0	0.0	0.0	0.0	33.3	0.0	0.0	0.0	0.0
Astragalus alpinus	0.0	0.0	0.0	0.0	0.0	75.0	0.0	0.0	0.0	0.0	0.0	0.0
Tofieldia cernua	0.0	0.0	0.0	66.7	0.0	0.0	0.0	0.0	0.0	0.0	0.0	0.0
Bistorta vivipala	0.0	0.0	66.7	100.0	0.0	0.0	0.0	0.0	0.0	0.0	0.0	0.0
Aconogonon tripterocarpum	0.0	0.0	66.7	0.0	0.0	0.0	20.0	0.0	0.0	0.0	0.0	0.0
Hierochroe sp.	0.0	0.0	0.0	0.0	33.3	0.0	0.0	0.0	0.0	0.0	0.0	0.0
Polemonium acutiflorum	0.0	0.0	0.0	0.0	0.0	0.0	0.0	0.0	0.0	0.0	0.0	0.0
Larix cajanderi (>2 m height tree)	80.0	100.0	100.0	0.0	0.0	0.0	0.0	0.0	0.0	0.0	0.0	0.0

[a]*Sphagnum* sec. Acutifolia include *S. warnstorfii* and *S. girgensohnii*. Both species were usually appeared at same patch.

Table 2-S3. Statistical significance of differences in the relative elevation of each cluster in the Kodac site (K) vegetation survey. Significances were calculated by single factor ANOVA among clusters and t-test between a pair of clusters.

ANOVA	SS	df	MS	F	P-value	F critical
Between groups	16354	7	2336	13.6	**<0.0001**	2.05
Within groups	38423	223	172			
sum	54777	230				

Vegetation classes	Tree	Shrub-dry		Shrub-moist		Dry-tussock	Sphagnum	Cotton-sedge
Clusters	i	v	iv	vi	vii	viii	iii	ii
i								
v	0.249							
iv	0.118	0.351						
vi	**0.001**	**0.003**	0.137					
vii	**0.003**	**0.003**	0.056	0.366				
viii	**< 0.001**	**< 0.001**	**0.007**	0.320	0.686			
iii	**< 0.001**	**< 0.001**	**< 0.001**	**0.005**	0.417	0.028		
ii	0.067	0.077	0.265	0.663	0.898	0.936	0.496	

Note Relative elevation values of cluster (i) and (v) were significantly different from lower clusters (vi–viii and iii). Cluster (iii), which was dominated by sphagnum, showed significantly different from shrub dominated clusters (iv–vii), and they were bolded. Clusters (v) and (iv), and clusters (vi) and (vii) were similar, thus combined into Shrub-dry class and Shrub-moist class, respectively.

Table 2-S4. Separability of spectra among vegetation classes in training pixel. Jefferies-Matushita statistics were calculated for spectral separability evaluation. Alnus and Shrub subgroups (Shrub-dry, Shrub-moist, Dry-tussocks) were low separability (<1.85) among other vegetation classes, and filled by yellow.

Vegetation classes	Tree	Shrub-dry	Shrub-moist	Dry-tussock	Sphagnum	Cotton-sedge	Willow	Alder	River	Bare-land	Lake	Emergent
Tree												
Shrub-dry	1.85											
Shrub-moist	1.63	1.33										
Dry-tussock	1.50	1.83	1.58									
Sphagnum	2.00	2.00	2.00	2.00								
Cotton-sedge	1.88	1.98	1.92	1.66	1.93							
Willow	1.99	2.00	2.00	2.00	2.00	2.00						
Alder	1.94	1.93	1.97	1.96	2.00	2.00	1.83					
River	2.00	2.00	2.00	2.00	2.00	2.00	2.00	2.00				
Bare-land	1.99	2.00	2.00	2.00	2.00	2.00	2.00	2.00	2.00			
Lake	2.00	2.00	2.00	2.00	2.00	2.00	2.00	2.00	2.00	2.00		
Emergent	1.95	2.00	2.00	2.00	2.00	2.00	2.00	2.00	2.00	2.00	2.00	

Table 2-S5. Accuracy of classification for various classification methods on a local scale (10 × 10 km). The overall accuracy is the ratio of correct sample number to total number. The kappa statistic is normalised, which accounts for the non-diagonal element of the confusion matrix.

Method	Resolution (m)	Overall accuracy (%)	Kappa
MLC	2.0	73	0.69
MLC	0.5	77	0.73
SID	0.5	50	0.44
DTC	2.0	59	0.53
MLC-DTC	0.5	85	0.83

Table 2-S6. Confusion matrix of maximum-likelihood classification and decision-tree classification combined, and independent ground truth test pixels at a local scale (10 × 10 km). The accuracy of the vegetation map was evaluated.

Class	Tree	Shrub	Sphagnum	Cotton-sedge	Willow	River	Bare-land	Lake	Emergent	Total	[b]User accuracy (%)
Tree	197	77	0	7	16	0	0	0	0	297	66
Shrub	16	191	0	1	0	0	0	0	0	208	92
Sphagnum	3	0	634	60	0	0	0	0	0	697	91
Cotton-sedge	2	0	65	472	0	0	0	0	0	539	88
Willow	416	274	0	0	967	0	0	0	521	2178	44
River	0	0	0	0	0	2732	0	0	0	2732	100
Bare-land	7	0	0	0	1	0	1916	0	27	1951	98
Lake	0	0	0	0	0	0	0	218	0	218	100
Emergent	0	0	0	0	0	0	0	76	1887	1963	96
Total	641	542	699	540	984	2732	1916	294	2435	10783	
[a]Producer accuracy (%)	31	35	91	87	98	100	100	74	77		

Note User and field sample accuracy was high enough for cotton-sedge, *Sphagnum*, water, bare land and emergent classes, while accuracy for the tree, shrub and willow classes was low. Pixels were misclassified as willow (from the tree class and the emergent class) and as tree (from the shrub class).

[a]Producer accuracy (PA: among test pixels of a class, percentage of number of pixels which were correctly classified). [b]User accuracy (UA: among test pixels classified into a class, percentage of number of pixels, which were correctly classified)

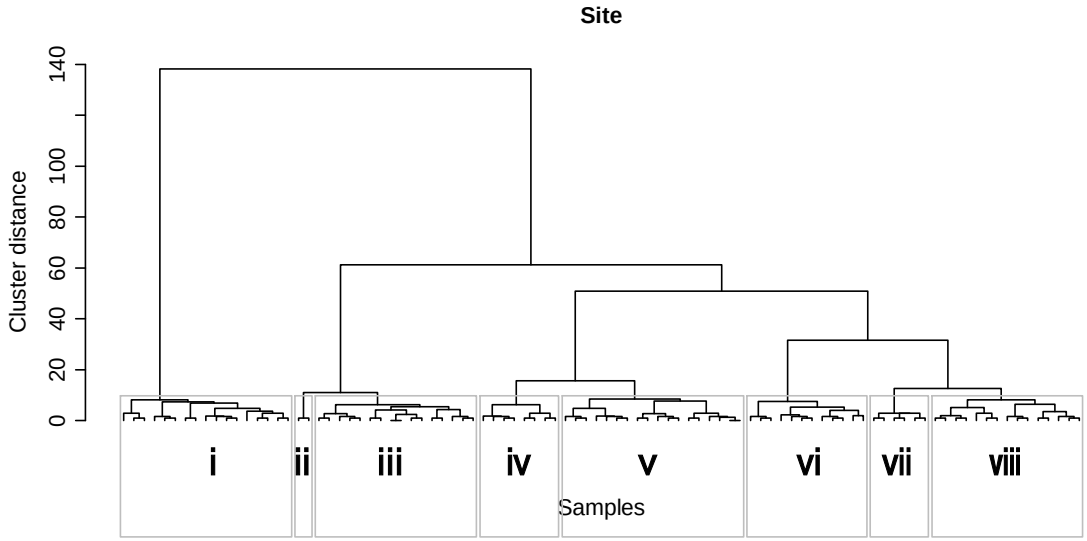

Figure 2-S1. Clustering dendrogram of plant community based on species appearance in site vegetation surveys at 231 plots (Table 2-S2). Eight clusters (i–viii) were distinguished by 14 species and five groups. Cluster (i) was characterized by *Larix cajanderi* (emphasized by *Larix* appearance values three times larger than those of other species). Cluster (ii) was characterized by *Eriophorum angustifolium* and *Comarum palstre* with Moss-wet species (*Drepanocladus* spp. and *Warnstorfia* spp.) as mentioned in Table 2-S2. Cluster (iii) was characterized by sphagnum (*Sphagnum balticum, S. squarrosum* etc.) and *Salix pulchra*. Clusters (iv) and (v) were dominated by Green moss with shrub species, cluster (vi) and (vii) were dominated by Salix and Sphagnum dry, and Cluster (viii) was dominated by tussock sedge (*Eriophorum vaginatum*) with Ledum and Sphagnum dry.

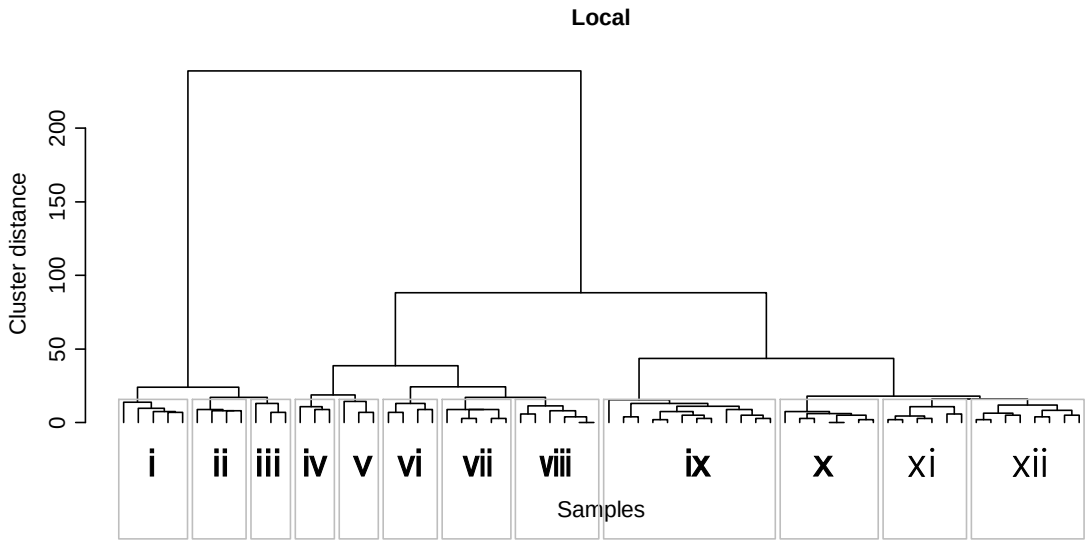

Figure 2-S2. Clustering dendrogram of plant community based on species appearance in local vegetation surveys at 64 plots (Table 2-S1). Twelve clusters (i–xii) were distinguished by 71 species. Appearance of *Larix* were emphasized to classify the site into clusters (i), (ii) and (iii) as like clustering with site data (emphasized by *Larix* appearance values twice as large as those of other species). Clusters (iv) and (v) were designated with *Ledum decumbens, Dryas punctate* and *Luzula confusa*. Clusters (vi) and (vii) were designated with *Betula nana*, *Vaccinium uliginosum* and *Pyrola rotundifolia*. Cluster (viii) was designated with *Alnus fruticosa, Betula nana* and *Hylocomnium splendens*, and Cluster (ix) was designated with tall bush type willow species (*Salix boganidensis, richardsonii* and others). Cluster (x) was characterized by *Arctophila fulva* or *Carex chordorrhiza*, and Clusters (xi) and (xii) were characterized by *Sphagnum squarrosum, Eriophorum angustifolium* and *Salix pulchra*.

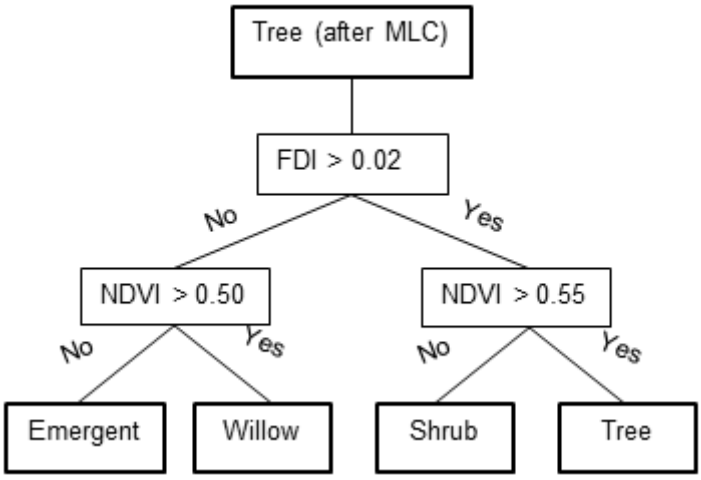

Figure 2-S3. Decision tree criteria applied to MLC-DTC (Maximum likelihood method – Decision tree combined) method. After classification by MLC, the tree class was subdivided into four; emergent, willow, shrub and tree, which were classes misclassified, as indicated by the confusion matrix of MLC (Table 2-S5). Lower FDI and lower NDVI pixels were removed from the original tree class in MLC. In the first step, two groups were separated by a threshold FDI value of 0.02. In the second step, the high-FDI group was separated by a threshold NDVI value of 0.55, following which the low-NDVI group and the high-NDVI group were assigned to shrub and tree respectively. The low-FDI group was separated by a threshold NDVI value of 0.5, and then the low-NDVI group and high-NDVI group were assigned to emergent and willow respectively.

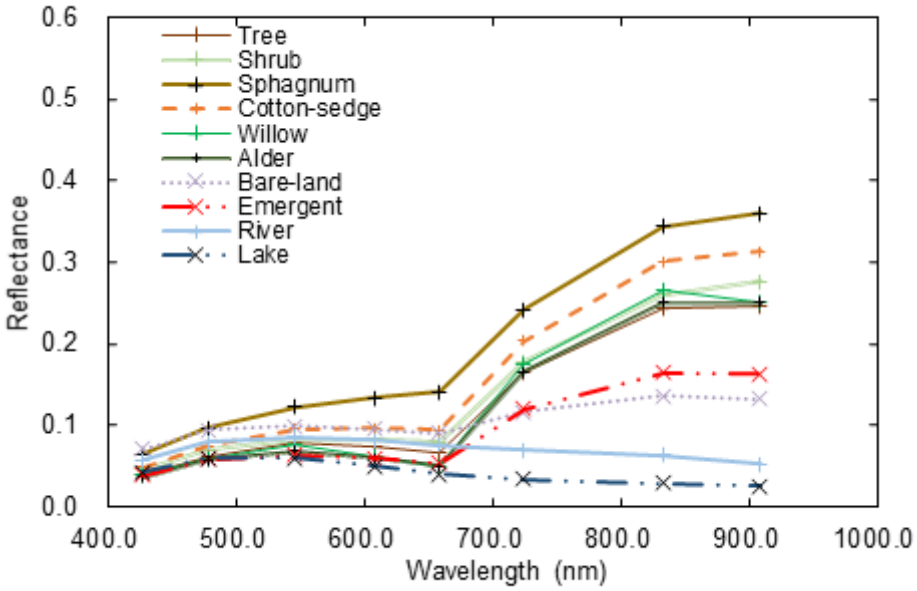

Figure 2-S4. Spectral reflectance of vegetation classes selected by training pixels' average of satellite image. Surface reflectance was demonstrated by a factor between 0 and 1 with no unit.

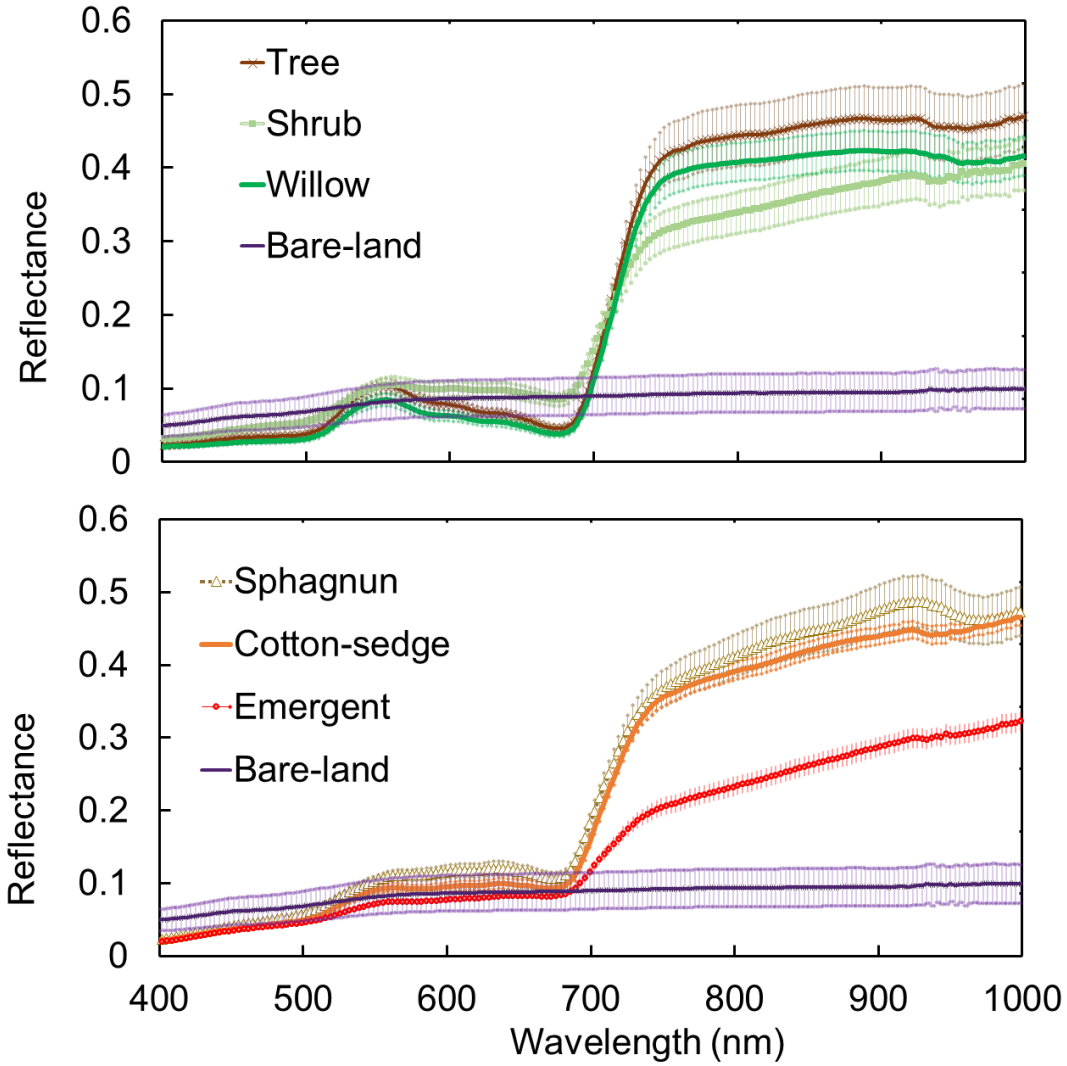

Figure 2-S5. Vegetation and dry sandy soil reflectance spectra for visual and near-infrared wavelength using reference data. Surface reflectance was demonstrated by a factor between 0 and 1 with no unit. Each line and shadow present the average and SD of the reflectance. Vegetation reflectance was measured using a MS720 handheld field spectroradiometer and calibrated with a Spectralon white reference board for inbound radiation in the summer of 2014–2015.

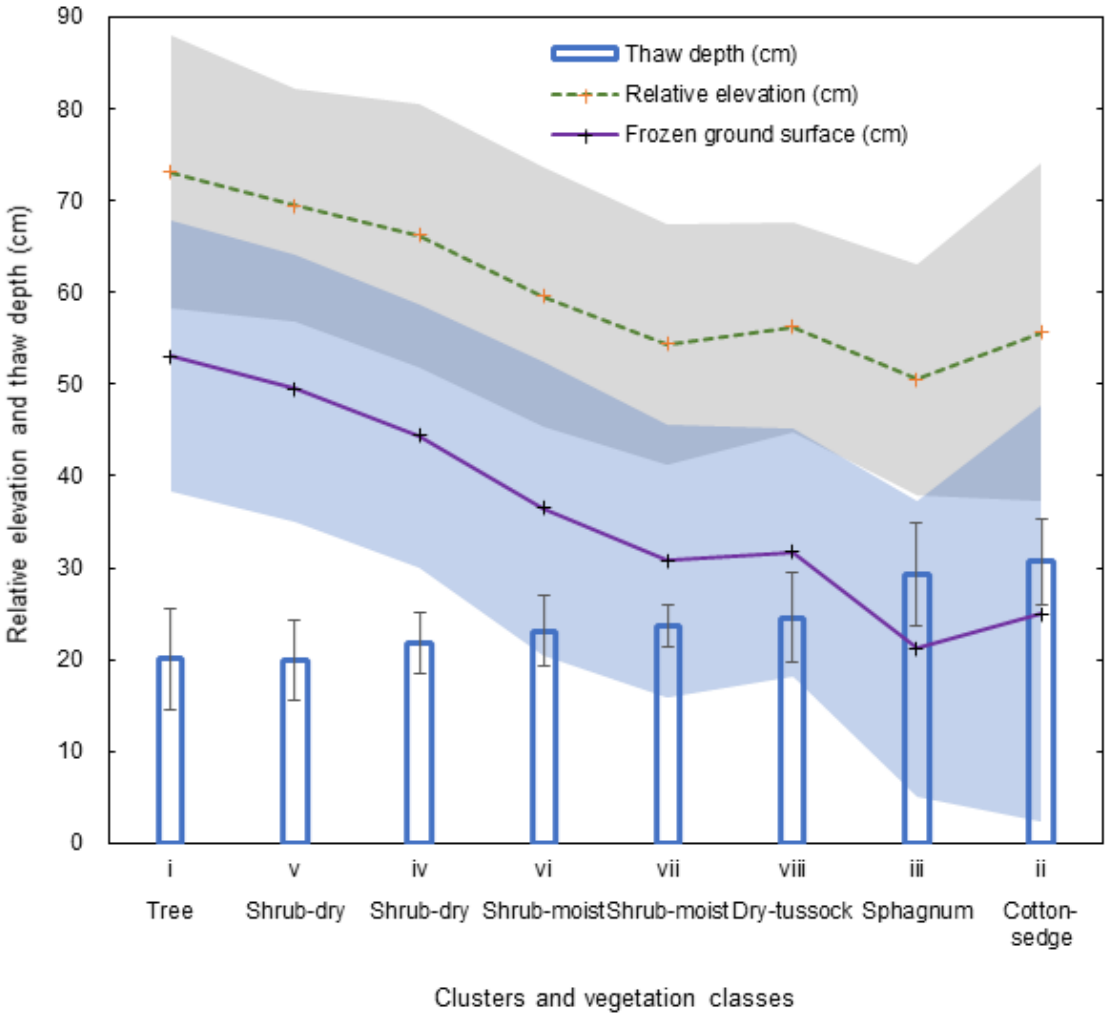

Figure 2-S6. Micro–topographic relative elevation, underground frozen surface elevation and thaw depth at eight clusters (i–viii) from the Kodac site vegetation survey (Table 2-S2). The dashed line shows the average relative elevation of the ground surface (cm), and the hatched area shows the standard deviation of elevation. The solid line shows the average underground frozen surface elevation (cm). Statistical significances were tested among clusters (Table 2-S3).

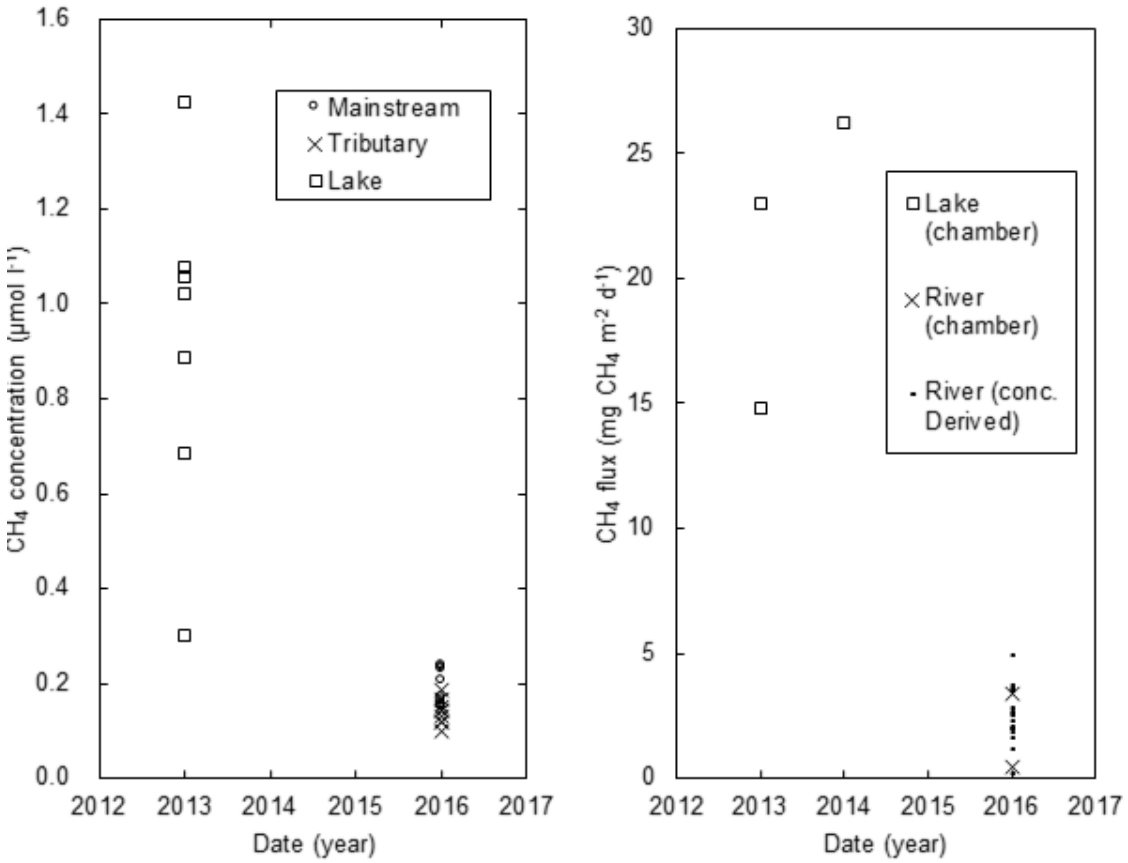

Figure 2-S7. (a) Dissolved CH_4 concentrations in river and lake waters measured using the headspace technique in 2016 and in 2013 respectively. (b) River CH_4 fluxes derived from concentration and transportation velocity equations compared with river and lake CH_4 fluxes derived from chamber measurement. Rectangles, circles and crosses show values for the lake, mainstream, and tributaries of the river. Although we observed almost no emission in the chamber method (0.49–3.36 mg m^{-2} d^{-1}), river water was always oversaturated in dissolve CH_4 with respect to atmospheric CH_4. Therefore, we estimated river methane flux from the river water's dissolved CH_4 concentration, assuming a transfer velocity (2-2-9).

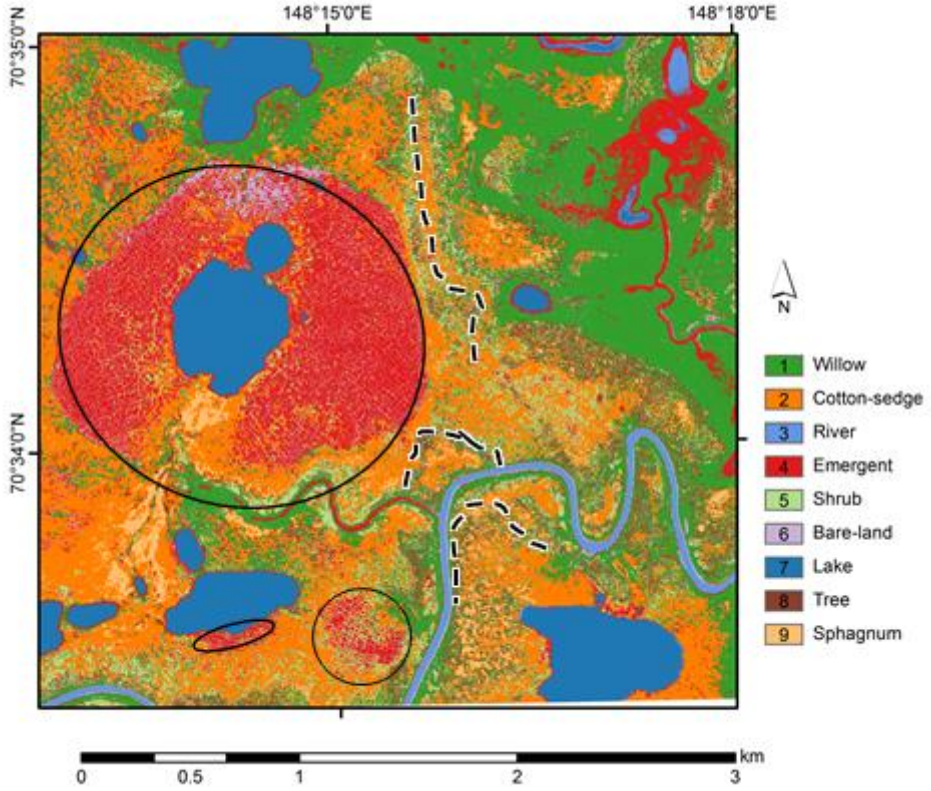

Figure 2-S8. Enlarged view of vegetation map classified into nine classes across 3 × 3 km by the MLC-DTC (maximum-likelihood classification and decision tree classification combined) method. Dashed lines indicate narrow tree-mounds (dark brown). Solid lines indicate mixed vegetation patches dominated by emergent class (red).

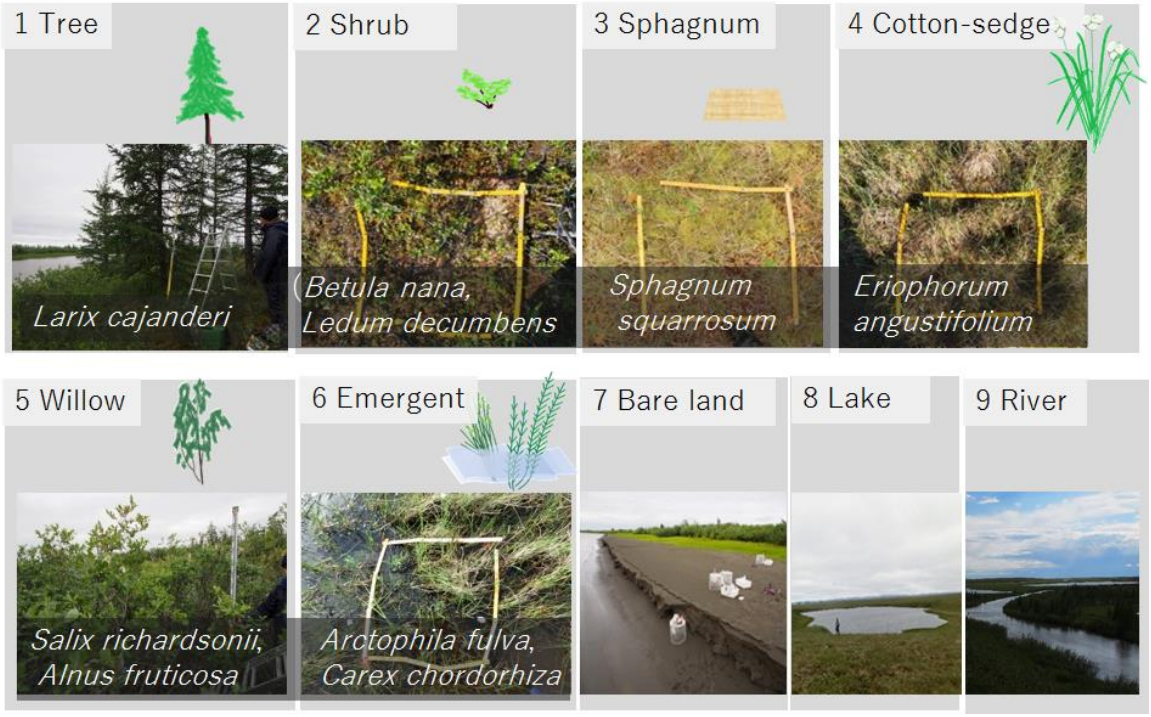

Figure 2-SA. Photographs of nine vegetation classes with typical plant species. A leveling rod indicates 2 m height in tree and willow stands, and a yellow-color ruler frame indicates 0.5 m square block in shrub, *Sphagnum*, cotton-sedge and emergent vegetation cover.

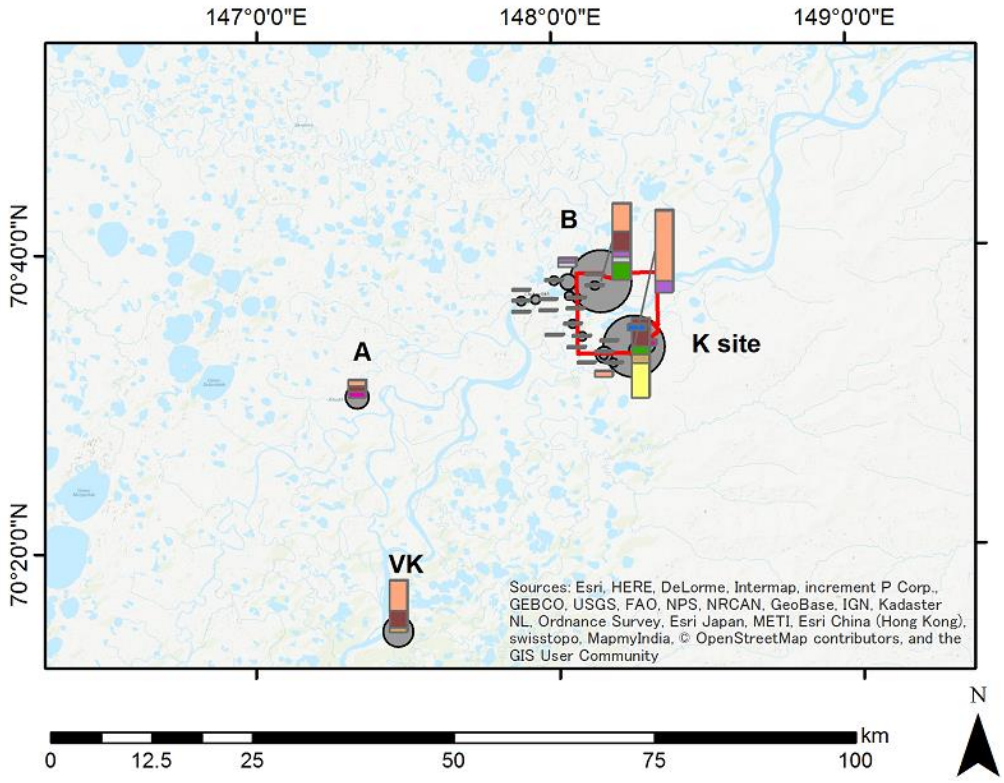

Figure 2-SB. Location of chamber measurements in a local-scale map with bubble (indicating number of samplings) and bar (indicating vegetation classes in each color). Methane flux was observed at 37 locations (212 flux measurements in total), using the chamber method during the growing seasons (July) of 2009 to 2016. The flux measurements were conducted in each vegetation type: i) around site K (70.56 ° N, 148.26 °E), ii) around site B, which was located near the main flow of the Indigirka River (70.64 °N, 148.15 °E), and iii) at additional points in the Indigirka lowland (including the lake, river, and bare-land).

Chapter 3 Estimation of riverine dissolved methane using water surface reflectance remote sensing in extreme flood event

In press; Polar Science, 10.1016/j.polar.2019.01.005.

3-1 Introduction

Dissolved methane (CH_4) is an important factor in aquatic biogeochemical cycles; river water is usually oversaturated with methane, such that the riverine flux contributes to increases in atmospheric methane (Campeau and del Giorgio, 2014; Sawakuchi et al., 2014; Striegl et al., 2012). Additionally, highly saturated dissolved methane is transported to the ocean, where it can be an important methane source in high-latitude coastal areas (Shakhova et al., 2007). Dissolved methane is produced by the decomposition of organic carbon under anoxic conditions and consumed by microbial oxidation, which is activated when the oxygen concentration of river water increases (Stanley et al., 2016). The riverine production/consumption balance is controlled by landscape patterns of river channels connected to streams, lakes, wetlands and ponds that are related to basal sediment compositions (Crawford et al., 2017).

Dissolved methane concentrations can have large spatial and temporal variations including the seasonal dynamics observed in rivers and other terrestrial water bodies. In low-latitude regions such as the Amazon River Basin, the dissolved methane concentration has been reported to rise during periods of low or declining water levels, especially in tributaries (Barbosa et al., 2016). In high-latitude regions, dissolved methane can be enriched owing to seasonal accumulations of methane under lake ice (Langer et al., 2015), contributing to high methane emissions when the ice breaks up in spring (Karlsson et al., 2013). In snowmelt period, river water may also be affected by overflow of accumulated methane in lake water. Changing concentrations of dissolved methane have also been observed in a Finnish river during snowmelt (Dyson et al., 2011). Therefore, in high-latitude regions, seasonal changes in water tables and river discharges can affect dissolved riverine methane concentrations and fluxes.

Such dissolved methane fluxes can be studied using satellite remote sensing to

provide a broader spatial coverage of the inundation area (Rokni et al., 2014) and to determine water color from turbidity using optical reflectance from suspended sediment on the surface (Mertes et al., 1993, Volpe et al., 2011, Ward et al., 2013). Xiao et al. (2017) introduced an empirical stepwise regression for methane flux determination in shallow lakes using observed water clarity, dissolved oxygen data, and the satellite-derived normalized difference vegetation index (NDVI).

In early summer (June–July) 2017, major flooding in the Yana-Indigirka lowland of northeastern Siberia covered a large region with water. Surface water derived from snow and/or ice melt (including lake water) was likely mixed with river water during the flood. We hypothesized that different water sources with distinct levels of dissolved methane and suspended sediments (represented by water color) were mixed during this event, and that their spatial distributions could be distinguished under flood conditions in the main channel and tributaries.

Thus, we collected in-situ concentrations of riverine dissolved methane and surface reflectance satellite data during the summers of 2016 and 2017. Using the 2017 data during the flood period, we also modeled the dissolved methane concentration using water reflectance and estimated the river's methane flux for both years. Our results demonstrate a new approach to estimating dissolved methane using water color reflectance data and offer new insights into methane emissions during an extreme flooding event in northeastern Siberia.

3-2 Methods and Data

3-2-1 Study location and observation methods

We focused on the lower reaches of the Indigirka River and its tributaries near Chokurdakh in northeastern Siberia (Figure 3-1). The landscape consisted of a taiga-tundra boundary ecosystem with many lakes, ponds, and wetlands among shrubland and sparse stands of larch trees. The area's climate is extremely cold with a mean annual air temperature of −13.9°C (measured during 1950–2008; Liang et al., 2014; Yabuki et al., 2011). Water level was recorded every 1–3 days from mid-July to early August during 2015–2017 at two sites, Chokurdakh (70.62° N, 147.89° E) and

Kodac (70.56° N, 148.15° E); these sites were also used by previous studies (Iwanhana et al., 2014; Liang et al., 2014; Figure 3-1b). We recorded river levels directly by measuring the vertical distance from a tagged tree to the river surface, because there are no river gauging stations close to the field site. In addition, we observed river flooding indirectly using time-lapse cameras (Garden Watch Cam, Brinno, USA) and using satellite imagery (see section 3-2-3).

3-2-2 In situ dissolved methane measurements

We collected river surface water samples (upper 10 cm) from a motorboat on 8 and 25 July 2016 (6 samples for each) and 28 July and 2 August 2017 (5 samples for each) using a 60-ml plastic syringe with a three-way stopcock. Samples of river surface water were obtained from three areas of the Indigirka river system: the main channel, substream (west area) and tributaries (east narrow channels in the eastern area; Figure 3-1b). Methane free headspace gas and river water samples was mixed in the plastic syringe for 1 minute. After a leave for 5 minutes , methane was extracted to the head space gas under equilibrium at room temperature and pressure. Ultra-high purity N_2 gas was used as the headspace gas (45 ml of water and 15 ml of N_2 in a 1:3 ratio) and headspace gas was transferred into a 10-ml vacuumed glass vial with a butyl rubber stopper and was brought to the laboratory at Hokkaido University, Japan. Methane concentration in the sample gas was measured using gas chromatography with a flame-ionization detector (GC-FID; HP6890, Hewlett Packard, USA). The detection limit in the gas chromatography (GC) analysis was less than 0.07 μM and the reproducibility of the analysis was less than 0.16 ppm. Finally, the initial concentration of dissolved methane was calculated with a Bunsen coefficient obtained by Yamamoto, (1976). Concentrations in μmol l^{-1} were recorded in units of μM (micro molar). We also used data for dissolved methane concentrations from 13 samples taken at three points within a lake near a tributary (Figure 3-1b) on the 20, 25, and 27 July 2013 (non-flood), using similar methods (Shingubara et al., 2016). Additionally, four ambient air samples were collected at wetlands near the Indigirka's main channel on 10, 19, 20, 24 and 27 July 2016 and 30 July 2017, for use in flux calculations (section 3-2-5). The measured values were

statistically analyzed by t-test using p value notation.

3-2-3 Flooding and water color detection using satellite imagery

We acquired Landsat8 Operational Land Imager (OLI) surface reflectance images (30 m resolution) of the study area for 29 June, 29 July, and 7 August 2016 and 11 and 27 July 2017 (USGS/NASA; Figure 3-2, Table 3-1) and observed the water color. The 11 July 2017 image (Figure 3-1d) was used for detection of flooded areas and for water color analysis when the water was at its highest; the 27 July 2017 image (Figure 3-1e) represented a ~60% retreat of floodwater compared with the peak flood height on 11 July.

Satellite image analysis and classification were conducted using the ENVI v5.1 software (Exilis Visual Information Solutions, Broomfield, CO USA), and spatial patterns were analyzed with ArcGIS v10.2 (Environmental Systems Research Institute, Redlands, CA USA). Water extent (and thus flooding) was defined by normalized difference water index (NDWI; McFeeters, 1996) values exceeding a threshold of 0.05 value; NDWI is defined as:

$$NDWI = (Green - NIR) / (Green + NIR), \quad (1)$$

where Green is Band 3 (533–590 nm) and NIR is Band 5 (851–879 nm). Water surface reflectance (water color) data were acquired using the nearest 4 pixels, including at the sampling sites for dissolved methane (within 1–5 days before sampling). Pixels were carefully selected from a homogenous water surface to avoid terrestrial pixels, shadow, breaking wave bubbles, glint, and other water color variations. Several indicators of water color were used, including reflectance on bands 1–7, NDWI, and the normalized difference vegetation index (NDVI):

$$NDVI = (NIR - Red) / (NIR + Red), \quad (2)$$

where Red is Band 4 (636–673 nm) and NIR is Band 5.

3-2-4 Empirical modelling of dissolved methane concentrations

To develop an empirical model for dissolved methane concentrations, we used the river surface reflectance as a proxy for the spatial distribution of the mixing processes between methane-rich and methane-poor water during flooding on 11 July 2017 (Figure 3-2). First, we applied multivariate correlation analysis and clustered samples by methane concentration and water color using the R software (R Core Team, 2013). A linear relationship between water color and methane concentration was assumed, and this linearity should be tested under various flooding condition in further research. Then, four groups among various methane concentrations (high-low) and water colors (clear-turbid) were distinguished as endmembers.

We used endmembers and a mixing model in a similar manner as to many other studies of stream water solute chemistry (e.g., James and Roulet, 2006; Neal et al., 2010). Our empirical mixing model was defined assuming main channel water (turbid) and tributary water (not turbid) as the endmembers:

$$\rho_{sample} = \rho_m \times F_m + \rho_t \times F_t, \quad (3)$$

$$C_{sample} = C_m \times F_m + C_t \times F_t, \text{ and} \quad (4)$$

$$F_m + F_t = 1, \quad (5)$$

where ρ_{sample}, ρ_m, and ρ_t are the reflectance of sampling points and endmembers in the main channel and tributary, respectively; F_m and F_t are the fractions of the main channel and tributary; and C_{sample}, C_m, and C_t are the dissolved methane concentrations of the sampling points, main channel, and tributary, respectively. The reflectance values were calculated in a scale factor of 0 to 10. The regression for reflectance and dissolved methane was given as:

$$C_{sample} = \text{slope} \times (\rho_{sample}) + \text{intercept}. \quad (6)$$

After obtaining predicted values for slope and intercept, we validated model performance using a subset of the observation data with intermediate reflectance and dissolved methane by clustering with the multivariate correlation analysis as described above. Correlation coefficient, root mean square error (RMSE), and Akaike Information

Criteria (AIC) for the model were also used for evaluating the accuracy of the model (Akaike, 1974).

3-2-5 Estimation of river flux

The methane flux (mg CH_4 m^{-2} d^{-1}) between the river surface and the atmosphere was calculated with a gas transfer velocity (k_{CH4}) using the difference between predicted concentrations in the river (C_w) and observed concentration in the atmosphere (C_a) in 2017 (Figure 3-2):

$$\text{Flux} = (C_w - C_a) \times k_{CH4} \text{ (mg } CH_4 \text{ } m^{-2} \text{ } d^{-1}). \quad (7)$$

Parameterization for the transfer velocity of methane was assumed by analogy to riverine CO_2 gas in boreal arctic zones as reported by Aufdenkampe et al. (2011):

$$k_{CH4} = k_{600} (Sc_{CH4}/400) \times 0.69 \text{ (m } d^{-1}), \quad (8)$$

where k_{600} is the CO_2 gas transfer velocity and $ScCH_4$ is the Schmidt number for methane given by a temperature dependence function (Wanninkhof, 1992). The Bunsen coefficient (Yamamoto, 1976) was then applied to estimate the saturation ratio of dissolved methane. The calculated flux values were the same range as the flux directly observed using a floating chamber at the site (0.5-3.4 mg m^{-2} d^{-1}; Morozumi et al., 2017).

3-2-6 Land cover analysis

We conducted land cover classification using Landsat multispectral data (bands 1–7) from 7 August 2016 (Table 3-1, Figure 3-2). Multiband images were classified by ISODATA unsupervised classification (Tou and Gonzalez 1974, impremented in ENVI software), then mapped using vegetation types drawn from the high-resolution vegetation map produced using the supervised maximum likelihood method (Morozumi et al. 2016), which contains 8 types of vegetation classes, including tree, shrub, willow, and cotton-sedge. The land cover data obtained were used to consider methane sources because dissolved methane can be highly saturated in near-surface soil water in wetlands (Shingubara et al., 2016). Sedge wetland and aquatic lake margin areas up to 500 m from

the river bank were selected as potential methane sources, and were delineated using the spatial multi-ring buffering tool in ArcGIS using 50 m intervals up to 200 m from the river and 100 m intervals 200–500 m from the river. Coverage proportions of methane source landscapes were then compared between the main channel and the tributaries.

3-3 Results

3-3-1 Dissolved methane concentrations of river water in 2016 and 2017

Large differences were detected in the methane concentrations of the main channel and tributaries between 2016 (normal year) and 2017 (flooding event). Dissolved methane concentrations of tributaries (0.7–1.1 μM) were significantly higher (p<0.005) than those of the main channel (0.2–0.4 μM) at the end of the extreme flooding event on 27 July and 2 Aug 2 2017 (Figure 3-3), while dissolved methane concentrations were low (0.1–0.2 μM) in both the main channel and tributaries on 8 July and 25 July 2016. Additionally, the dissolved methane concentrations of lake water were high (0.3–1.5 μM) in the summer of 2013 (Shingubara et al., 2016).

3-3-2 Water color in flooding area

Using NDWI, extreme flooding water cover was detected across ~10,010 km^2 within a total area of ~59,830 km^2 on 11 July 2017. Physical observations showed that water levels were 2–3 m higher than in previous years. The time-lapse camera at the Kodac site captured flood conditions within forested land along a tributary from 11 June to 25 July, 2017.

Water surface reflectance values for both the main channel and tributaries were higher in 2016 (normal year) than in 2017 (flood year) for bands 3 and 4 (Figure 3-S1). Tributary surface reflectance (mean and SD), which was expressed with a scale from 0 to 10, in 2017 for bands 3 and 4 were 0.137±0.040 and 0.153±0.053, respectively, lower than the main channel (0.287±0.094 and 0.343±0.101, respectively; $p < 0.001$). On the

other hand, there was no statistically significant difference in 2016, although the average surface reflectance for the tributaries was lower than for the main channel.

3-3-3 Empirical end-member model for water color and dissolved methane concentrations

Dissolved methane concentrations were negatively correlated with band 4 (red, R = −0.86) and band 5 (NIR, R = −0.87) reflectance (Figure 3-S2). We produced end-member models using these correlations in 2017. Before establishing the models, clustering analysis was used to determine the possible endmembers and outliers; the latter were removed from the model because of specific reflectances from tributaries close to lake outlets, as discussed in section 3-4-1. The clustering results produced four classes indicating (c1) high concentration and low reflectance, (c2) low concentration and high reflectance, (c3) intermediate, and (c4) high concentration and high NDVI and high NDWI (Figure 3-S2); (c4) was considered an outlier. We also removed (c3) for use as evaluation data, as described in the methods.

Using the (c1) and (c2) data, end-member models with bands 4 and 5 were developed (Figure 3-4a). Methane predicted with the band 4 model was compared with the observed methane concentrations in 2017 (Figure 3-4b; R^2 = 0.94, RMSE = 0.097, AIC = −9.44). Modeled concentrations of dissolved methane were mapped at a regional scale (~250 km; Figure 3-4c) and for local sampling areas (~50 km; Figure 3-4d). The main channel of the Indigirka River showed lower values of predicted methane concentrations, while the tributaries were relatively higher in 2017.

3-3-4 Regional river methane flux

The main channel (320 km^2) and tributaries (164 km^2) had average methane concentrations of 0.36 and 0.68 μM, respectively (Table 3-2), 187 and 351 times higher than water saturation at a temperature of 10 °C. Estimated average flux values were 5.6 and 16.5 mg CH_4 m^{-2} d^{-1} for the main channel and tributaries, respectively. Daily surface methane emissions from the total area of the main channel and tributaries were 1839 kg

CH_4 d^{-1} (40.5% of the total river areas) and 2705 kg CH_4 d^{-1} (59.5%), respectively.

3-3-5 Land cover characterization

Land cover types were visually observed at each sampling point and checked against the classification (Figure 3-5). The distribution patterns of the lake-margin and sedge-wetland classes, considered to be the main sources of methane (Chapter 2, van Huissteden et al., 2005; Shingubara et al., 2016, 2019), were different along the main channel and tributaries within the 500 m zone previously defined (Figure 3-S3). The tributaries were surrounded by sedge-wetland and lake-margin (mostly > 50%), whereas the main channel showed less sedge-wetland and more willow bushes, considered to have very low methane flux and concentrations (van Huissteden et al., 2005; Morozumi et al., 2016), along with a wider river channel. The ratios of sedge-wetland and lake-margin to total land cover were 25%–75% along the tributaries and 15%–40% along the main channel, whereas those of willow were 5%–13% along tributaries and 6%–20% along the main channel (Figure 3-S3).

3-4 Interpretations and Discussions

3-4-1 Spatial variations in dissolved methane and water color

Our estimates of dissolved methane concentrations based on water color were higher in the tributaries than in the main channel in 2017 (Figure 3-4c, 4d) and surface water reflectance was negatively correlated with dissolved methane (Figure 3-4a). The main channel was turbid because of sediment transported from upstream areas with lower dissolved methane, whereas the tributaries were relatively clear with higher dissolved methane. In other words, dissolved methane was mostly sourced from tributaries within the Indigirka River lowlands, instead of upstream areas along the main channel from which most suspended sediments were sourced (Huh et al., 1998). On the other hand, in the summer of 2016, the dissolved methane concentrations in the tributaries were as low as in the main channel. Optical properties of tributaries' water can also be affected by

dissolved organic matter, which is a potential substrate of methane, leaching from wetland soils, and has a dark color with light absorption (i.e., Brezonik et al., 2015), although these characteristics might be masked by the large variations of surface reflectance derived from light scattering by suspended sediments, in particular during 2017.

Dissolved methane concentrations sampled between 2016 and 2017 were similar in the main channel, whereas reflectance was different between the two years. Water color results indicated that turbidity in tributaries and the main channel were higher in 2016 than in 2017 for bands 3, 4, and 5 (Figure 3-S1). The main channel is usually turbid during the spring snowmelt season owing to erosion in mountainous upstream regions, such that this turbid water mixes with clearer water in the lowlands. However, during the extreme flooding event in 2017, this turbid upstream water may have mixed with larger amounts of lowland water, causing the lower turbidity. In addition, a large amount of precipitation, and snowmelt water from thick snow cover in the lowlands, may also have contributed to the lower turbidity in 2017.

As noted in section 3-3-3, there was an outlying sample (c4) that contained a high concentration of dissolved methane (Figure 3-3) and showed relatively higher reflectance values along with high NDVI and NDWI (Figure 3-S2). This sample was collected from a tributary close to the outlet of a lowland lake at a site surrounded by stands of willow and aquatic grasses; thus, there was the potential for aquatic plants to produce high NDVI. Xiao et al. (2017) reported that high NDVI and methane concentrations can be explained by *in-situ* methane production linked to the decomposition of aquatic plants and algae in subtropical lakes. As the sampling point for outlier (c4) in the tributary was close to the lake outlet, dissolved methane from the lake may have been high owing to the decomposition of organic matter.

3-4-2 Potential sources of dissolved methane in tributaries

During the extreme flooding event, there may have been two origins for the excess water: local snow melting under floodwater and water from the main channel. As the dissolved methane in the main channel was low, the source of dissolved methane in the

tributaries must have been produced on the land, when the floodwater receded, and the tributary channels were re-established. There are usually several sources of methane on land, such as wetlands and lakes; during floods, vegetation such as trees and shrubs (which are usually methane sinks) might become sources owing to the anoxic condition of the soil. Any methane produced on the land can be carried away by the tributary. Compared with the 2017 flood, during the summer of 2016 the tributary water was poor in methane, owing to lower methane production and higher methane oxidation on the dry land (i.e., the normal condition).

Another possible reason for the higher methane concentrations in the tributaries might be the land cover. Higher ratios of sedge-wetland and lake-margin (> 50%) were observed close to the tributaries than along the main channel (Figure 3-5), which could have produced more methane (e.g., Billett and Harvey, 2013; Fernandez et al., 2016; Murase et al., 2003), whereas land cover close to the main channel was more commonly willow thickets on sand bars with only limited wetlands. The vegetation types close to the main channel are not typically considered methane sources (van Huissteden et al., 2005), so when flooding occurs, the vegetation along tributaries produces more methane than that along the main channel.

Finally, the relatively large amount of water in the main channel means that the low concentration of dissolved methane in the main channel is not strongly affected by the inflow of tributaries with higher concentrations.

3-4-3 Contributions of riverine methane emissions during extreme flooding on a regional scale

An extreme flooding event influenced an extensive region of river lowlands in eastern Siberia from June to July 2017. We reported that the dissolved methane concentrations along the Indigirka River and its tributaries (0.1–1.1 μM) were slightly higher than those previously reported at Lena river (0.01–0.7 μM), the adjacent catchment to our study location (Bussmann, 2013; Semiletov et al., 2011), and a small tributary of Yenisei in central Siberia (0.01-0.02 μM; Morishita et al., 2014). The large temporal variations of dissolved methane concentration would cause the uncertainty in

the regional estimate. However, the dissolved methane concentrations in this study are not extremely high compared with a middle Lena tributary (0.1-1.9 μM; Sawamoto et al., 2006), Yukon river main stem and tributaries (0.15–0.82 μM; Striegl et al., 2012), and even smaller than for boreal streams in Wisconsin (USA; 0–2.8 μM; Crawford et al., 2017). Comparison suggests that our finding of high dissolved methane concentration is within the range of data on a global scale and does not exceed the spatial-temporal variation of those reported concentrations.

The total river flux estimated using calculation with transfer velocity in 2017 (9.4±3.5 mg CH_4 m^{-2} d^{-1}), of which 60% was sourced from the tributaries, was significantly higher than that in 2016 (2.6±1.1 mg CH_4 m^{-2} d^{-1}); daily emissions of river methane were 3.6 times higher in 2017 than in 2016 (Table 3-2). The large spatial variation of dissolved methane concentration, modeled in 2017, caused substantial differences in the flux estimation. The flux in the main-flow and tributaries in 2017 (flood) were 5.6±1.1 and 16.5±2.8 (mg CH_4 m^{-2} d^{-1}), respectively. In particular, the flux for tributaries in 2017 were higher than in previous research for Lena (0 mg CH_4 m^{-2} d^{-1} owing to measurement limit; Schneider et al., 2009), the Middle Yukon (6.2±2.1 mg CH_4 m^{-2} d^{-1}; Striegl et al., 2012) and the Kuparuk river in Alaska (5.8 mg CH_4 m^{-2} d^{-1}; Kling et al., 1992), but lower than the Lower Yukon (22±4.2 mg CH_4 m^{-2} d^{-1}; Striegl et al., 2012). Enhanced emissions at tributaries, covering 34% of the total river area, were evaluated to be 2.7×10^3 kg CH_4 per day. Previous studies have reported significant methane efflux in the growing season using the chamber method for the back swamp of a river margin (310–890 mg CH_4 m^{-2} d^{-1}), a polygonal sedge wetland (48–190 mg CH_4 m^{-2} d^{-1}) in the Indigirka lowland (van Huissteden el al 2005), and a polygonal wetland in the Lena delta (78–100 mg CH_4 m^{-2} d^{-1}; Sachs et al., 2010). Riverine methane emissions in this study are smaller than those from wetland soils on a daily scale. Nevertheless, riverine emissions and water-to-air transportation of dissolved methane should not be negligible while flood waters cover the land for more than a month, and flux through the wetland soil surface might be inhibited by water on a month-long time-scale. The estimation is also limited by the flux evaluation method applied from the constant transfer velocity, although the flux can be obtained from the difference in partial pressures between air and water of CH_4. Gas exchange rate is expected to be high in the

turbulent conditions of water and atmosphere, in which the transport velocity (k_{CH4} in Eq 7) is high. Therefore, the river CH_4 flux may be linked to the hydrology which may be relating to the stream morphology of the rivers (Campeau et al., 2014), and these parameters are unknown in our study. There could still be underestimation of methane evasion under unusual water surface mixing conditions during flooding, and further research is needed to improve measurement of dissolved concentrations and the air–water surface exchange of methane for reliable estimation during extreme events.

3-5 Concluding remarks

Visible and near-infrared bands, recorded by high-resolution satellites, can be used for modeling the spatial variations of riverine methane concentrations. In this study, the best indicator for dissolved methane was the red band (636–673 nm), which responded to turbidity controlled by suspended sediment concentration enhanced under extreme flooding, and was negatively correlated with dissolved methane concentrations. The methods presented here for satellite observation of dissolved methane can provide a tool for in situ environmental monitoring in remote areas such as Siberia.

Figures and Tables

Table 3-1. Landsat 8 OLI satellite images used in flood detection.

Acquisition Date (dd-mm-yy)	Path/Row[1]	Surface Condition[2]	Solar angle zenith (deg)	Azimuth (deg)[3]
29-6-16	115/10	dry	47.75	175.95
29-7-16	117/10	dry	52.3	175.25
07-8-16	116/10	dry	54.63	175.55
11-7-17	114/10	flood	48.88	175.37
11-7-17	114/11	flood	47.63	173.01
27-7-17	114/10	after flood	51.78	175.18
27-7-17	114/11	after flood	50.54	172.89

[1]Location identifier using the global notation system for Landsat data.

[2]Condition of the land surface (whether flooded or not).

[3]Horizontal angle relative to north from the observer.

Table 3-2. Predicted dissolved methane concentration [CH_4], saturation ratio of dissolved methane in equilibrium, flux as average and SD, total methane emission in the study area per day, and contribution of methane flux from the main channel and tributaries.

Year	Category	Area[*1] (km^2)	CH_4 concentration (μM)[*2]	saturation ratio[*3]	Flux ($mgCH_4$ m^{-2} d^{-1})[*4]	Daily CH_4 emission ($kgCH_4$ d^{-1})	Regional contribution %
2017	All	483.3	0.47±0.17	242	9.4±3.5	4544	
	Main channel	319.5	0.36±0.07	187	5.6±1.1	1839	40.5
	Tributary	163.9	0.68±0.12	351	16.5±2.8	2705	59.5
2016[*5]	All	483.3	0.17±0.04[*5]	86	2.6±1.1	1257[*6]	

[1]Study area covers a 250 × 350 km region in the Indigirka River lowlands.

[2]Dissolved methane concentration predicted by the empirical model.

[3]Saturation ratio of dissolved methane against solubility of dissolved methane in equilibrium.

[4]Average methane flux from water surface to the atmosphere estimated from predicted dissolved methane concentration.

[5]Average dissolved methane in 2016 among the main-channel and tributaries using observed values.

[6]Total methane emission calculated from observed mean flux in 2016 multiplied by total river area.

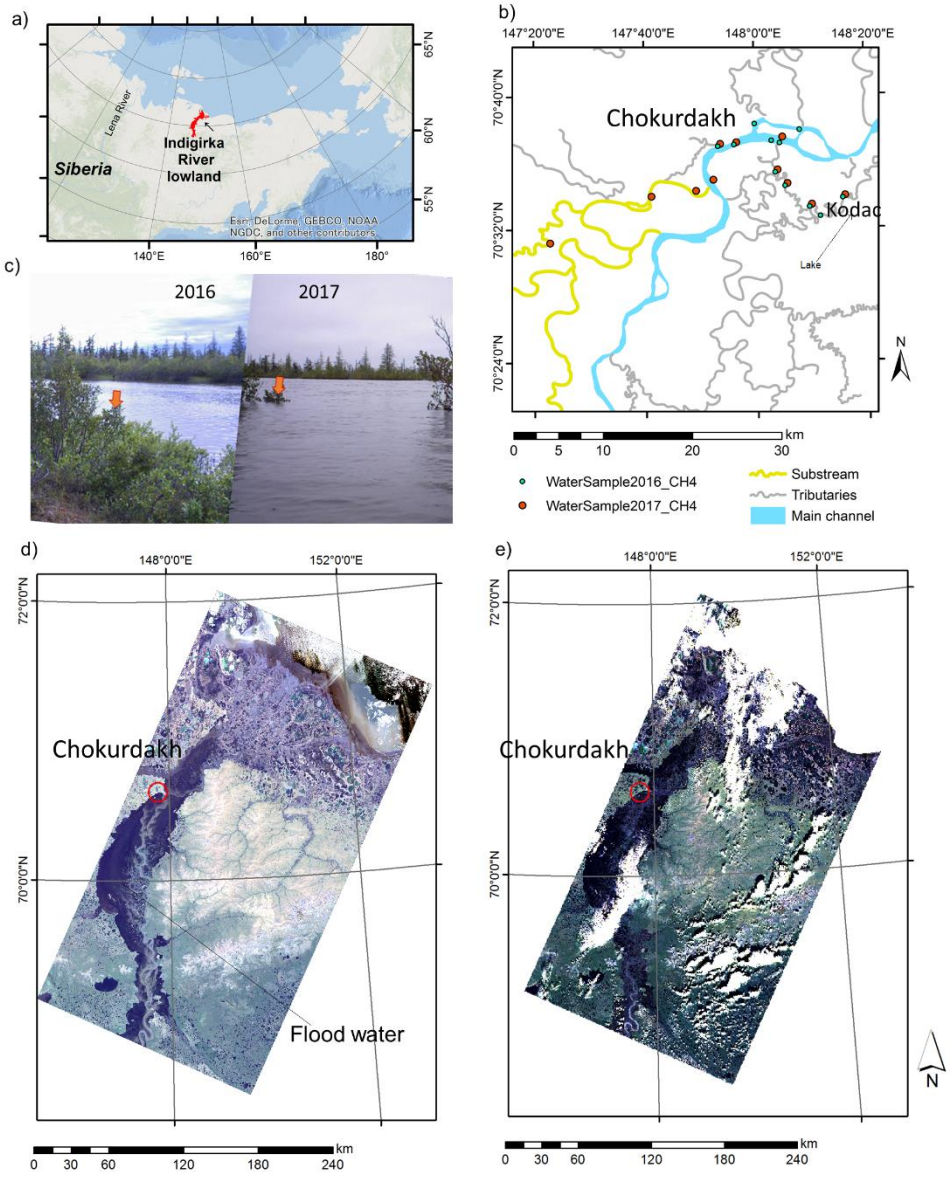

Figure 3-1. Study sites and sampling locations for a typical year in 2016 and an extreme flooding event in 2017: (a) Observation area in the region; (b) Sampling sites for dissolved methane near Chokurdakh and Kodac; (c) Photographs recorded along a tributary near Kodac during the summers of 2016 and 2017; (d) Landsat 8 true color image during the peak of flooding on 11 July 2017; (e) Landsat 8 true color image during flood decline on 27 July 2017 (6.0×10^4 km^2). Red circle indicates location of the town of Chokurdakh. White blank on the image is a cloudy area (1.3×10^4 km^2) that was excluded from the analysis.

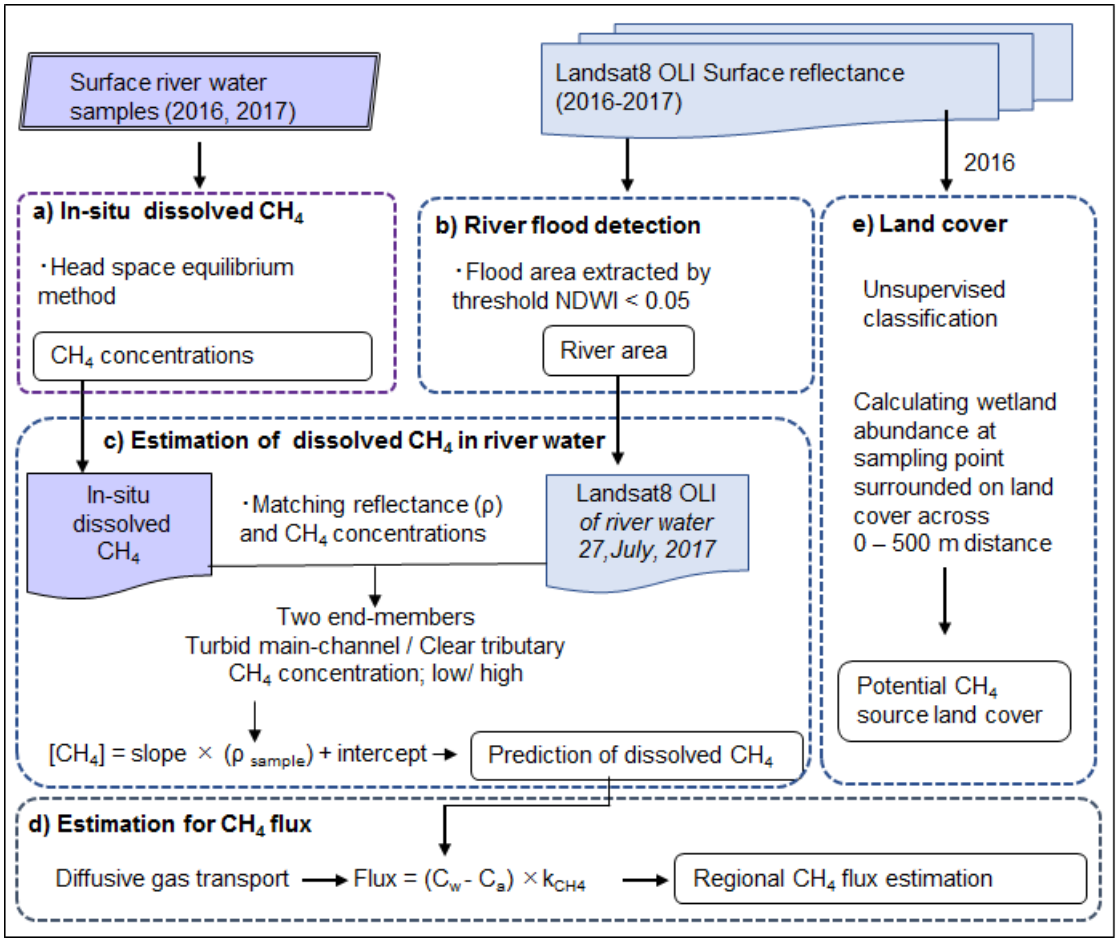

Figure 3-2. Flow chart for data processing. (a) In-situ dissolved methane in river water; (b) river flooding detection with Landsat 8 on 11 and 27 July 2017; (c) modeling for dissolved methane with in-situ methane concentrations and reflectance; (d) regional methane emissions calculated using a diffusive transport model; (e) land cover identified using unsupervised classification to detect potential methane sources. Abbreviations note reflectance on Landsat8 (ρ), concentration of dissolved methane ([CH_4]), and slope and aspect of regression to predict dissolved methane. Abbreviations for flux calculation are concentration of methane in water (C_w)and air (C_a), and the gas transfer velocity of methane between water and air (k_{CH4}).

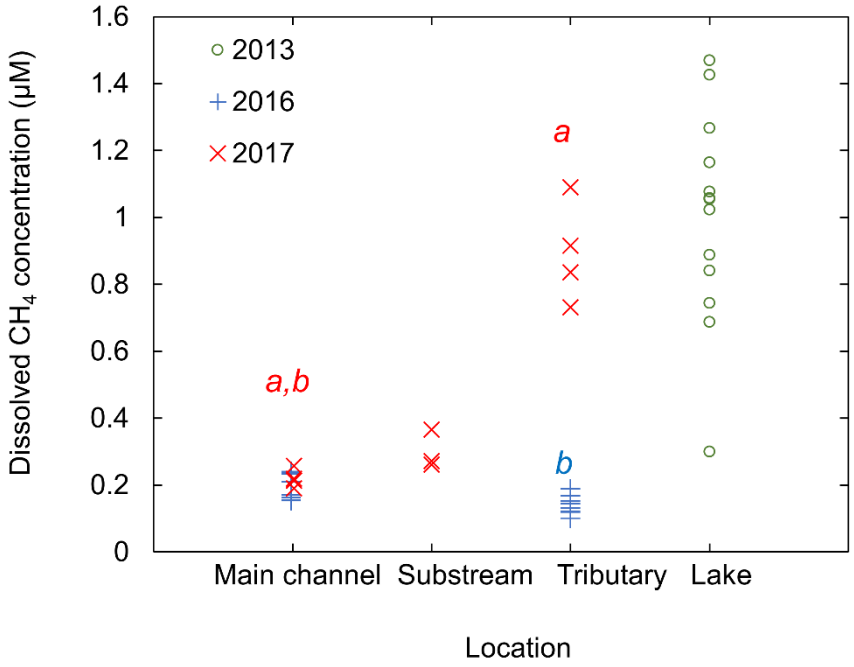

Figure 3-3. Dissolved methane concentrations (µM) in the main channel, substream, tributaries, and lake observed in July 2013, 2016, and 2017. Significant differences between the main channel and tributary in 2017 are marked as *a* ($P < 0.005$), and in 2016 with as *b* ($P < 0.005$).

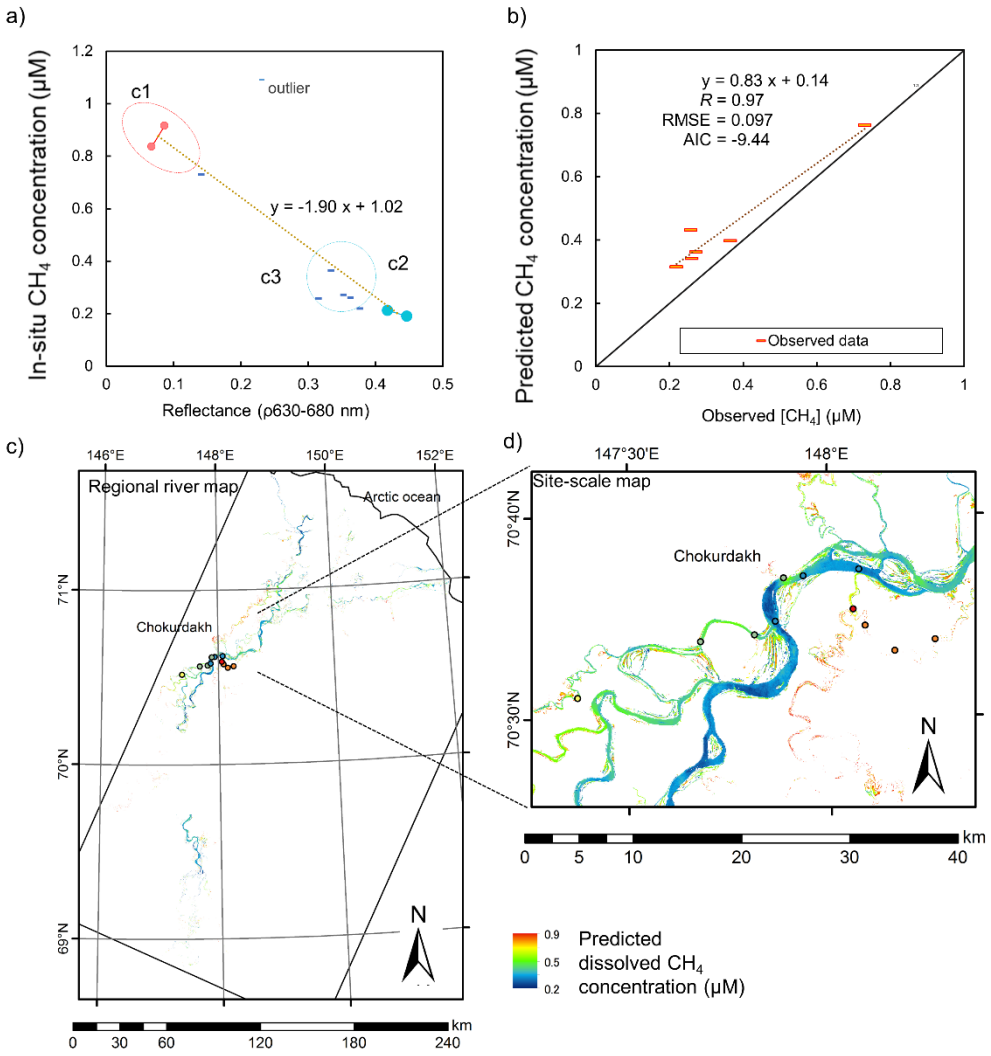

Figure 3-4. Empirical endmember mixing model for dissolved methane concentrations (μM) and satellite reflectance from the red band (630–680 nm). Surface reflectance values were expressed in a scale of 0-10 ($\times 10^{-1}$). (a) Relationship between reflectance from the red band (636–673 nm) and in-situ dissolved methane, with notations for endmembers of higher concentration with low reflectance (c1), lower concentrations with high reflectance (c2), and intermediate (c3); (b) In-situ dissolved methane and predicted methane concentration with an empirical endmember mixing model from satellite reflectance from the red band (636–673 nm) with the 1:1 line, correlation coefficient (*R*), root mean square error (RMSE), and Akaike information criteria (AIC); (c) Distribution map of river dissolved methane concentrations drawn by an empirical endmember mixing model with satellite reflectance from the red band (636–673 nm) in the lower Indigirka River region. (d) Enlarged view around the sampling area; cloud, lake, and land areas were excluded from the analysis.

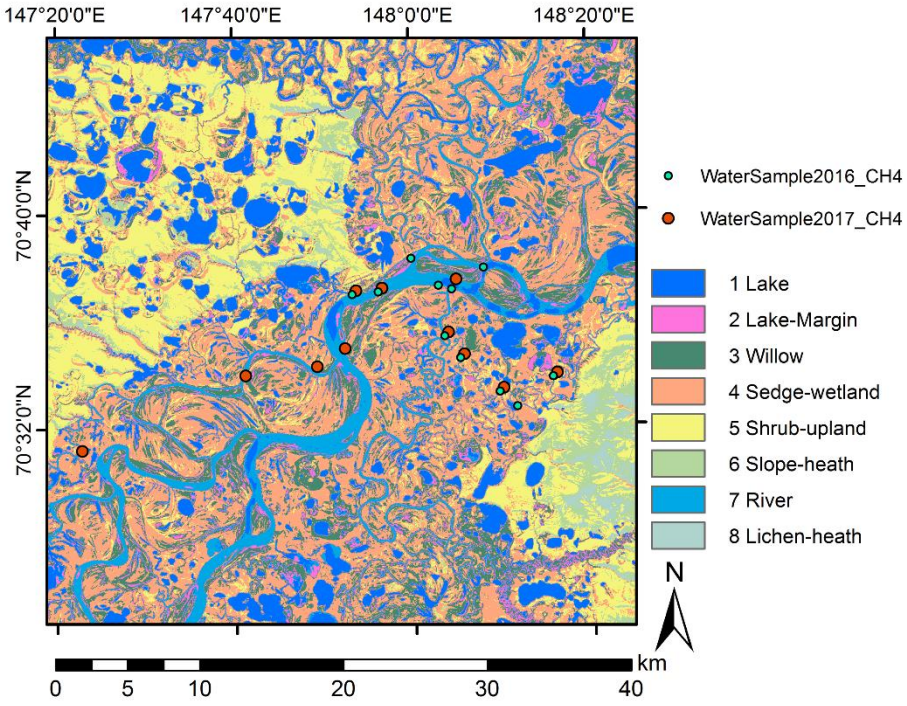

Figure 3-5. Land cover properties classified from a Landsat 8 image on 7 August 2016.

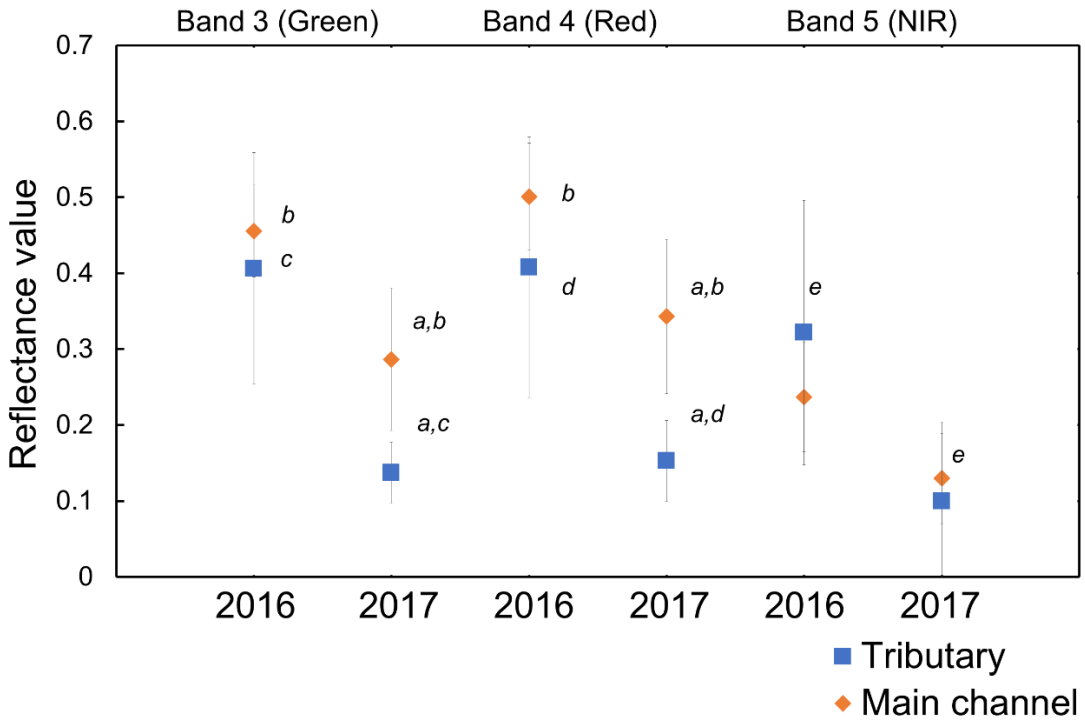

Figure 3-S1. Surface reflectance of the tributary and main channel in June-August 2016 (non-flood) and 2017 (extreme flood), shown as average ±SD; with a scale factor of 0-10 ($\times 10^{-1}$). Reflectance values were collected in the water sampling site at four points in tributary and seven points along the main-flow; for each, Band 3, Band 4, and Band 5 reflectance was compared. Significant differences between tributary and main-flow in 2017 is shown with *a* ($P < 0.001$). Differences between 2016 and 2017 for the main-flow are shown with *b* ($P < 0.001$), and difference between 2016 and 2017 for the tributaries is shown with *c* ($P < 0.001$), *d* ($P < 0.005$) and e ($P < 0.01$).

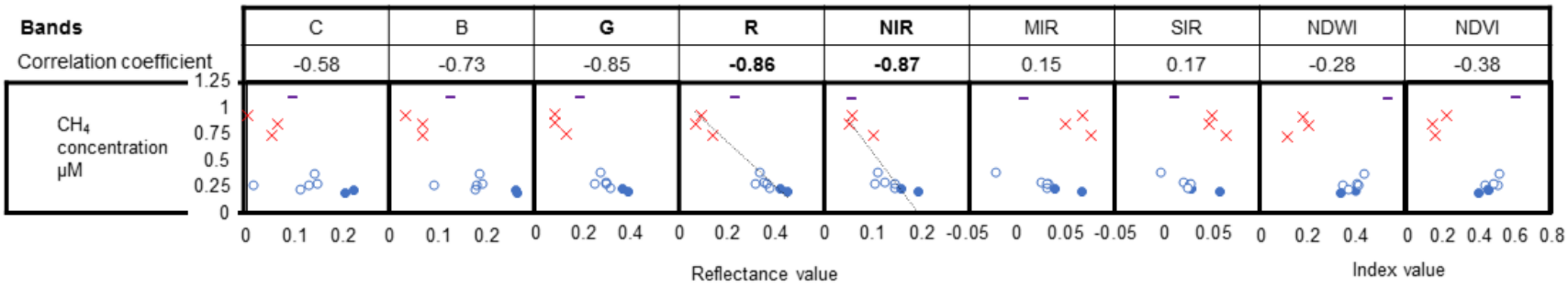

Figure 3-S2. Multivariate correlation analysis on satellite surface reflectance (coastal, blue, green red near-infrared shortwave-infrared1, shortwave-infrared2 band; with a scale factor of 0-10) and water indices against dissolved CH_4 concentration. Each legend indicates the different clusters of red x-marks (c1), blue filled circles (c2), blue blank circles (c3), and purple bars (c4-outlier).

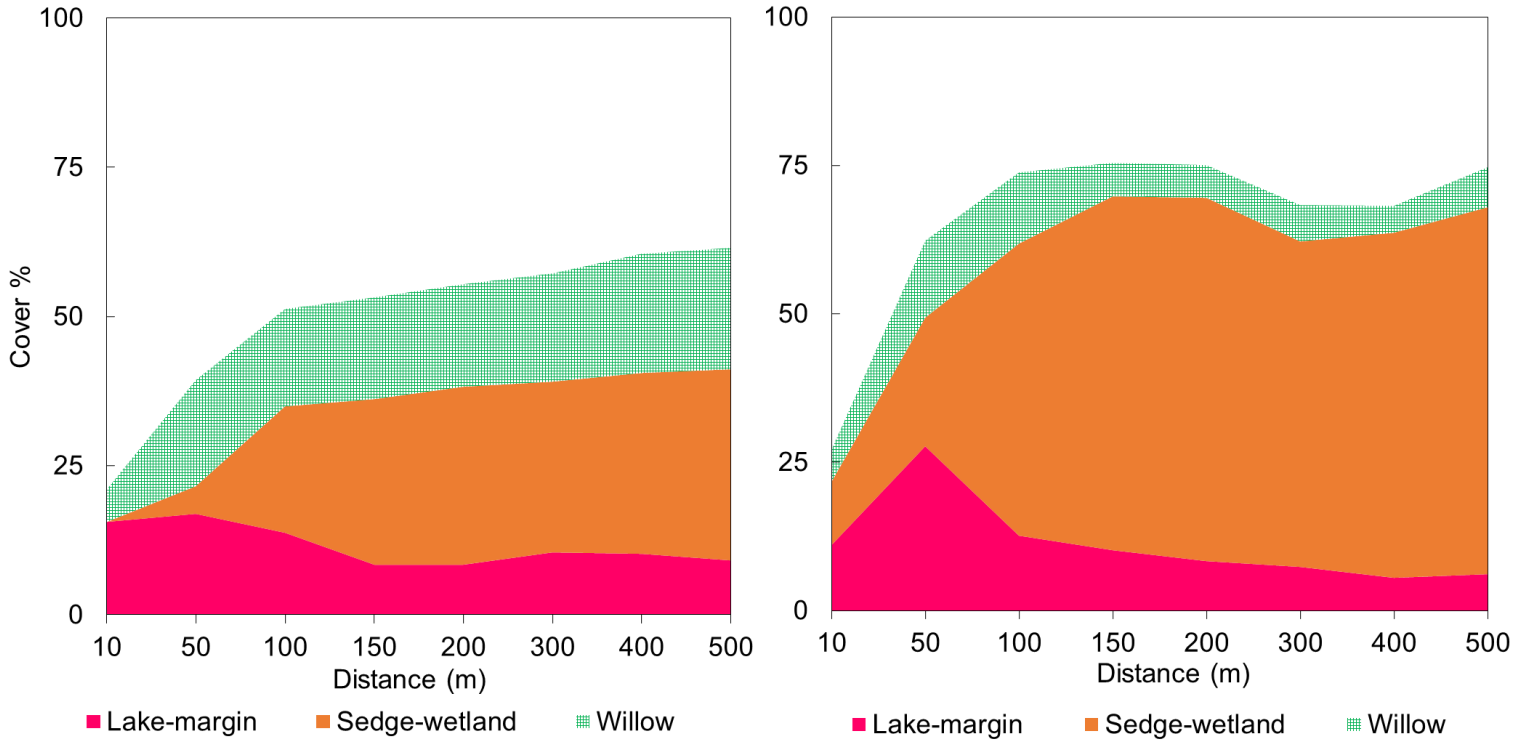

Figure 3-S3. Land cover properties of surrounding areas (0–500m distances from each sampling point). Tributary sampling points (right) were adjacent to the lake-margin and sedge-wetland, implying potential CH_4 sources, whereas the main-flow (left) was adjacent to willow bush, implying no-source.

Chapter 4 General discussions

4-1 Implication of regional estimation for future perspectives

4-1-1 Toward the regional study in northeastern Siberia

The study has provided an approach for regional assessment based on local sampling of ecosystem and biogeochemical cycles. Indigirka lowland, the study area, is only a part of the region in northeastern Siberia. However, there were different characteristics between taiga-tundra boundary and typical tundra or boreal forest. For instance, there are different CH_4 emission values, different plant species and vegetation, and discontinuous patchy larch forest. It suggested that boundary ecosystem does not resemble neither tundra ecosystem nor taiga ecosystem, and some of those characteristics might be missing in regional evaluations. This study also figured out the no CH_4 sources (tree, shrub and willows) on microtopography in wetlands. Those could be error on the regional evaluation, though contribution of non-source classes were small (Chapter 2). The multiscale approach from site to local scale can provide regional evaluation precisely contributed by microtopographic features.

For further scaling, the fundamental key is the integration of small classification components toward the local and regional scales. Small vegetation patches cannot be detected in regional or global data, because larger extent data tend to be coarser spatial resolution. One possible solution is to make subclasses into an integrated category, in which the cover ratios of subclasses were assigned by constant value observed in a local representative site. Another possibility is a subpixel classification method, which could evaluate cover ratios in a pixel using endmember model for representative spectral data in each category, thus it is preferable for various landscape conditions in regional scale. Indeed, we have further studied about subpixel classification for approximately 70 km × 70 km region in Indigirka lowland and successfully evaluated vegetation coverage in relatively middle resolution (ALOS AVNIR2: 10 m) satellite images compared to WorldView-2 high resolution data (0.5 m) (Morozumi et al., 2017, 2018, in conference).

4-1-2 Comparing the results of the local methane emission with a global methane model

The study provided the estimation of local-regional CH_4 emissions using in situ observed data with interactive up-scaling based on vegetation mapping. The challenges of this subject in Siberian arctic are still not so many, thus it is expected to be further application for global scale studies.

In this section, I compared our average CH_4 emissions in local scale (10 km × 10 km) to an output of a process-based global biogeochemical model, Vegetation Integrated Simulator for Trace gases (VISIT; Ito and Inatomi, 2012), to discuss the implication of our data in modeling validations and global biogeochemical cycles. In the VISIT model, fluxes were calculated by schemes of single layer soil (Cao, 1996) and multilayer soil with multiple transportation pathways (Walter and Heimann, 2000), and fluxes were weighted by wetland coverage referred to the Global Lake Wetland Database level 3 product (Lehnar and Döll, 2004) which has spatial resolution of approximately 900m × 300m (Figure 4-1, 4-2). Simulated fluxes were calculated at a spatial resolution of 0.5°×0.5° which was comparable to approximately 50 km × 15 km spatial resolution. Model were calculated from 1990 to 2017, and average value and annual fluctuation were different among models (Figure 4-3).

In the comparison between vegetation map (this study) and GLWD, large part of cotton-sedge, emergent and willow around lakes (this study) were accounted for coastal wetland in GLWD. Willow around river was accounted for freshwater marsh and floodplain (Figure 4-2). The wetland fraction was accounted for 81.5% in GLWD whereas a fraction showed 34.1% of our vegetation map.

There was overestimation in Walter-Heimann's (WH) methods in GLWD weighted result, which were explained as larger fraction of wetland in GLWD dataset (Figure 4-4). Indeed, model recalculation weighted by our vegetation map were less than half of calculation weighted by GLWD. On the other hand, Cao's result were similar or lower values compared to our result. It is difficult to tell the reasonable or trustful value of different datasets for far different purposes, although those comparisons showed that

model output ranged 6.2-0.4 times than our local up-scaling, and overestimation of wetland coverage in the heterogenous landscape in a taiga-tundra boundary. It suggests that high resolution vegetation map could provide useful information of wetland coverage in heterogenous landscape and furthermore we could point out the willow covered floodplain is no CH_4 source and it could be missed those non-source landcover in previous wetland datasets.

Despite our estimation includes *in-situ* fluxes in July and detailed spatial covers of CH_4 sources, we could not have discussed temporal dynamics of emissions in the thesis. The reason is that manual chamber method in our study was not suited for long term continuous measurement but suited for observation in many plots with not many temporal repetitions. Our observation was conducted on the warmest month (July), to show the mean flux of the peak growing season among eight years (2009-2016). The VISIT result showed that representative ratio of July emissionis to annual emissions were 25±8% and 41±12% (average and SD) for WH's and Cao's estimations, and it suggest that our estimation would represent approximately 1/3 to 1/2 of annual emissions. We concluded that the spatial differences in flux related to vegetation were successfully represented large proportion of annual emissions in the study region. However, there were limitations of our findings due to the large inter-annual variation of fluxes in wetland (Chapter 2) perhaps depending on the precipitation and soil moisture as comparably reported in the arctic (Mastepanov et al., 2013, Shigubara et al., 2019). The VISIT model result also showed large interannual variation (Figure 4-3), where coefficient of variations was ranged 0.67-0.34 for different methods and areas in 2009-2016. Those insights suggest that our average estimation would be biased by measurements in each year, though it is difficult to delineate contribution of annual difference from variations due to the limited repetition for temporal differences. Therefore, it is necessary to monitor the temporal variations combined with measurement of spatial variations in CH_4 emissions for further reliable estimations in the region.

4-1-3 Implications of local observations to assess biogeochemical cycles in

changing biome and climate

The aim of the study is to clarify the local CH_4 emissions and the role of taiga-tundra boundary ecosystem among regional CH_4 budget in high latitude. In chapter 1, we set four scientific questions: i) What is the environmental factors controlling vegetation distribution? ii) What is the spatial limiting factor for local CH_4 emissions? Whether hypothesized CH_4 absorption in forest floor could affect local CH4 emissions? iv) Are there any effect on CH_4 emissions by flooding event? We now summarize the findings and consider implications of the study.

The vegetation distributions were observed from point scale to local scale combining field survey and satellite remote sensing. The result showed that vegetation distributions, defined by different plant species appearance, were controlled by microtopographic difference corresponding to permafrost thaw depth, soil moisture and frost height in site scale (Figure 2-4, 2-7), and tree mound, where larch tree could grow up, has only limited extents among local area (Figure 2-11). The local CH_4 emissions were largely contributed by cotton-sedge wetland (Table 2-3). In contrast, ground of tree mound was not significant sink, andrarely contributed to balance local CH_4 emissions. The limited CH_4 sinks in the study area also imply that taiga-tundra boundary lowland, where tree growth was regulated by microtopography on permafrost, cannot act as a negative effect on CH_4 emissions among regions. Indeed, local CH_4 emissions in the study was rather higher than previous reported values in tundra in NE Siberia (Sachs et al., 2010, Schneider et al., 2009). Those findings could approach the aim of the study, but it remains unclear whether the CH_4 emissions and the area of vegetation, treeline and waterbody could change in near future. There will be still missing factors of tree distributions and forest CH_4 absorptions. Therefore, especially to answer the third question, whether hypothesized forest absorption could affect local CH_4 emissions, we need further investigations of landscape dynamics, vegetation successions, permafrost thaw, local climate and temporal CH_4 dynamics in shifting ecosystems and biomes under climate change.

The field observation could provide a new finding such as a different riverine dissolved CH_4 concentrations and CH_4 fluxes between extreme flooding in 2017 and

normal year in 2016. The local estimation further implied that flooding transport could affect local redistribution of dissolved CH_4 concentrations and CH_4 effluxes in short periods. However, much work still remains to understand the correlation between dissolved CH_4 and apparent turbidity in river water. Detailed studies should be made on transportation and balance of dissolved CH_4 under flooding in lake dominated landscapes to clarify the regional impact of extreme flooding on CH_4 budget.

High latitude regions are thought to be suffering gradual biome shift and event induced disturbances, and those two aspects should be monitored not only in site but also in local scale. It was suggested that point scale observation (0.5 m for vegetation and 0.35m for CH_4 flux chamber) may missing representative feature of landscape structure in 10×10 km local scale (Chapter 2), and those findings imply the benefits of multiscale analysis on high latitudes ecosystem. Flooding disturbance (Chapter 3) also may affect vegetation on the land via late blooming, damaged buds and leaves, over wetting stresses and so on. Furthermore, the disturbed ground may affect permafrost thaw and may trigger thermokarst processes, which can drastically change the landscape. In decadal timescales, it is necessary to monitor in site and local-regional scales whether forest northward or forest decline, and wetland increase or decrease at taiga-tundra boundary as a frontline of biome shift.

4-2 Concluding remarks

4-2-1 Local-scale vegetation mapping and methane emissions in taiga-tundra boundary lowland

The heterogenous vegetation distribution and coverages were provided by a microtopographic level vegetation map using high resolution satellite imagery and field survey for 10×10km local CH_4 upscaling. The taiga–tundra boundary ecosystem of the Indigirka River lowland has a large coverage of wetlands (28% by cotton-sedge and 10% by emergent), leading to larger local CH_4 emissions (37 ± 10 mg m^{-2} d^{-1}) than that in the tundra located in northeastern Siberia. Results from site- and local-scale vegetation mapping, validated by field survey of apparent plant species, indicated that site-scale hydrological conditions and geomorphological structures with rivers and permafrost could explain vegetation distribution patterns. Highly heterogenous vegetation and

spatially varied CH_4 flux makes high-resolution satellite images essential for assessing local CH_4 emissions. Our findings indicate that tree distribution was spatially limited to small microtopographic elevations, and that forest CH_4 sink might not provide significant local balance in the taiga–tundra boundary lowland. Further analysis of physical and biological control factors combined to *in situ* observation and remote sensing could promote the local-regional study of CH_4 emissions and vegetation dynamics affecting biogeochemical cycles.

4-2-2 Estimation of riverine dissolved methane using water color remote sensing in extreme flood event

An extreme flooding event influenced an extensive lowland and made to increase river CH_4 concentrations under recession phase in tributary in Indigirka watershed, eastern Siberia at the end of July 2017. We reported that the dissolved CH_4 concentrations along the Indigirka River and its tributaries (0.1–1.1 μM) were higher than those previously reported at Lena (0.01–0.7 μM), adjacent catchment from our study location in northeastern Siberia. An empirical end-member model to estimate the dissolved CH_4 concentrations from red band (636–673 nm) satellite data, validated by *in situ* river CH_4 measurements and training pixels corresponding to sampling sites, revealed spatial patterns of river CH_4 concentrations in the study region (approx. 250 × 350 km). We further presented that the total river flux in 2017 (9.4±3.5 mg CH_4 m^{-2} d^{-1}), of which 60% was sourced from the tributaries, was remarkably higher than that in 2016 (2.6±1.1 mg CH_4 m^{-2} d^{-1}); daily emissions of river CH_4 were 3.6 times higher in 2017 than 2016. The methods applied to dissolved CH_4 with satellite observations has a benefit for efficient monitoring of an extreme event in remote areas such as Siberia, where manual sampling of whole region is too much cost consuming. Future analysis could combine other factors, such as dissolved oxygen, organic matter concentrations, and isotope tracers of water and CH_4, to better understand biogeochemical cycles in high latitude lowlands.

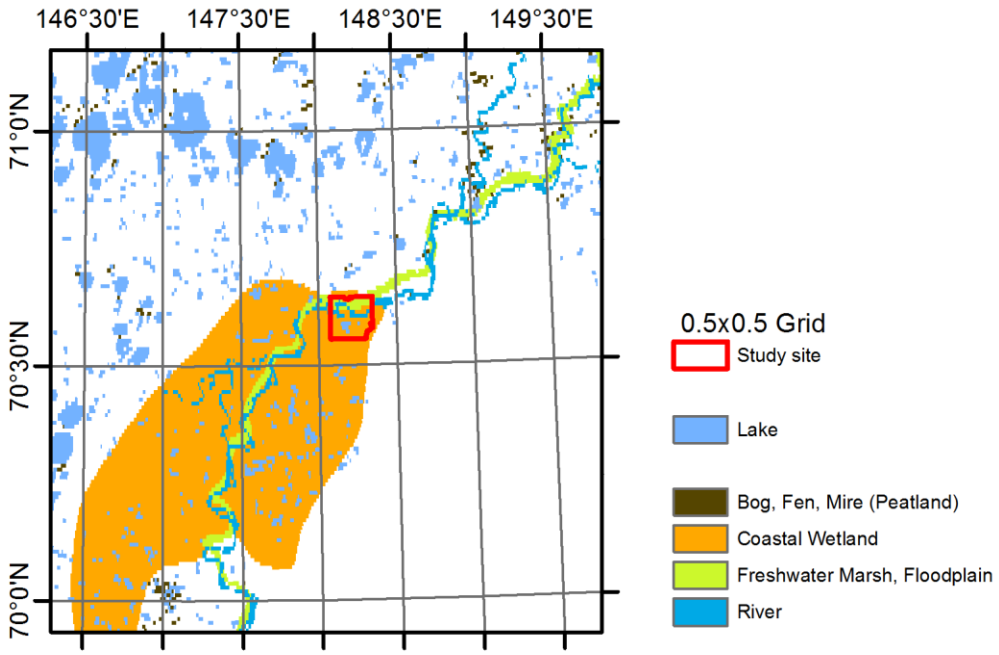

Figure 4-1. Map of Global Lake and Wetland Database (GLWD; Lehnar and Döll, 2004) and 10 km ×10 km study site in this study (red line). Grid lines shows the size of model resolution in VISIT (Ito and Inatomi, 2012).

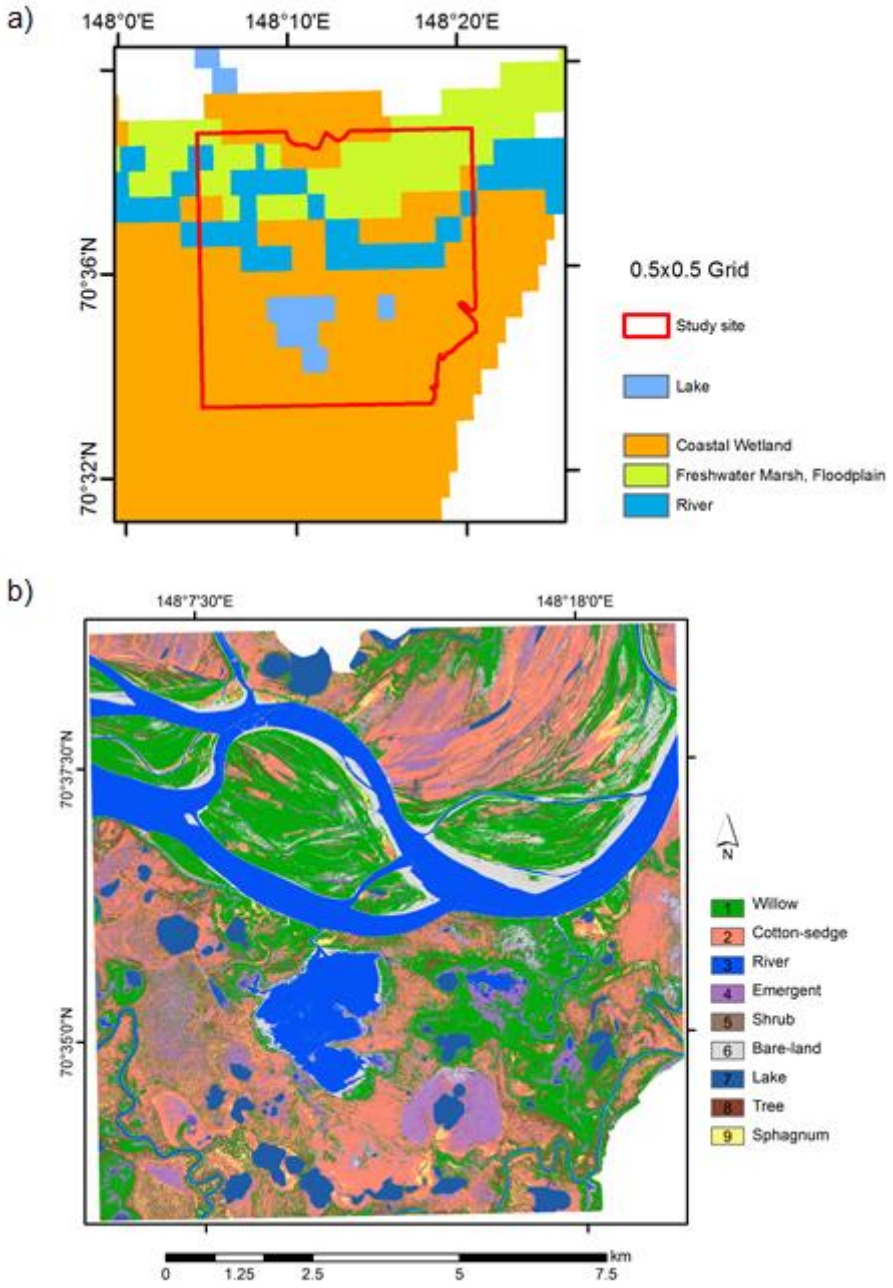

Figure 4-2. (a) GLWD image and (b) vegetation map classified into nine classes in this study (Chapter 2). Lake and river fractions were similar between two datasets. Large part of Cotton-sedge, emergent and willow around lakes (this study) were accounted for coastal wetland in GLWD. Willow around river was accounted for freshwatrer marsh and floodplain.

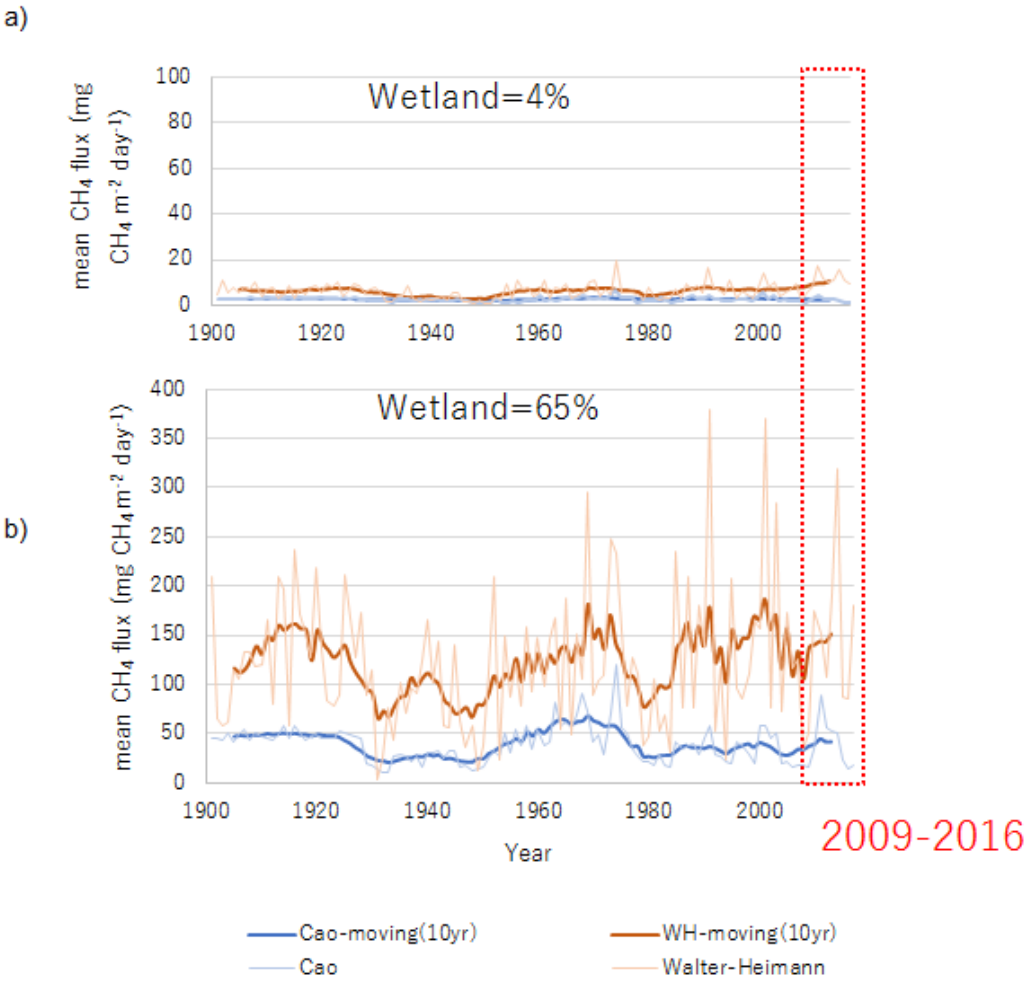

Figure 4-3. Average values of model output from 1900 to 2017 on VISIT (Ito and Inatomi, 2012). (a) a grid on upland area (70.75N, 148.75E) were covered by 4% of wetland. (b) a grid on lowland area (70.25N, 146.75E) were covered by 65% of wetland in GLWD. Cao's single layer model was calculated by whole flux, whereas WH (Walter-Heimann's) multilayer model was calculated by diffusive, ebullsive and plant-mediated transport pathway of fluxes. Interannual variations were ranged 0.67-0.34 (CoV) among different methods in 2009-2016. (Output of model simulation was provided by Prof. Ito)

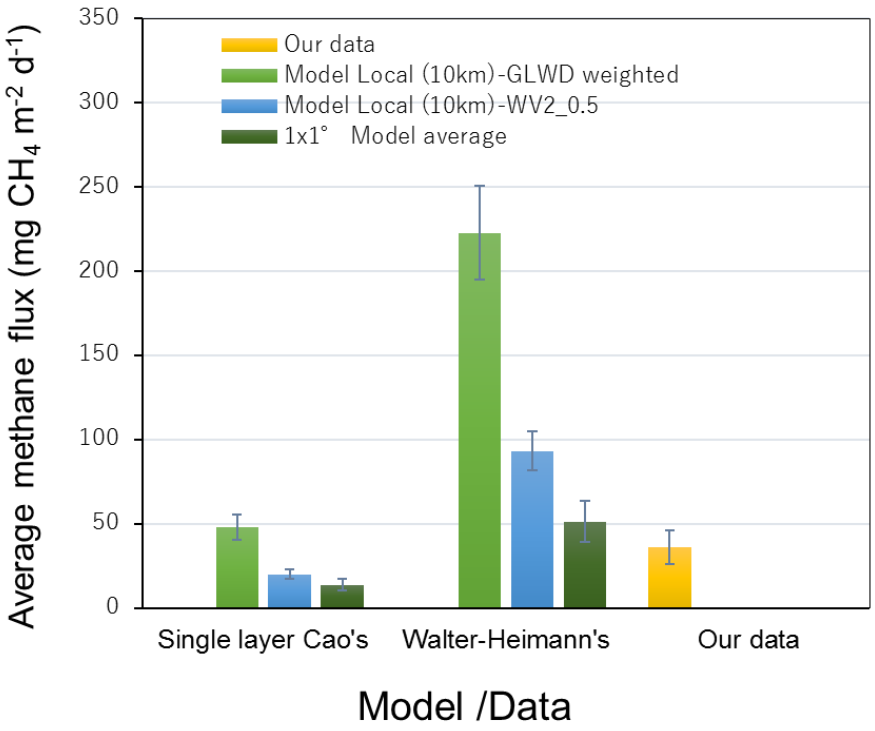

Figure 4-4. Average methane flux per square meter for model outputs and data in this study. Model output of four grids were averaged into 1 ×1° , and weighted by wetland coverage in 10 ×10km of GLWD and our vegetation map (WV2_0.5). There were large overestimations in WH methods in GLWD weighted result. On the other hand, Cao's result were similar or lower values compared to our result.

Acknowledgements

I am deeply grateful to Professor Atsuko Sugimoto (Hokkaido University) for the opportunity of the study and her kind support throughout my study of seven years (since the undergraduate thesis). I also appreciate Associate Prof. M. Yamamoto (Hokkaido University), Associate Prof. Y. Yamashita (Hokkaido University), and Assistant Prof. T. Irino (Hokkaido University) for many advices on my study and kind encouragement. I also thank all committee members of the doctoral decertation, Prof. A. Sugimoto, Prof. K. Suzuki (Hokkaido University), Assoc. Prof. M. Yamamoto, Assoc. Prof. Y. Yamashita, and Prof. S. Maksyutov (CGER/NIES in Tsukuba), who kindly reviewed the thesis.

I would like to thank Prof. T. C. Maximov, Dr. A. Kononov, P. Roman, S. Ksenofontov, A. Alekseeva, Dr. A. Popova, E. Starostin and all members of the biogeochemical laboratories in Institute for Biological Problem of Cryolithozone (IBPC SB RAS) and the BEST center in North Eastern Federal University (NEFU) for their support of fieldworks in eastern Siberia, Russia. I also thank for plants name identification from Drs. V. Zakharova, A. Egorova, A. Efimova and all members of botanical laboratories in IBPC, Russia. I would like to express my gratitude to Dr. R. Suzuki (JAMSTEC), Dr. H. Kobayashi (JAMSTEC) and Dr. S. Nagai (JAMSTEC) for their helpful scientific suggestions and research cooperations especially on remote sensing and kind support to accomplish this study. I would like to thank Dr. A. Ito (NIES) for kind data provision of a global biogeochemical model in the general discussion.

I would have special acknowledgement to R. Shingubara especially for sample measurements, and present members: Dr. S. Tei, Dr. Y. Miyamoto, Y. Hoshino, S. Nunohashi, S. Takano, R. Fan, S. Ruslan, S. Hashiguchi, S. Zhong, A. Nogovitsyn, K. Tanekura and graduated former members: H. Kudo, A. Ueta, A. Popova, M. Liang, R. Fujiyoshi, A. Kitayama, colleague: K. Tanaka, S. Goto, and all members of our laboratory and hensen-group for helpful discussion and fieldwork cooperation.

Finally, I would like to express my deepest gratitude to my family for their encouragement and supports.

Researches and educations were supported by institutions and fundings of Hokkaido University, NIPR, UArctic, NEFU, UiT, JANATEX, JREX, RJE3, IFES-GCOE, JSPS KAKANHI (grants JP21403011 [A. Sugimoto], JP16J07265 [T. Morozumi]), JSPS Research Fellowship for Young Scientists DC2, GRENE Arctic Climate Change Research Project by MEXT, and Belmont forum, 2014CRA, COPERA by JST.

References

Akaike H. 1974. A new look at the statistical model identification. *IEEE Trans. Automat. Contr*. AC-19:716-23.

Andresen, C. G., Lara, M. J., Tweedie, C. E. and Lougheed, V. L. 2017. Rising plant-mediated methane emissions from arctic wetlands. *Global Change Biology* **23**, 1128-1139.

Aufdenkampe, A. K., Mayorga, E., Raymond, P. A., Melack, J. M., Doney, S. C. and co-authors 2011. Riverine coupling of biogeochemical cycles between land, oceans, and atmosphere. *Frontiers in Ecology and the Environment* **9**, 53-60.

Barbosa, P. M., Melack, J. M., Farjalla, V. F., Amaral, J. H. F., Scofield, V., Forsberg, B. R. 2016. Diffusive methane fluxes from Negro, Solimoes and Madeira rivers and fringing lakes in the Amazon basin. Limnology and Oceanography, 61, 221-237.

Bartsch, A., Hofler, A., Kroisleitner, C. and Trofaier, A. M. 2016. Land Cover Mapping in Northern High Latitude Permafrost Regions with Satellite Data: Achievements and Remaining Challenges. *Remote Sensing* **8**, 27.

Bastviken, D., Tranvik, L. J., Downing, J. A., Crill, P. M. and Enrich-Prast, A. 2011. Freshwater Methane Emissions Offset the Continental Carbon Sink. *Science* **331**, 50-50.

Berner, L. T., Beck, P. S. A., Bunn, A. G. and Goetz, S. J. 2013. Plant response to climate change along the forest-tundra ecotone in northeastern Siberia. *Global Change Biology* **19**, 3449-3462.

Billett, M. F. and Harvey, F. H. 2013. Measurements of CO2 and CH4 evasion from UK peatland headwater streams. *Biogeochemistry* **114**, 165-181.

Blok, D., Heijmans, M., Schaepman-Strub, G., Kononov, A. V., Maximov, T. C. and co-authors 2010. Shrub expansion may reduce summer permafrost thaw in Siberian tundra. *Global Change Biology* **16**, 1296-1305.

Brezonik, P. L., Olmanson, L. G., Finlay, J. C. & Bauer, M. E. 2015. Factors affecting the measurement of CDOM by remote sensing of optically complex inland waters. Remote Sensing of Environment, 157, 199-215.

Budishchev, A., Mi, Y., van Huissteden, J., Belelli-Marchesini, L., Schaepman-Strub, G. and co-authors 2014. Evaluation of a plot-scale methane emission model using eddy covariance observations and footprint modelling. *Biogeosciences* **11**, 4651-4664.

Bunting, P. and Lucas, R. 2006. The delineation of tree crowns in Australian mixed species forests using hyperspectral Compact Airborne Spectrographic Imager (CASI) data. *Remote Sensing of Environment* **101**, 230-248.

Bussmann, I. 2013. Distribution of methane in the Lena Delta and Buor-Khaya Bay, Russia. *Biogeosciences*, 10(7), 4641-4652.

CAFF 2013. ABA 2013 Appendix 9.1 - List and distribution of all Arctic vascular plantseds. Tom, B., D. F.

J.A., G. Lynn and P. Michel).

Callaghan, T. V., Crawford, R. M. M., Eronen, M., Hofgaard, A., Payette, S. and co-authors 2002. The dynamics of the tundra-taiga boundary: An overview and suggested coordinated and integrated approach to research. *Ambio*, **Spec 12**. 3-5.

Campeau, A. and Del Giorgio, P. A. 2014. Patterns in CH4 and CO2 concentrations across boreal rivers: Major drivers and implications for fluvial greenhouse emissions under climate change scenarios. *Global Change Biology* **20**, 1075-1088.

Campeau, A., Lapierre, J. F., Vachon, D. and del Giorgio, P. A. 2014. Regional contribution of CO2 and CH4 fluxes from the fluvial network in a lowland boreal landscape of Quebec. *Global Biogeochemical Cycles* **28**, 57-69.

Chasmer, L., Hopkinson, C., Veness, T., Quinton, W. and Baltzer, J. 2014. A decision-tree classification for low-lying complex land cover types within the zone of discontinuous permafrost. *Remote Sensing of Environment* **143**, 73-84.

Ciais, P., C. Sabine, G. Bala, L. Bopp, V. Brovkin, J. Canadell, A. Chhabra, R. DeFries, J. Galloway, M. Heimann, and C. Jones, C. L. Q., R.B. Myneni, S. Piao and P. Thornton 2013. Carbon and Other Biogeochemical Cycles *In:Climate Change 2013: The Physical Science Basis. Contribution of Working GroupI to the Fifth Assessment Report of the Intergovernmental Panel on Climate Change*. Cambridge, United Kingdom and New York, NY, USA, Cambridge University Press.

Clark, R. N., Swayze, G. A., Gallagher, A. J., King, T. V. V. and Calvin, W. M. 1993. The U. S. Geological Survey, Digital Spectral Library: Version 1 (0.2 to 3.0um). In: *Open-File Report*.

Congalton, R. G. 1991. A Review of assessing the accuracy of classifications of remote sensed data. *Remote Sensing of Environment* **37**, 35-46.

Crawford, J. T., Loken, L. C., West, W. E., Crary, B., Spawn, S. A., Gubbins, N., Jones, S. E., Striegl, R. G. & Stanley, E. H. 2017. Spatial heterogeneity of within-stream methane concentrations. *Journal of Geophysical Research-Biogeosciences*, 122(5), 1036-1048.

Davidson, S. J., Sloan, V. L., Phoenix, G. K., Wagner, R., Fisher, J. P. and co-authors 2016. Vegetation Type Dominates the Spatial Variability in CH4 Emissions Across Multiple Arctic Tundra Landscapes. *Ecosystems* **19**, 1116-1132.

de Klerk, P., Donner, N., Karpov, N. S., Minke, M. and Joosten, H. 2011. Short-term dynamics of a low-centred ice-wedge polygon near Chokurdakh (NE Yakutia, NE Siberia) and climate change during the last ca 1250 years. *Quaternary Science Reviews* **30**, 3013-3031.

Desyatkin, A. R., Takakai, F., Fedorov, P. P., Nikolaeva, M. C., Desyatkin, R. V. and co-authors 2009. CH(4) emission from different stages of thermokarst formation in Central Yakutia, East Siberia. *Soil Science and Plant Nutrition* **55**, 558-570.

Du, H., C.-I. Chang, H. Ren, F. M. D'Amico, and J. O. Jensen, J. 2004. New Hyperspectral Discrimination Measure for Spectral Characterization. *Optical Engineering* 43, **8**. 1777-1786

Dyson, K. E., Billett, M. F., Dinsmore, K. J., Harvey, F., Thomson, A. M. and co-authors 2011. Release of aquatic carbon from two peatland catchments in E. Finland during the spring snowmelt period. *Biogeochemistry* **103**, 125-142.

Egorova, A. A. 2013. Flora of vascular plants of the Resource Reserve “Kytalyk” (Northeastern Yakutia). In: Proceedings of the 2nd International Conference on “Global Warming and the Human-Nature Dimension in Siberia:Social Adaptation to the Changes of the Terrestrial Ecosystem, with an Emphasis on Water Environments”& 7th Annual International Workshop "C/H2O/Energy balance and climate over boreal and arctic regions with special emphasis on eastern Eurasia", Yakutsk, Russia, 2013. Online at : http://www.chikyu.ac.jp/siberia/2nd_International_Conference.pdf

Emmerton, C. A., Lesack, L. F. W. and Marsh, P. 2007. Lake abundance, potential water storage, and habitat distribution in the Mackenzie River Delta, western Canadian Arctic. *Water Resources Research* **43**, 14.

Epstein, H. E., Beringer, J., Gould, W. A., Lloyd, A. H., Thompson, C. D. and co-authors 2004. The nature of spatial transitions in the Arctic. *Journal of Biogeography* **31**, 1917-1933.

Fernandez, J. E., Peeters, F., Hofmann, H. 2016. On the methane paradox: Transport from shallow water zones rather than in situ methanogenesis is the major source of CH4 in the open surface water of lakes. *Journal of Geophysical Research-Biogeosciences*, 121(10), 2717-2726.

Flessa, H., Rodionov, A., Guggenberger, G., Fuchs, H., Magdon, P. and co-authors 2008. Landscape controls of CH4 fluxes in a catchment of the forest tundra ecotone in northern Siberia. *Global Change Biology* **14**, 2040-2056.

Forbes, B. C., Fauria, M. M. and Zetterberg, P. 2010. Russian Arctic warming and 'greening' are closely tracked by tundra shrub willows. *Global Change Biology* **16**, 1542-1554.

Frey, K. E. and McClelland, J. W. 2009. Impacts of permafrost degradation on arctic river biogeochemistry. *Hydrological Processes* **23**, 169-182.

Frost, G. V. and Epstein, H. E. 2014. Tall shrub and tree expansion in Siberian tundra ecotones since the 1960s. *Global Change Biology* **20**, 1264-1277.

Glagolev, M., Kleptsova, I., Filippov, I., Maksyutov, S. and Machida, T. 2011. Regional methane emission from West Siberia mire landscapes. *Environmental Research Letters* **6**, 7.

Harding, R., Kuhry, P., Christensen, T. R., Sykes, M. T., Dankers, R. and co-authors 2002. Climate feedbacks at the tundra-taiga interface. *Ambio*, Spec12. 47-55.

Huh, Y., Tsoi, M. Y., Zaitsev, A. and Edmond, J. M. 1998. The fluvial geochemistry of the rivers of eastern Siberia: I. Tributaries of the Lena River draining the sedimentary platform of the Siberian Craton. *Geochimica Et Cosmochimica Acta* **62**, 1657-1676.

Ito, A. and Inatomi, M. 2012. Use of a process-based model for assessing the methane budgets of global terrestrial ecosystems and evaluation of uncertainty. *Biogeosciences* **9**, 759-773.

Iwahana, G., Takano, S., Petrov, R. E., Tei, S., Shingubara, R. and co-authors 2014. Geocryological

characteristics of the upper permafrost in a tundra-forest transition of the Indigirka River Valley, Russia. *Polar Science* **8**, 96-113.

James, A. L. and Roulet, N. T. 2006. Investigating the applicability of end-member mixing analysis (EMMA) across scale: A study of eight small, nested catchments in a temperate forested watershed. *Water Resources Research* **42**, 17.

Johansson, T., Malmer, N., Crill, P. M., Friborg, T., Akerman, J. H. and co-authors 2006. Decadal vegetation changes in a northern peatland, greenhouse gas fluxes and net radiative forcing. *Global Change Biology* **12**, 2352-2369.

Karlsson, J., Giesler, R., Persson, J. and Lundin, E. 2013. High emission of carbon dioxide and methane during ice thaw in high latitude lakes. *Geophysical Research Letters* **40**, 1123-1127.

Khitun, O. V., Koroleva, T. M., Chinenko, S. V., Petrovsky, V. V., Pospelova, E. B. and co-authors 2016. Applications of local floras for floristic subdivision and monitoring vascular plant diversity in the Russian Arctic. *Arctic Science* **2**, 103-126.

Kling, G.W., Kipphut, G.W., & Miller, M.C. (1992). The flux of CO2 and CH4 from lakes and rivers in Arctic Alaska. *Hydrobiologia*, 240, 23-36.

Kravtsova, V. I. and Loshkareva, A. R. 2013. Dynamics of vegetation in the tundra-taiga ecotone on the Kola Peninsula depending on climate fluctuations. *Russian Journal of Ecology* **44**, 303-311.

Langer, M., Westermann, S., Anthony, K. W., Wischnewski, K. and Boike, J. 2015. Frozen ponds: production and storage of methane during the Arctic winter in a lowland tundra landscape in northern Siberia, Lena River delta. *Biogeosciences* **12**, 977-990.

Lara, M. J., McGuire, A. D., Euskirchen, E. S., Tweedie, C. E., Hinkel, K. M. and co-authors 2015. Polygonal tundra geomorphological change in response to warming alters future CO2 and CH4 flux on the Barrow Peninsula. *Global Change Biology* **21**, 1634-1651.

Liang, M. C., Sugimoto, A., Tei, S., Bragin, I. V., Takano, S. and co-authors 2014. Importance of soil moisture and N availability to larch growth and distribution in the Arctic taiga-tundra boundary ecosystem, northeastern Siberia. *Polar Science* **8**, 327-341.

Lloyd, A. H., Rupp, T. S., Fastie, C. L. and Starfield, A. M. 2002. Patterns and dynamics of treeline advance on the Seward Peninsula, Alaska. *Journal of Geophysical Research-Atmospheres* **108**, 15.

Loranty, M. M., Lieberman-Cribbin, W., Berner, L. T., Natali, S. M., Goetz, S. J. and co-authors 2016. Spatial variation in vegetation productivity trends, fire disturbance, and soil carbon across arctic-boreal permafrost ecosystems. *Environmental Research Letters* **11**, 13.

Maechler, M. and al, e. 2013. Cluster analysis extended Rousseeuw et al. R CRAN.

Marsh, P. and Hey, M. 1989. The flooding hydrology of Mackenzie Delta lakes near Inuvik, NWT, Canada. *Arctic* **42**, 41-49.

Mastepanov, M., Sigsgaard, C., Strom, L., Tamstorf, M. P., Lund, M. and co-authors 2013. Revisiting

factors controlling methane emissions from high-Arctic tundra. *Biogeosciences* **10**, 5139-5158.

Matveev, A., Laurion, I., Deshpande, B. N., Bhiry, N. and Vincent, W. F. 2016. High methane emissions from thermokarst lakes in subarctic peatlands. *Limnology and Oceanography* **61**, S150-S164.

McFeeters, S. K. 1996. The use of the normalized difference water index (NDWI) in the delineation of open water features. *International Journal of Remote Sensing*, 17(7), 1425-1432.

Menyailo, O. V., Abraham, W. R. and Conrad, R. 2010. Tree species affect atmospheric CH4 oxidation without altering community composition of soil methanotrophs. *Soil Biology & Biochemistry* **42**, 101-107.

Mertes, L. A. K., Smith, M. O., Adams, J. B. 1993. Estimating suspended sediment concentrations in surface waters of the Amazon river wetlands from Landsat images. *Remote Sensing of Environment*, 43(3), 281-301.

Montesano, P. M., Nelson, R., Sun, G., Margolis, H., Kerber, A. and co-authors 2009. MODIS tree cover validation for the circumpolar taiga-tundra transition zone. *Remote Sensing of Environment* **113**, 2130-2141.

Morishita, T., Hatano, R. and Desyatkin, R. V. 2003. CH(4) flux in an Alas ecosystem formed by forest disturbance near Yakutsk, eastern Siberia, Russia. *Soil Science and Plant Nutrition* **49**, 369-377.

Morishita, T., Matsuura, Y., Kajimoto, T., Osawa, A., Zyryanova, O. A. & Prokushkin, A. S. 2014. CH4 and N2O dynamics of a Larix gmelinii forest in a continuous permafrost region of central Siberia during the growing season. *Polar Science*, 8(2), pp 156-165.

Morozumi, T., Shingubara, R., Fan, R., Takano, S., Tei, S., Maximov, T. C., Kobayashi, H., Suzuki, R. & Sugimoto, A. 2016. High resolution vegetation mapping for upscaling of local CH4 emission in Taiga-Tundra boundary, eastern Siberia. proceeding of International Symposium on Remote Sensing, 2016 Korea.

Murase, J., Sakai, Y., Sugimoto, A., Okubo, K. and Sakamoto, M. 2003. Sources of dissolved methane in Lake Biwa. *Limnology* **4**, 91-99.

Muster, S., Langer, M., Heim, B., Westermann, S. and Boike, J. 2012. Subpixel heterogeneity of ice-wedge polygonal tundra: a multi-scale analysis of land cover and evapotranspiration in the Lena River Delta, Siberia. *Tellus Series B-Chemical and Physical Meteorology* **64**, 19.

Myhre, G., D. Shindell, F.-M. Bréon, W. Collins, J. Fuglestvedt, J. Huang, D. Koch, J.-F. Lamarque, D. Lee, B. Mendoza, T. Nakajima, A. Robock, G. Stephens, T. Takemura and H. Zhang 2013. Anthropogenic and Natural Radiative Forcing. Cambridge, United Kingdom and New York, NY, USA, Cambridge University Press.

Nakano, T., Inoue, G. and Fukuda, M. 2004. Methane consumption and soil respiration by a birch forest soil in West Siberia. *Tellus Series B-Chemical and Physical Meteorology* **56**, 223-229.

Nauta, A. L., Heijmans, M., Blok, D., Limpens, J., Elberling, B. and co-authors 2015. Permafrost collapse after shrub removal shifts tundra ecosystem to a methane source. *Nature Climate Change* **5**,

67-70.

Neal, C., Jarvie, H. P., Williams, R., Love, A., Neal, M. and co-authors 2010. Declines in phosphorus concentration in the upper River Thames (UK): Links to sewage effluent cleanup and extended end-member mixing analysis. *Science of the Total Environment* **408**, 1315-1330.

Nicholson, B. J., Gignac, L. D. and Bayley, S. E. 1996. Peatland distribution along a north-south transect in the Mackenzie River Basin in relation to climatic and environmental gradients. *Vegetatio* **126**, 119-133.

Nilsson, M., Mikkela, C., Sundh, I., Granberg, G., Svensson, B. H. and co-authors 2001. Methane emission from Swedish mires: National and regional budgets and dependence on mire vegetation. *Journal of Geophysical Research-Atmospheres* **106**, 20847-20860.

Olefeldt, D., Turetsky, M. R., Crill, P. M. and McGuire, A. D. 2013. Environmental and physical controls on northern terrestrial methane emissions across permafrost zones. *Global Change Biology* **19**, 589-603.

Pajunen, A. M. 2009. Environmental and Biotic Determinants of Growth and Height of Arctic Willow Shrubs along a Latitudinal Gradient. *Arctic Antarctic and Alpine Research* **41**, 478-485.

Parmentier, F. J. W., van Huissteden, J., Kip, N., den Camp, H., Jetten, M. S. M. and co-authors 2011a. The role of endophytic methane-oxidizing bacteria in submerged Sphagnum in determining methane emissions of Northeastern Siberian tundra. *Biogeosciences* **8**, 1267-1278.

Parmentier, F. J. W., van Huissteden, J., van der Molen, M. K., Schaepman-Strub, G., Karsanaev, S. A. and co-authors 2011b. Spatial and temporal dynamics in eddy covariance observations of methane fluxes at a tundra site in northeastern Siberia. *Journal of Geophysical Research-Biogeosciences* **116**, 14.

Peregon, A., S. Maksyutov, N. P. Kosykh, and N. P. Mironycheva‐Tokareva. 2008. Map‐based inventory of wetland biomass and net primary production in western Siberia, *J. Geophys. Res*., **113**, G01007, doi:10.1029/2007JG000441.

Peregon A., Maksyutov S., Yamagata Y. 2009. An image-based inventory of the spatial structure of West Siberian wetlands. *Environ. Res. Lett*., **4**, 045014, doi:10.1088/1748-9326/4/4/045014.

R-Core-Team 2013. R foundation for statistical computing, Vienna, Austria.

Ranson, K. J., Montesano, P. M. and Nelson, R. 2011. Object-based mapping of the circumpolar taiga-tundra ecotone with MODIS tree cover. *Remote Sensing of Environment* **115**, 3670-3680.

Richards, J. A. and Jia, X. 1999. *Remote Sensing Digital Image Analysis*, Springer.

Rokni, K., Ahmad, A., Selamat, A. and Hazini, S. 2014. Water Feature Extraction and Change Detection Using Multitemporal Landsat Imagery. *Remote Sensing* **6**, 4173-4189.

Roulet, N. T., Jano, A., Kelly, C. A., Klinger, L. F., Moore, T. R. and co-authors 1994. Role of the Hudson-Bay Lowland as a source of atmospheric methane. *Journal of Geophysical Research-Atmospheres* **99**, 1439-1454.

Sabrekov, A., Glagolev, M., Irina, T., K, Machida, T., Maksyutov, S. 2013. Methane emission from mires of the West Siberian taiga. *Eurasian Soil Science*. **46**. 10.1134/S1064229314010098.

Sachs, T., Giebels, M., Boike, J. and Kutzbach, L. 2010. Environmental controls on CH4 emission from polygonal tundra on the microsite scale in the Lena river delta, Siberia. *Global Change Biology* **16**, 3096-3110.

Sawakuchi, H. O., Bastviken, D., Sawakuchi, A. O., Krusche, A. V., Ballester, M. V. R. and co-authors 2014. Methane emissions from Amazonian Rivers and their contribution to the global methane budget. *Global Change Biology* **20**, 2829-2840.

Sawamoto, T., Takakai, F., Desyatkin, A. R., Desyatokin, R. V. & Hatano, R. 2006. Dissolved N2O and CH4 in seepage and stream water in Yakutsk, R. Hatano, G. Guggenberger (Eds.), *Symptom of Environmental Change in Siberian Permafrost Region*, Sapporo, Japan: Hokkaido University Press.

Schickhoff, U., Walker, M. D. and Walker, D. A. 2002. Riparian willow communities on the Arctic Slope of Alaska and their environmental relationships: A classification and ordination analysis. *Phytocoenologia* **32**, 145-204.

Schneider, J., Grosse, G. and Wagner, D. 2009. Land cover classification of tundra environments in the Arctic Lena Delta based on Landsat 7 ETM+ data and its application for upscaling of methane emissions. *Remote Sensing of Environment* **113**, 380-391.

Semiletov, I. P., Pipko, II, Shakhova, N. E., Dudarev, O. V., Pugach, S. P. and co-authors 2011. Carbon transport by the Lena River from its headwaters to the Arctic Ocean, with emphasis on fluvial input of terrestrial particulate organic carbon vs. carbon transport by coastal erosion. *Biogeosciences* **8**, 2407-2426.

Settele, J., R. Scholes, R. Betts, S. Bunn, P. Leadley, D. Nepstad, J.T. Overpeck, and M.A. Taboada, 2014. Terrestrial and inland water systems *In: Climate Change 2014: Impacts, Adaptation, and Vulnerability.Part A: Global and Sectoral Aspects. Contribution of Working Group II to the Fifth Assessment Report of theIntergovernmental Panel on Climate Change*. Cambridge, UnitedKingdom and New York, NY, USA, Cambridge University Press

Shakhova, N. E., Semiletov, I. P., Bel'cheva, N. N. 2007. The great Siberian rivers as a source of methane on the Russian Arctic shelf. Doklady Earth Sciences, 415(5), 734-736.

Shingubara, R., Sugimoto, A., Murase, J., Tei, S., Takano, S. and co-authors 2016. Multi-year response of CH_4 efflux to wetting at Indigirka Lowland in Northeastern Siberia. In: *Japan Geoscience Union Meeting*, Chiba, Japan.

Shingubara, R., Sugimoto, A., Murase, J., Iwahana, G., Tei, and co-authors. 2019. Multi-year effect of wetting on CH4 flux at taiga–tundra boundary in northeastern Siberia deduced from stable isotope ratios of CH4, *Biogeosciences*, **16**, 755-768, https://doi.org/10.5194/bg-16-755-2019.

Sidorchuk, A. and Matveev, B. 1994. Channel processes and erosion rates in the rivers ofthe Yamal

Peninsula in western Siberia. In: *Proceedings of the The Symposiumon Variability in Stream Erosion and Sediment Transport*, Canberra, December 1994. IAHS Publ. 224.197-202 1994.

Sidorchuk, A. Y., Panin, A. V., Borisova, O. K., Elias, S. A. and Syvistki, J. P. 2000. Channel morphology and river flow in the northern Russian Plain in the Late Glacial and Holocene. *International Journal of Earth Sciences* **89**, 541-549.

Sjogersten, S. and Wookey, P. A. 2002. Climatic and resource quality controls on soil respiration across a forest-tundra ecotone in Swedish Lapland. *Soil Biology & Biochemistry* **34**, 1633-1646.

Sjogersten, S. and Wookey, P. A. 2009. The Impact of Climate Change on Ecosystem Carbon Dynamics at the Scandinavian Mountain Birch Forest-Tundra Heath Ecotone. *Ambio* **38**, 2-10.

Skre, O., Baxter, R., Crawford, R. M. M., Callaghan, T. V. and Fedorkov, A. 2002. How will the tundra-taiga interface respond to climate change? *Ambio*, **Spec 12**. 37-46.

Soja, A. J., Tchebakova, N. M., French, N. H. F., Flannigan, M. D., Shugart, H. H. and co-authors 2007. Climate-induced boreal forest change: Predictions versus current observations. *Global and Planetary Change* **56**, 274-296.

Stanley, E. H., Casson, N. J., Christel, S. T., Crawford, J. T., Loken, L. C. and co-authors 2016. The ecology of methane in streams and rivers: patterns, controls, and global significance. *Ecological Monographs* **86**, 146-171.

Striegl, R. G., Dornblaser, M. M., McDonald, C. P., Rover, J. R. and Stets, E. G. 2012. Carbon dioxide and methane emissions from the Yukon River system. *Global Biogeochemical Cycles* **26**, 11.

Strom, L., Falk, J. M., Skov, K., Jackowicz-Korczynski, M., Mastepanov, M. and co-authors 2015. Controls of spatial and temporal variability in CH4 flux in a high arctic fen over three years. *Biogeochemistry* **125**, 21-35.

Suzuki, K., Matsuo, K. and Hiyama, T. 2016. Satellite gravimetry-based analysis of terrestrial water storage and its relationship with run-off from the Lena River in eastern Siberia. *International Journal of Remote Sensing* **37**, 2198-2210.

Takeuchi, W., Tamura, M. and Yasuoka, Y. 2003. Estimation of methane emission from West Siberian wetland by scaling technique between NOAA AVHRR and SPOT HRV. *Remote Sensing of Environment* **85**, 21-29.

Tchebakova, N. M., Parfenova, E. and Soja, A. J. 2009. The effects of climate, permafrost and fire on vegetation change in Siberia in a changing climate. *Environmental Research Letters* **4**, 9.

Tei, S., Sugimoto, A., Liang, M. C., Yonenobu, H., Matsuura, Y. and co-authors 2017. Radial Growth and Physiological Response of Coniferous Trees to Arctic Amplification. *Journal of Geophysical Research-Biogeosciences* **122**, 2786-2803.

Terentieva, I. E., Glagolev, M. V., Lapshina, E. D., Sabrekov, A. F., and Maksyutov, S. 2016. Mapping of West Siberian taiga wetland complexes using Landsat imagery: implications for methane emissions, *Biogeosciences*, 13, 4615-4626, https://doi.org/10.5194/bg-13-4615-2016.

Tou, J. T. and R. C. Gonzalez, 1974. Pattern Recognition Principles, Addison-Wesley Publishing Company, Reading, Massachusetts.

Troeva, E., Isaev, A., Cherosov, M. and Karpov, N. 2010. *The Far North:: Plant Biodiversity and Ecology of Yakutia*.

van Huissteden, J., Maximov, T. C., Kononov, A. V. and Dolman, A. J. 2008. Summer soil CH4 emission and uptake in taiga forest near Yakutsk, Eastern Siberia. *Agricultural and Forest Meteorology* **148**, 2006-2012.

Vermote, E. F., Tanre, D., Deuze, J. L., Herman, M. and Morcrette, J. J. 1997. Second Simulation of the Satellite Signal in the Solar Spectrum, 6S: An overview. *Ieee Transactions on Geoscience and Remote Sensing* **35**, 675-686.

Virtanen, T. and Ek, M. 2014. The fragmented nature of tundra landscape. *International Journal of Applied Earth Observation and Geoinformation* **27**, 4-12.

Volpe, V., Silvestri, S. and Marani, M. 2011. Remote sensing retrieval of suspended sediment concentration in shallow waters. *Remote Sensing of Environment* **115**, 44-54.

Walter, K. M., Zimov, S. A., Chanton, J. P., Verbyla, D. and Chapin, F. S. 2006. Methane bubbling from Siberian thaw lakes as a positive feedback to climate warming. *Nature* **443**, 71-75.

Wanninkhof, R. 1992. RELATIONSHIP BETWEEN WIND-SPEED AND GAS-EXCHANGE OVER THE OCEAN. *Journal of Geophysical Research-Oceans* **97**, 7373-7382.

Ward, D. P., Hamilton, S. K., Jardine, T. D., Pettit, N. E., Tews, E. K. and co-authors 2013. Assessing the seasonal dynamics of inundation, turbidity, and aquatic vegetation in the Australian wetdry tropics using optical remote sensing. *Ecohydrology* **6**, 312-323.

Xiao, Q. T., Zhang, M., Hu, Z. H., Gao, Y. Q., Hu, C., Liu, C., Liu, S. D., Zhang, Z., Zhao, J. Y., Xiao, W., Lee, X. 2017. Spatial variations of methane emission in a large shallow eutrophic lake in subtropical climate. *Journal of Geophysical Research-Biogeosciences*, 122(7), 1597-1614.

Yabuki, H., Park, H., Kawamoto, H., Suzuki, R., Razuvaev, V.N., Bulygina, O.N., Ohata, T., 2011. Baseline Meteorological Data in Siberia (BMDS) Version 5.0. RIGC, JAMSTEC, Yokosuka, Japan distributed by CrDAP, Digital media.

Yamamoto, S., Alcauskas, J. B. and Crozier, T. E. 1976. Solubility of methane in distilled water and seawater. *Journal of Chemical & Engineering Data* **21**, 78-80.